INFORMATION TO USERS

This manuscript has been reproduced from the microfilm master. UMI films the text directly from the original or copy submitted. Thus, some thesis and dissertation copies are in typewriter face, while others may be from any type of computer printer.

The quality of this reproduction is dependent upon the quality of the copy submitted. Broken or indistinct print, colored or poor quality illustrations and photographs, print bleedthrough, substandard margins, and improper alignment can adversely affect reproduction.

In the unlikely event that the author did not send UMI a complete manuscript and there are missing pages, these will be noted. Also, if unauthorized copyright material had to be removed, a note will indicate the deletion.

Oversize materials (e.g., maps, drawings, charts) are reproduced by sectioning the original, beginning at the upper left-hand corner and continuing from left to right in equal sections with small overlaps.

ProQuest Information and Learning
300 North Zeeb Road, Ann Arbor, MI 48106-1346 USA
800-521-0600

UMI®

Curve Veering and a Parametric Study of Stiction in Capacitive Microelectromechanical Systems Subjected to Electrostatic and Casimir Forces

Azubuike E. Okwuobi

A Thesis
in
The Department of Mechanical and Industrial Engineering

Presented in Partial Fulfillment of the Requirements
for the
Degree of Master of Applied Science
at
Concordia University
Montreal, Quebec, Canada

June 2002

© Azubuike E. Okwuobi

National Library of Canada

Bibliothèque nationale du Canada

Acquisitions and Bibliographic Services

Acquisitions et services bibliographiques

395 Wellington Street
Ottawa ON K1A 0N4
Canada

395, rue Wellington
Ottawa ON K1A 0N4
Canada

Your file Votre référence

Our file Notre référence

The author has granted a non-exclusive licence allowing the National Library of Canada to reproduce, loan, distribute or sell copies of this thesis in microform, paper or electronic formats.

L'auteur a accordé une licence non exclusive permettant à la Bibliothèque nationale du Canada de reproduire, prêter, distribuer ou vendre des copies de cette thèse sous la forme de microfiche/film, de reproduction sur papier ou sur format électronique.

The author retains ownership of the copyright in this thesis. Neither the thesis nor substantial extracts from it may be printed or otherwise reproduced without the author's permission.

L'auteur conserve la propriété du droit d'auteur qui protège cette thèse. Ni la thèse ni des extraits substantiels de celle-ci ne doivent être imprimés ou autrement reproduits sans son autorisation.

0-612-72923-0

Canada

ABSTRACT

Curve Veering and a Parametric Study of Stiction in Capacitive Microelectromechanical Systems Subjected to Electrostatic and Casimir Forces

Azubuike E. Okwuobi

Curve veering is a phenomenon in which the plot of eigenvalues of a system against a system parameter sometimes results in curves that abruptly veer away from each other in a rapid but continuous manner at points where they are expected to intersect. For certain modes of vibration, the natural frequencies of rectangular plate structures obtained from an exact analysis are expected to intersect. However, approximate analysis would invariably indicate such curves veering away at those points. Occurrence of curve veering indicates the extent of approximation involved and hence it is important to understand this phenomenon from a design perspective. Any error will introduce errors in the response calculations and will result in poor design. In view of their small dimensions such approximations are critical in the estimation of natural frequencies of microelectromechanical systems (MEMS). This phenomenon is investigated for such systems subjected to electrostatic forces and assuming the existence of the Casimir forces.

Stiction, the functional impairment of capacitive microplates by sticking together, is a problem of instability to be avoided in MEMS. Previous parametric studies have shown that the strength of applied voltage influences this form of instability. In addition to

voltage, this thesis studies the influence of side ratio on microplates having various boundary conditions and subjected to the aforementioned field forces.

The system is modeled as a rectangular microplate with various boundary conditions based on a standard CRONOS fabrication procedure using the MUMPs technology. Since exact analysis is difficult in view of the non-linear nature of the system, the analysis is carried out using the Rayleigh-Ritz method to determine the natural frequencies, incorporating boundary characteristic orthogonal polynomials as assumed deflection shape functions. Results are presented and discussed based on numerical computations carried out using MATLAB.

The parametric study of the dependency of the non-dimensional natural frequency versus the side ratio a/b shows the locations of curve veering in the microplate, which occurs more than once at several locations of side ratio for an identifiable natural frequency curve having various boundary conditions. Results also indicate that the natural frequencies of the system are reduced with an increase in the applied voltage at a given side ratio culminating in instability and the occurrence of stiction. Furthermore it is seen that the Casimir effect is significant only in the sub-micron range and has no appreciable influence on the natural frequency for gaps in excess of 1 μm for the geometries considered. The variation of the natural frequency with voltage indicate that the side dimensions and boundary conditions of the plate have a significant influence on the stability of a microplate and should be taken into account in the design and analysis of capacitive MEMS.

"Trust in the Lord with all thine heart;

and lean not on thine own understanding.

In all thy ways acknowledge him; and He shall direct thy paths"

Proverbs 3:5-6

(The Holy Bible)

To

Professor P. A. C. Okwuobi and Mrs. L. Okwuobi

my parents

ACKNOWLEDGEMENTS

I consider it very fortuitous, and an honour to have as my supervisors, Professors R. B. Bhat and I. Stiharu , who through their teaching instruction, encouragement and financial support have made it possible to successfully complete this program. The suggestions, guidance and advice of these fine gentlemen have proved to be very useful in this thesis, as well as in the career decisions made, and is deeply appreciated and gratefully acknowledged.

The staff in the Department of Mechanical and Industrial Engineering of Concordia University from whom I have had support in one form or another is simply a wonderful team that has made the learning and research experience pleasurable. I wish to express my heartfelt thanks to the system analysts, Joe Hulet, William Wong and Weimin Pu, who ensured that all the assistance required in the optimal use of the departments' computing resources was rendered during my academic program. To John Elliott and Danius Juras, who have been so pleasant to work with, I wish to say thank you. I am also very grateful to the departmental graduate program secretary, Charlene Wald and secretary at CONCAVE (Concordia Computer Aided Vehicle Engineering) Research Centre, Arlene Zimmerman who have been very helpful in so many ways. For useful suggestions from my colleagues at CONCAVE I am also grateful.

Finally, I wish to express heartfelt thanks to my family who have been very patient and understanding during the course of the academic program.

TABLE OF CONTENTS

i.	List of Figures	xi
ii.	List of Tables	xvii
iii.	Nomenclature	xviii

CHAPTER 1

INTRODUCTION, LITERATURE REVIEW AND THESIS OBJECTIVES

1.1	Introduction	1
1.2	Curve Veering	6
1.3	Electrostatic Forces in MEMS	9
1.4	Casimir Force in MEMS	12
1.5	Motivation, Methods and Objectives	19

CHAPTER 2

DESIGN AND FABRICATION

2.1	Introduction to Microelectromechanical Systems	22
2.2	Design and Fabrication of a Microplate	25
	2.2.1 Process Design	28
	2.2.2 Layout Design	34
2.4	Post Processing	35

CHAPTER 3

ANALYSIS OF MICROPLATES INCLUDING ELECTROSTATIC AND CASIMIR FORCES

3.1 Electrostatic Force 40

3.2 Casimir Force 51

3.3 Elastic Force 57

3.4 Boundary Characteristic Orthogonal Polynomials 60

3.5 The Rayleigh-Ritz Method 70

CHAPTER 4

RESULTS AND DISCUSSIONS

4.1 Natural Frequencies 78

4.2 Curve Veering 91

4.3 Parametric Variations 139

CHAPTER 5

CONCLUSIONS AND RECOMMENDATIONS FOR FURTHER WORK

5.1 Conclusions 158

5.2 Recommendations for Further Work 161

REFERENCES 163

APPENDICES 174

A. Fabrication 174

A1 Design and Fabrication 174

A1.1 Thermal Oxidation 177

A1.2 Chemical Vapor Deposition 180

A1.3 Evaporation 183

A1.4 Sputtering 184

A1.5 Photolithography 186

A1.6 Etching 190

A2 LIGA technology 196

LIST OF FIGURES

1. **Fig. 1.1** Comparative influence of field forces on microplates with varying dimensions 3

2. **Fig. 1.2a** Eigenvalues versus side ratio for a simply supported plate rectangular plate from Leissa (1973) 8

3. **Fig. 1.2b** Enlarged view of Fig. 1.2a for the interval $0.95 \leq (a/b)^2 \leq 1.05$ showing curve veering from Leissa (1973) 8

4. **Fig. 2.1** An example of bulk micromachining 24

5. **Fig. 2.2** An example of surface micromachining 24

6. **Fig. 2.3** Cross sectional view showing all 7 layers of the MUMPs process 26

7. **Fig. 2.4** Nitride and Poly 0 layers 30

8. **Fig. 2.5** Oxide 1 and Anchor 1 layers 30

9. **Fig. 2.6** Poly 1 and Oxide 2 layers 32

10. **Fig. 2.7** Poly 2 layer 32

11. **Fig. 2.8** Released structure 33

12. **Fig. 2.9** Layout 34

13. **Fig. 3.1** The electrostatic normal force 42

14. **Fig. 3.2** Electrostatic tangential force 46

15. **Fig 3.3** Sketch of C-C-C-C plate 61

16. **Fig. 3.4** Sketch of C-C-F-F plate 64

17. **Fig. 3.5** Sketch of C-F-C-C plate 65

18. **Fig. 3.6** Sketch of C-F-C-F plate 66

19. **Fig. 3.7** Sketch of F-F-F-C (cantilever) plate 68

20. **Fig. 4.1** Natural frequency versus side ratio for a C-C-C-C microplate 94

21. **Fig. 4.1a** Natural frequency versus side ratio showing curve veering 95

22. **Fig. 4.1b** Curve veering between modes 3-1 and 2-3 at a side ratio of 0.84 96

23. **Fig. 4.1c** Curve veering between modes 2-2 and 1-3 at a side ratio of 0.77 97

24. **Fig 4.1d** Curve veering between modes 2-1 and 2-2 at a side ratio of 0.651 98

25. **Fig. 4.2** Natural frequency showing regions of instability for an applied voltage of 110 volts 100

26. **Fig. 4.2a** Natural frequency versus side ratio for an applied voltage of 110 volts showing curve veering 101

27. **Fig. 4.2b** Curve veering between modes 3-1 and 2-3 at a side ratio of 0.84 102

28. **Fig. 4.2c** Curve veering for modes 2-2 and 1-3 at a side ratio of 0.776 103

29. **Fig. 4.2d** Curve veering for modes 2-1 and 2-2 at a side ratio of 0.66 104

30. **Fig. 4.3** Natural frequency versus side ratio 108

31. **Fig. 4.3a** Natural frequency versus side ratio showing curve veering 109

32. **Fig. 4.3b** Curve veering at a side ratio of 0.825 110

33. **Fig. 4.3c** Curve veering at a side ratio of 0.8 111

34. **Fig. 4.3d** Curve veering at a side ratio of 0.776 112

35. **Fig. 4.3e** Curve veering at a side ratio of 0.68 113

36. **Fig. 4.3f** Curve veering at side ratios of 0.535, 0.486, 0.439 and 0.39 114

37. **Fig. 4.4** Natural frequency showing regions of instability for an applied voltage of 110 volts 115

38. **Fig. 4.5** Natural frequency versus side ratio for C-C-F-F microplate 116

39. **Fig. 4.5a** Natural frequency versus side ratio showing curve veering for a C-C-F-F 117

40. **Fig. 4.5b** Curve veering between modes 3-1 and 2-3 at a side ratio of 0.825 118

41. **Fig. 4.5c** Curve veering between modes 2-2 and 1-3 at a side ratio of 0.535 119

42. **Fig 4.5d** Curve veering between modes 2-1 and 2-2 at a side ratio of 0.44 120

43. **Fig. 4.6** Natural frequency versus side ratio for a C-F-C-C microplate 121

44. **Fig. 4.6a** Natural frequency versus side ratio showing curve veering 122

45. **Fig. 4.6b** Curve veering between modes 2-1 and 2-2 at a side ratio of 0.438 123

46. **Fig. 4.6c** Curve veering between modes 2-2 and 1-3 at a side ratio of 0.535 124

47. **Fig 4.6d** Curve veering between modes 1-2 and 2-1 at a side ratio of 0.68 125

48. **Fig 4.6e** Curve veering between modes 3-1 and 2-3 at a side ratio of 0.825 126

49. **Fig 4.6f** Curve veering between modes 1-3 and 3-1 at a side ratio of 0.922 127

50. **Fig 4.6g** Curve veering between modes 2-3 and 3-2 at a side ratio of 1.067 128

51. **Fig. 4.7** Natural frequency versus side ratio for a C-F-C-F microplate 129

52. **Fig. 4.7a** Natural frequency versus Side Ratio showing curve veering 130

53. **Fig 4.7b** Curve veering between modes 2-1 and 2-2 at a side ratio of 0.39 131

54. **Fig. 4.7c** Curve veering between modes 2-2 and 1-3 at a side ratio of 0.49 132

55. **Fig. 4.7d** Curve veering between modes 2-1 and 1-2 at a side ratio of 0.60 133

56. **Fig. 4.7e** Curve veering between modes 3-1 and 2-3 at a side ratio of 0.68, 1-3 and 3-1 at a side ratio of 0.776 134

57. **Fig. 4.7f** Curve veering between modes 2-3 and 3-2 at a side ratio of 0.92 135

58. **Fig. 4.7g** Curve veering between modes 3-1 and 2-3 at a side ratio of 1.02 136

59. **Fig. 4.8** Natural frequency versus side ratio for a cantilever (F-F-F-C) microplate 137

60. **Fig. 4.8a** Natural frequency versus side ratio showing curve veering 138

61. **Fig. 4.9** Natural frequency versus voltage for various modes of vibration for a C-C-C-C plate 141

62. **Fig. 4.10** Natural frequency showing regions of instability for an applied voltage of 70 volts 143

63. **Fig. 4.11** Natural frequency showing instability for an applied voltage of 80 volts 144

64. **Fig. 4.12** Natural frequency showing instability for an applied voltage of 90 volts 145

65. **Fig. 4.13** Natural frequency versus voltage for various side ratios on a C-C-C-C plate 146

66. **Fig. 4.14a** Natural frequency versus voltage for various modes of vibration for a C-F-C-C microplate 148

67. **Fig. 4.14b** Natural frequency versus voltage for various side ratios on a C-F-C-C microplate 149

68. **Fig. 4.15a** Natural frequency versus voltage for various modes of vibration for a C-F-C-F microplate 150

69. **Fig. 4.15b** Natural frequency versus voltage for various side ratios on a C-F-C-F microplate 151

70. **Fig. 4.16a** Natural frequency versus voltage for various modes of vibration for a C-C-F-F plate 152

71. **Fig. 4.16b** Natural frequency versus voltage for various side ratios on a C-C-F-F plate 153

72. **Fig. 4.17a** Natural frequency versus voltage for various modes of vibration for a F-F-F-C microplate 154

73. **Fig. 4.17b** Natural frequency versus voltage for various side ratios on a F-F-F-C microplate 155

74. **Fig. A1.1** Arrangement of a thermal oxidation system 179

75. **Fig. A1.2** Chemical vapor deposition 181

76. **Fig. A1.3** Evaporation system 183

77. **Fig. A1.4** Sputtering system 185

78. **Fig. A1.5** Examples of correctly exposed, overexposed and underexposed lithographic patterns 189

79. **Fig. A1.6** V-groove etching 193

80. **Fig. A2.1** The LIGA process from Sze (1994) 198

LIST OF TABLES

1. **Table 2.1** Layer names, thickness and lithography levels 27
2. **Table 2.2** Mask conventions 29

3. **Table 4.1** Comparison of non-dimensional natural frequencies 82
4. **Table 4.2** Non-dimensional natural frequencies influenced by various applied voltages for C-C-C-C microplate 83
5. **Table 4.3** Non-dimensional natural frequencies influenced by various applied voltages for C-F-C-C microplate 84
6. **Table 4.4** Non-dimensional natural frequencies influenced by various applied voltages for C-F-C-F microplate 85
7. **Table 4.5** Non-dimensional natural frequencies influenced by various applied voltages for C-C-F-F microplate 86
8. **Table 4.6** Non-dimensional natural frequencies influenced by various applied voltages for Cantilever (F-F-F-C) microplate 87
9. **Table 4.7** Non-dimensional natural frequencies of a C-C-C-C microplate showing the influence of the Casimir effect 88
10. **Table 4.8** Non-dimensional natural frequencies of a F-F-F-C microplate showing the influence of the Casimir effect 89
11. **Table 4.9** Non-dimensional natural frequencies for various boundary conditions at subject to an applied voltage of 20 volts and the Casimir effect 90

NOMENCLATURE

BSG	Borosilicate glass
CMC	Canadian Microelectronics
CVD	Chemical Vapor Deposition
EDM	Electrodischarge machining
EDP	A mixture of ethylenediamine, pyrocatechol and water
HMDS	Hexamethyldisilizane
HNA	A mixture of hydrofluoric acid, nitric acid and acetic acid
IC	Integrated Circuits
KOH	Potassium hydroxide
LIGA	German for *Lithography, Galvanoformung, Abformung*, which stands for lithography, electroplating, and molding
LPCVD	Low Pressure Chemical Vapor Deposition
MEMS	Microelectromechanical Systems
MMT	Micromachine Technology
MOEMS	Micro-optical electromechanical systems
MST	Microsystems Technology
MUMPs	Multi-user MEMS processes
PECVD	Plasma Enhanced Chemical Vapor Deposition
PMMA	Polymethyl-methacrylate
PSG	Phosphosilicate glass
RIE	Reactive ion etching

SOR	Synchrotron orbital radiation
TMAH	Tetramethyl ammonium hydroxide
WEDG	Wire electrodischarge grinding
A	Electrode area
a	Length of microplate, electrode
B	Parabolic rate constant
b	Width of microplate, electrode
c	Velocity of light
D	Flexural rigidity of a uniform rectangular plate
d	Gap between two parallel plates
E	Vacuum energy between two conducting parallel plates, Young's modulus
E_b	The internal energy of the battery
E_c	Energy stored in capacitor
$F_{Casimir}$	Casimir force
F_{elec}	Electrostatic force
F_n	Normal force between electrodes
F_t	Tangential force between electrodes
$\hbar$	Planck's constant
h	Plate thickness
m	Mass per unit area of plate
m,n	No of half waves in x and y directions
Q_c	Charge stored in capacitor
S	Surface area

t	Elapsed time
T_{max}	Maximum kinetic energy
U_{mac}	Maximum potential energy
V	Voltage
w	Transverse deflection of a rectangular plate
x,y	Dimensionless plate Cartesian coordinate directions $[\xi/a\,,\ \eta/b]$
β	Non-dimensional voltage parameter $[\varepsilon V^2a^4/Dd^3]$, correction factor for fringing effects
δx	An infinitesimal distance moved in the x direction
δy	An infinitesimal distance moved in the y direction
α	Side ratio a/b
γ	Non-dimensional Casimir parameter $[\pi^2hca^3/60Dd^5]$
ε	Relative permitivity of the medium between the electrodes
ε_o	Permitivity of a vacuum
$\xi\,,\ \eta$	Cartesian coordinates
λ	Non-dimensional frequency parameter $[\rho h\omega^2a^4/D]$
ν	Poisson's ratio
ρ	Density of material
Φ	Deflection shape of plate in x direction
φ	Deflection shape of plate in y direction
ω	Natural frequency of plate vibration

CHAPTER 1

INTRODUCTION, LITERATURE REVIEW AND THESIS OBJECTIVES

1.1 INTRODUCTION

Micro electromechanical Systems (MEMS) is an enabling technology that yields micromachines that have the size of a grain of salt, integrating mechanical elements such as those for sensing and actuation, and the electronics such as measurements and control circuits, on a common silicon substrate. MEMS applications include optical switches within telecommunication and networking systems, accelerometers found in safety airbags in automobiles, inkjets in desktop printers and sensors in medical equipment, among other numerous and wide applications. This technology results in substantial cost benefits, directly through low unit pricing, or indirectly by cutting service and maintenance costs.

The design, analysis and fabrication of devices with micron and sub-micron dimensions requires the collaboration and specialist knowledge from diverse fields such as mechanics, materials science, physics and mechanical engineering among others to effectively reach a pragmatic goal. Furthermore, the performance of the micro-systems must be evaluated before the systems are created because they have to be coupled with the appropriate electronic circuits. In order to achieve this, it is imperative to perform static and dynamic analyses on mechanically designed systems in order to evaluate the influence of the various parameters on the system dynamic behaviour. The results of the

analysis provides useful information that the designer uses to predict various system responses that may be of interest for a particular application, ensuring the ultimate integrity of the product as it fulfils the function for which it was conceived.

As in the case of any engineering component, modeling and simulation of micro electromechanical devices are essential for a better understanding of their functionality and optimal design. The development of increasingly complex MEMS demands sophisticated simulation techniques for design and optimization.

MEMS devices typically involve multiple coupled energy domains and media such as coupled electrostatic, electromagnetic, elastodynamic, thermal and fluid dynamic interactions giving rise to an interdisciplinary domain type of mathematical model depending on the type of application. Although most of the captured phenomena experience non-linear behaviour it has been common to assume linearity to simplify the mathematical model. The resulting simulation however is nontrivial because, in general, it involves coupled partial differential equations. Often the functionality of these devices can only be captured with time dependent non-linear partial differential equations.

With advances in MEMS, the gap between plates in capacitive type devices has fallen down to micrometer and sub-micron levels where the influence of field forces, such as electrostatic and Casimir forces (Casimir and Polder, 1948), on the dynamic behaviour of the plates cannot be ignored.

As the device feature size reduces to sub-micron levels, fringing effects, van der Waals type interactions and quantum effects, dominated by the Casimir effect, significantly influence the response and performance of MEMS devices and must be taken into account. Fig. 1.1 illustrates the effect of a variation in typical dimensions of a microplate with the dominant forces present. The microplate is assumed with the side square in microns as indicated below on the double logarithmic scale.

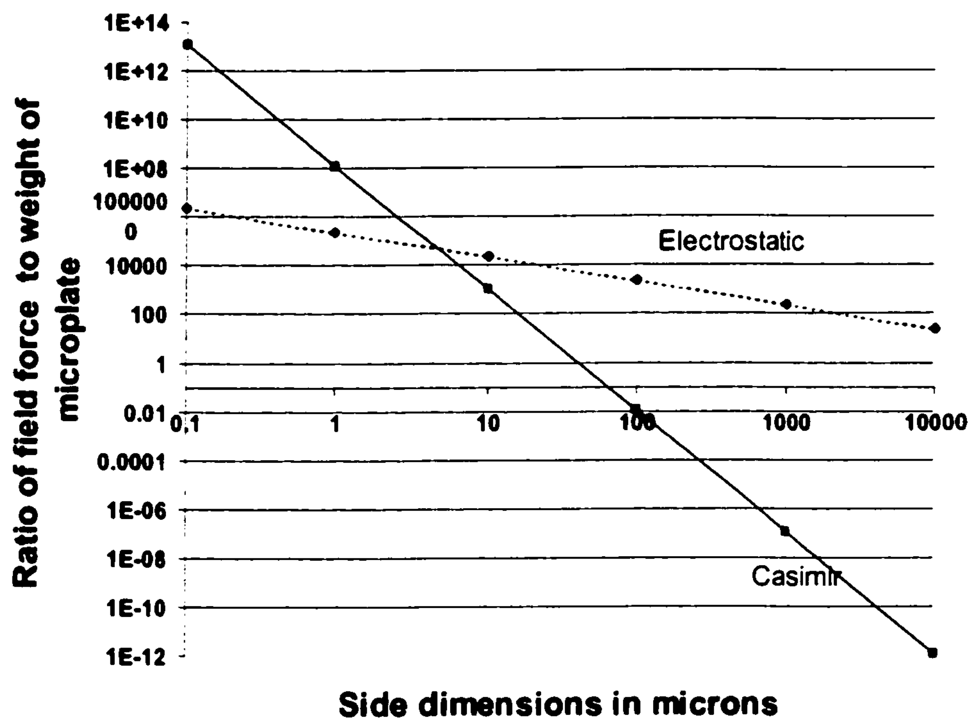

Fig. 1.1 Comparative influence of field forces on microplates with varying dimensions

Solution of the complex, coupled partial differential equations in a multi-domain environment can be carried out in closed form only in a limited number of cases. Approximate solution techniques must be employed in order to understand the dynamic behaviour of such microsystems. In view of the inherent limitations of such approximate techniques, the solutions that should be identical may be constrained to be unequal. Such an example is the use of approximate methods to compute the natural frequencies of square, homogeneous plates under small deflections. The natural frequencies corresponding to the *m-n* and *n-m* modes should have identical natural frequencies, however, approximate methods such as the Rayleigh-Ritz method predict the natural frequency of the *m-n* mode to be slightly different from the corresponding *n-m* mode. When the variation of such natural frequencies is plotted against the side ratio of the rectangular plate, instead of crossing at a side ratio of unity, they veer away from each other in an abrupt but continuous manner. This phenomenon is commonly referred to as *curve veering*.

Curve veering in structural dynamics is invariably due to the approximation in the analysis. Curve veering indicates the degree of approximation involved which would affect the subsequent response calculations, which in turn will influence the design. Hence the study of curve veering is important in order to reveal the degree of approximation in the analysis.

This thesis investigates the curve veering phenomenon resulting from the vibration analysis of the microplate. Particular consideration is given to the mixed domain effect

of the elastic forces and field forces, arising from electrostatic capacitive forces and the Casimir effect, on the dynamic response of the micro plate. The emphasis is on the curve veering aspects of the micro-plate dynamics and an analytical study of the influence of voltage and side dimensions with various boundary conditions on the natural frequencies of the microplate. The field forces introduce non-linearity into the problem formulation. The thermal energy effects, which in general introduce residual stresses, are neglected in this formulation. The plate design is described and carried out using commercially available software – MEMSPro Version 3. In studying the curve veering behaviour resulting from the response of the microplate in the presence of the aforementioned forces, the multiplicity of curve veering in the parametric region of interest is demonstrated. The implications of this phenomenon on the design of systems that incorporate such features are discussed. The process of achieving this will result in the presentation of a typical design in the Multi-User MEMS Processes (MUMPs) and the post-processing for a capacitive type microplate structure. Analytical results incorporating these field forces will be presented with a discussion of the influence of variations in the system parameters and boundary conditions on the natural frequencies of the microplates.

1.2 CURVE VEERING

Curve veering is a phenomenon in which the plot of eigenvalues of a system against a system parameter sometimes results in curves that abruptly veer away from each other in a rapid but continuous manner at points where they are expected to intersect. Certain modes of vibration of the natural frequencies of rectangular plate structures obtained from an exact analysis are expected to intersect. However approximate analysis would invariably indicate such curves veering away at those points. Occurrence of curve veering indicates the extent of approximation involved and introduces considerable error when interpreting the results obtained. Hence it is important to understand this phenomenon from a design perspective.

In the frequency analysis of rectangular plates using a two- term Ritz solution with beam functions, Warburton (1954) observed that frequency curves plotted against a system parameter such as the side ratio behaved smoothly everywhere except in regions where they tend to cross each other but strongly veer away. Claassen and Thorne (1962), in their work on the vibration of rectangular cantilever plates, obtained similar frequency plots which exhibited this same behaviour in a region they termed the "transition zone". Leissa (1974) demonstrated this *curve veering* aberration using the well-known solution to the problem of a vibrating membrane. When an exact solution was used to obtain the natural frequencies, curve veering was not present. However, this was shown to occur when another approximate method, the Galerkin Method, was used to obtain the frequency curves. The plots shown in Fig. 1.2 illustrate this point. The curves corresponding to λ^2_{31} and λ^2_{13} plotted against the aspect ratio veered away from each other

at a certain value of aspect ratio. Using an exact solution, the corresponding curves crossed at $a/b = 1$. Leissa (1973) had shown that for a rectangular plate there are 21 distinct cases having clamped, simply supported, or free boundaries. Exact solutions exist for six of these cases – those having at least two opposite edges simply supported. He went on to show that frequency coalescence was exhibited in these curves while the other fifteen having approximate solutions exhibited curve veering.

Perkins and Mote (1986) report this phenomenon for a general eigenvalue problem in which a characteristic of curve veering is that the eigenfunctions associated with the eigenvalues on each locus before veering are interchanged during veering in a rapid and continuous manner. They establish criteria for differentiating between a veering and a crossing. Similarly, Chen and Ginsberg (1992) establish criteria governing the occurrence of curve veering using perturbation methods of analysis to relate the eigenvalues of a system to a system parameter. They go on to show that in the region of veering, the eigenfunctions are linear combinations of the corresponding eigenfunctions at the outer limits of the veering zone, and that those combinations are highly sensitive to the value of the system parameter. Though associated with eigenvalue solutions obtained by approximate methods, Schajer (1982) has shown that curve veering can occur for certain problems that have exact solutions. Kuttler and Sigillito (1981) conclude that curve veering is as a result of the mathematical model used and not necessarily because of an approximate technique employed in obtaining an eigenvalue solution. Tsai (1993) shows that using an approximate method such as the finite difference method does not result in curve veering of eigenvalue loci and suggests that the existence of curve veering

in three-dimensional problems implies that it is a phenomenon in the real world. Bhat (2000) in his investigation of this phenomenon shows that curve veering is an inherent behaviour of some vibrating systems and not limited to systems that have approximate solutions only.

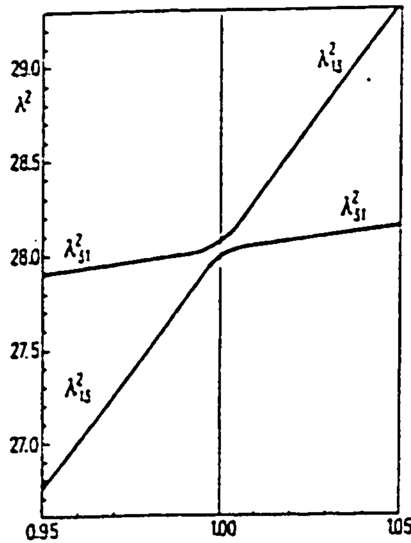

Fig. 1.2a Eigenvalues versus side ratio for a simply supported rectangular plate from Leissa (1973)

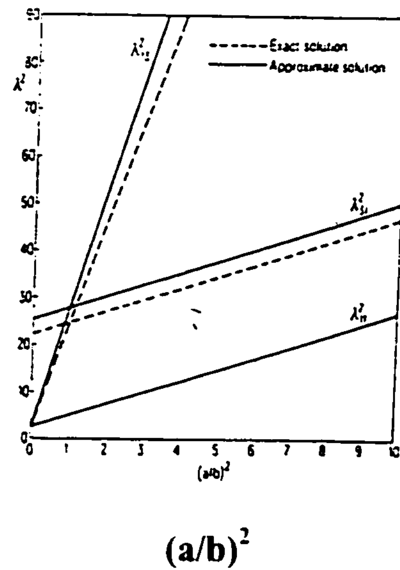

$(a/b)^2$

Fig. 1.2b Enlarged view of Fig. 1.2a for the interval $0.95 \le (a/b)^2 \le 1.05$ **showing curve veering from Leissa (1973)**

1.3 ELECTROSTATIC FORCES IN MEMS

An electrostatic actuation force field is established between two plates connected to a difference of potential. The charges on two objects with an externally applied potential between them can only be of opposite polarities. Therefore an applied voltage, regardless of its polarity, always results in an attractive electrostatic force.

In capacitive type MEMS such as micro sensors and micro actuators the electrostatic forces acting on plate elements prove to have a strong influence on its dynamic behaviour. In general not much attention had been given to the influence of the electrostatic field on the dynamic behaviour of the flexible capacitor plate elements. For example in early studies on polarized and pre-polarized electromechanical systems such as microphones (Morse, 1948), the influence of the electrostatic field on the dynamics of the system was not considered. However, in capacitive micro devices these effects cannot be ignored.

Puers and Lapadatu (1996) studied the effects of electrostatic forces on the measurements and fabrication process of capacitive mechanical sensors. Their investigation recognized the undesirable presence of instability in the form of stiction and go on to propose ways to avoid this. In considering a particle method for the analysis of micro electromechanical switches, (Aluru, 1998) describes a meshless technique which can be used for the analysis of a complicated micro device in which mixed – energy domains requiring different numerical methods to solve, are present. In that paper the governing equations include the effects of electrostatic forces. Ye and Mukherjee (1998) account

for these effects in the design and fabrication of an electrostatic variable gap comb drive. Large-displacement electrostatic actuators (for instance comb drives) produce small forces whereas large force actuators (such as parallel plate capacitive structures) result in small displacements. In order to overcome this, Jebens et al (1989) proposed curved actuators to obtain relatively large displacement and forces. Legtenberg et al (1997) investigate the static behaviour of the cantilever as it is pulled into contact with the rigid fixed-electrode structure resulting in stiction.

Designs requiring a critical and accurate assessment of gap to forestall surface contact would necessitate an analysis that incorporates all field forces that are significant in a given range. In generating efficient dynamic models for MEMS from a few finite element simulation runs, a mixed domain type model is obtained by Hung and Senturia (1999), which included the electrostatic effect. Chan et al (1999) study the electrostatic actuation of a beam in contact with an underlying silicon nitride layer resulting in stiction. Their work took into consideration electrical effects of fringing fields and surface effects in the characterisation that was carried out. The design was done in the multi-user MEMS process (MUMPs) technology that is used in the design and fabrication process enunciated in the present thesis. Bingqian et al (1999) reported that the electrostatic effect is further influenced by the space charge in sub-micron structures and is dominated by the distance and doping concentration.

Packisiramy et al (1997) considered the effect of electrostatic charge on plate structures in a static deflection analysis of a condenser microphone. Ziebart et al (1999) investigated theoretically and experimentally the buckling of square micromachined membranes, providing a useful sensing and actuation principle for micro-plate structures. In studying the dynamic response of microplates in an electrostatic field by Stiharu and Bhat (1997), a linearization of the voltage term was done and boundary characteristic orthogonal polynomials were used in the Rayleigh - Ritz method of analysis to obtain the approximate response. The non-linearity inherent in the problem formulation was addressed by Rajalingham and Bhat, (1998), and Chakraverty et al (2000) using a perturbation method to obtain the influence of an electric field on the stability and natural vibration of diaphragms in MEMS such as in micro sensors and actuators. Saif et al (1999) studied the analytical modeling of membranes that are electrostatically actuated as considered in the design of micro pumps.

Furthermore, it is known that the mechanical properties of micro and sub-micron structural elements differ from that predicted by continuum mechanics as reported by Miller and Shenoy (2000) and Namazu et al (2000). Similar thought should be extended to considerations of the applicable field forces in generating mathematical models for analysis.

1.4 CASIMIR FORCE IN MEMS

In microstructures, the electrostatic forces can be stronger than the electromagnetic forces (Trimmer and Jebens, 1989). However at sub-micron levels and in the absence of electrostatic forces, quantum fluctuations can give rise to the Casimir effect (Casimir and Polder, 1948).

The Casimir effect in its simplest form is due to the interaction of a pair of neutral, parallel conducting planes, arising as a result of the disturbance of the vacuum electromagnetic field between the planes. There is no force between the plates in classical electrodynamics, since the plates are assumed neutral. In the presence of the plates, the boundary conditions on the electromagnetic field are altered from the free field conditions resulting in an energy density in the space between the opposing parallel plates being less than that outside the plates (Serry et al, 1995). The attraction between the plates results from a quantum effect caused by the vacuum between them; the ground state of quantum electrodynamics (QED) causes the plates to attract each other. In quantum field theory it was previously assumed that the infinite vacuum energy of free space is zero (Itzykson and Zuber, 1980). However, there is a finite difference between the infinite vacuum energy densities in the presence of the plates and in free space, and is observable giving rise to the Casimir force. In the theoretical approach to its explanation, the Casimir force sometimes referred to as the retarded van der Waals force (Milonni, 1994) arises as a result of the coherent, non-zero, correlated oscillations of the induced atomic dipole moments of a great number of atoms belonging to the different boundary bodies.

These quantum fluctuations tend to produce dominant electromagnetic components (Bordag et al, 1995). This results in attractive or repulsive forces depending on the geometry, topology and boundary conditions of the separate bodies. When the distance between the surfaces is much less than 1 μm, the force becomes the unretarded van der Waal's force having its greatest effect on capacitive MEMS in this range. Serry et al (1998) have investigated the role of the Casimir effect in the static deflection and stiction of membrane strips in MEMS and propose parametric criteria for establishing the collapse of a MEMS device analyzed using the principles enunciated in their paper.

Though quantum in nature, it is possible to predict forces between macroscopic bodies. It is strongly dependent on shape, being attractive or repulsive. These forces are also dependent on temperature, and on the electrical and mechanical properties of the boundary surface (Mamaev and Trunov, 1979).

In an extensive review on new developments in the study of the Casimir effect, Bordag et al (2001) derive the well known formula for the vacuum energy between two conducting parallel plates at zero temperature. In this report it is shown that for situations where the boundaries are in motion, i.e. dependent on time, there arises what is referred to as the Dynamic Casimir Effect. As a direct consequence of the dynamic behaviour, is the dependence of the Casimir force on time.

Bordag et al, (2001) also derived a general expression for the van der Waals and Casimir force, which can be generalized for a system of plane, parallel, stratified layers of various

materials. Further work in deriving the Casimir force for anisotropic plates was carried out by Mostepanenko and Trunov, (1997), in which it was concluded that anisotropic plates induce a torque in addition to the vacuum force, which results in a change of the mutual orientation of the bodies.

Lukosz (1971) reported the variation of the vacuum Casimir energy inside a rectangular box after which Mamaev and Trunov (1979) subsequently derived this energy with in terms of the dimensions of the box. Ambjorn and Wolfram (1983), obtained the Casimir energy for the general case of a hypercuboidal region with n sides. Li et al (1997) investigated the relationship between the Casimir energy and the boundary conditions of the conducting surfaces. In their work, it was seen that the sign of the energy was dependent on the type of boundary conditions.

In Mamaev (1979) and Bordag et al (2001) the Casimir energy for a rectangular cavity with perfectly conducting faces of sides a_1, a_2, a_3 and encompassing an electromagnetic vacuum is derived.

It is interesting to note that the energy can produce attractive or repulsive forces, depending on the relative dimensions of the sides of the rectangular cavity. Milton and Ng (1998) obtained similar results for the repulsive Casimir forces on the interior of a sphere. Macklay (2000) computed similar results for the Casimir forces and energies of rectangular cavities with varying side lengths.

The Casimir effect for a cylinder was initially investigated by DeRaad and Milton (1981). The associated force with this energy is attractive. The exact analytical calculation of Casimir energies and forces is only possible for configurations that are symmetrical. In experimental methods of interest that require the calculation of these quantities for non-symmetrical systems such as a sphere suspended over a disk, approximate methods of solutions are employed.

All of the foregoing has been based on static considerations of the Casimir energies and forces. In the case where the gap is dependent on time, the so-called Dynamical Casimir Effect arises. The dynamics of a moving boundary results in a dependence of the Casimir force on the velocity and requires a correction to accurately account for this. However, the error that arises from this velocity dependence for an electromagnetic field is very small being less than 8% of the static value as estimated by Bordag et al (2001). Another effect of the moving boundaries is a quantum effect that manifests in the creation of photons from a vacuum.

The above results for the Casimir energies and forces are valid for ideal situations of perfect conductivity and zero temperature, necessitating corrections that will arise in the use of real environment. These corrections arise from the non-zero temperatures, finite conductivity, surface roughness characterized by imperfections in geometry or stochastically varying surface. Real environment may require any one or a combination of these corrections.

The influence of finite conductivity on the Casimir force, which requires a correction of 10 to 20 % of the result at separations of about 1 micron, has been well documented in Bordag et al (2001). This study also derives in detail the effect of these corrections and their combinations on the Casimir force. Arnold et al (1979) propose correction factors for a variety of surfaces, which are successfully used by Serry et al (1995 and 1998) in their reported work on the Casimir effect in microelectromechanical systems.

The experimental measurement of the Casimir force has proved to be challenging to researchers primarily due to the fact that it is such a small quantity, being about 10^{-7} N for parallel, infinitely conducting, flat surfaces of 1 cm^3 and a separation of 1 μm. Sparnaay (1989) was the first to conduct experiments to verify the theoretical results used in predicting the Casimir force. Lamoraeux (1997) has carried out experimental investigations on the Casimir effect using a torsion pendulum. In this work, he pointed out the significant corrections required to surface temperature for separations greater than 1 μm. These amounts to 86%, 129% and 174% of the zero temperature values at separations of 4, 5 and 6 μm, respectively. However at smaller separations the absolute error decreases significantly.

Significant improvement in these measurements came with the use of an Atomic Force Microscope (AFM) by Mohideen and Roy (1998). Roy and Mohideen (1999) demonstrated the geometrical and boundary dependence of the Casimir force in which it was measured for a sphere suspended over a corrugated plate. Gold is the preferred material of choice for test measurements due to its chemical inertness. Harris et al (2000)

have produced the most accurate measure of the Casimir force using gold, with errors of less than 1%, accounting for the various correcting factors of temperature, finite conductivity and surface roughness, respectively.

Bordag et al (2001) review the various experimental techniques used in discussing the merits and demerits of each method. Limitations in measurements include such factors as the force sensitivity of the measuring apparatus, reproducible measurement of plate separation (or more generally separation of the bodies), residual electrostatic charges, and complex geometry such as for a torus.

Despite the advances in the experimental measurement of the Casimir force, researchers have only been able to obtain results in the range of separation of between 0.032 μm to 1μm. In order to further enhance the accuracy of Casimir force measurements, Bordag et al (2001) propose techniques that will incorporate the use of the AFM by lithographic fabrication of cantilevers with large radius of curvature and interferometric detection of cantilever deflection among others. They suggest that dynamic measurements might lead to substantial increase in the sensitivity in future work.

The small separation between neighboring surfaces in various MEMS devices means it is possible that the presence of Casimir forces may result in adjacent surfaces being attracted to or sticking to each other (Serry et al, 1998, Bordag et al, 2001) referred to as stiction.

Using AFM methods Macklay (2000) investigated the variation in vacuum energy and vacuum forces in micro fabricated structures. He has also given specific attention to the use of the Casimir Force in design of microelectromechanical systems (MEMS). Serry et al (1995) had given consideration to the Casimir effect in the Anharmonic Casimir Oscillator (ACO), using this effect to explain the phenomenon of stiction that occurs in MEMS. Their work proposes applications of the ACO in the design of a Casimir switch. They had further investigated the role of the Casimir effect on the static deflection and occurrence of stiction in membranes (Serry et al, 1998). Chan et al (2001) designed and fabricated an actuator operated on the basis of the Casimir force using silicon nanofabrication technology.

Thus far, no studies have been conducted on the influence of the Casimir force on the natural frequencies of a microfabricated structure. In this thesis, the general results for the Casimir force for a pair of conducting parallel plates is used in modelling of the microplate in order to investigate the influence it would have on the curve veering in capacitive type microelectromechanical systems and parametric variations that may lead to instability of the system.

1.5 MOTIVATION, METHODS AND OBJECTIVES

MEMS structures promise a huge potential in microsensor development. Among various measurement principles, capacitive type of measurement has a major advantage over the piezo-resistive or piezo-electric principles, namely the small offset due to temperature. However, these miniature structures experience major challenges in capacitive type measurements. MEMS structures are conceived with very simple geometries hence the use of flexible plates that would change deflection according to an input signal is quite common.

The analysis of such systems using an approximate method introduces errors. One of such is the phenomenon of curve veering, which has not been considered in application to MEMS structures. An implication of curve veering introduced by approximate analysis is made more apparent in the estimation of natural frequencies for capacitive microplates used as MEMS actuators, which may introduce considerable error in the interpretation of results obtained. Furthermore, parametric studies are important for a better understanding of the behaviour of the systems under consideration and the factors that affect stability. To the best of our knowledge, the reported studies in the literature have not taken into account the geometric parameter of side ratio (the ratio of the length to width), which is a key parameter for determining the plate dimensions in the design process. Additionally, the effect of a change in boundary conditions on the stability of capacitive MEMS structures is also taken into consideration.

The curve veering behaviour of a capacitive microelectromechanical system (MEMS) subject to load intensities arising from electrostatic and Casimir forces is investigated. The capacitive system studied is modeled as a pair of parallel plates, the design of which is done in the MUMPs technology using MEMSPro version 3 and is presented as the basis for the analysis. A mathematical model describing the complete effect of these forces on a pair of parallel conductive plates is developed. A mixed domain type model is obtained. The response of the system from the point of view of curve veering is subsequently obtained from a solution of the resulting governing non-linear equations using a suitable approximation technique, namely the Rayleigh-Ritz method. In the present study, the natural frequencies of a microplate subjected to an electrostatic field and the Casimir force are obtained and the curve veering behaviour for this system is examined. The plate considered is a typical structural element of a microelectromechanical system (MEMS) device that finds application in sensors, actuators and switches. Various boundary conditions of the microplate are considered. An approximate analysis is carried out using boundary characteristic orthogonal polynomials in the Rayleigh-Ritz method to obtain the natural frequencies for a given set of system parameters. The non-dimensional natural frequencies are plotted against the side ratio. The results of this frequency analysis are used to demonstrate the curve veering phenomena in more than one location corresponding to a particular normal mode.

A parametric study of the influence of various parameters on the behaviour of the system is presented. Consideration is given to such relations as the influence of the gap between plates, voltage, plate side dimensions, as well as type of boundary conditions and the

contributing effect of the electrostatic and Casimir forces from the micro to the nanometer range, on the natural frequency of vibration of the micro plate.

It is hoped that motivation for potentially new concepts and contributions to facilitate the design process of capacitive microstructures may evolve in the course of this study. This study also seeks to provide MEMS analysts and designers with a convenient framework useful in assessing which field forces are necessary for consideration in various ranges of scale from micrometer to sub-micron levels for capacitive micro devices. The investigation of the curve veering is expected to yield results that will give a deeper insight into this phenomenon as applied to the vibration of microplates across a given range of aspect ratios for a given set of boundary conditions. This is with a view to providing designers, engineers and scientists with new information and considerations for enhanced and more accurate modelling work.

The parametric study will contribute to the provision of a useful guide in the proposal of dimensions and boundary conditions that will avoid the occurrence of plate instability arising from stiction effects under operational conditions that involve the field effects considered here in the given range.

CHAPTER 2

DESIGN AND FABRICATION

2.1 INTRODUCTION TO MICROELECTROMECHANICAL SYSTEMS

In the early 1960s, the renowned physicist, Richard Feynman postulated on the possibility of producing new machines with a new miniaturized machining technology using televised robot arms in the microscopic world (Feynman, 1961). It was not until the 1980s did serious consideration to this thought translate to pioneering research in this area. Subsequent to a flurry of research activity at this time notably in Europe, Japan and North America, Gabriel et al (1988) reported on the interdisciplinary technologies and explained the future possibilities of this emerging technology. This report helped to generate interest and funding by the National Science Foundation of the United States of America with grants of $105 million and $200 million dollars in 1988 and 1989, respectively, for the formal commencement of MEMS research and development projects. In other parts of the world funding and research went on simultaneously. Erfeld et al (1986, 1987 and 1988), among others in Germany reported on the use of LIGA technology in the fabrication of MEMS. Japanese researchers began micromachine projects through pioneering works from Fujita and Omadaka (1987), among several others. The various approaches used in the research and development of micromachine technology has led to it being referred to by different names. In Europe it is called microsystems technology (MST), in Japan it is referred to as micromachine technology (MMT) and in North America it has the name microelectromechanical systems (MEMS).

Essentially it is an enabling technology that yields micromachines that have the size of a grain of salt, integrating mechanical elements such as sensors and actuators, and the electronics such as measurements and control circuits, on a common silicon substrate. MEMS applications include optical switches within telecommunication and networking systems, accelerometers in automotive airbags, inkjets in desktop printers and sensors in medical equipment, among other numerous and wide applications. This technology results in substantial cost benefits, directly through low unit pricing, or indirectly by cutting service and maintenance costs.

MEMS fabrication capitalizes heavily on the well-established lithographic processes used in the planar processing of integrated circuits using silicon technology. Prior to the onset of widespread interest in MEMS, Tufte et al (1962) had used silicon for the first time as both a mechanical and sensing material, developing a pressure transducer. Samaun et al (1973) and Wen et al (1979) used masked anisotropic etching to batch fabricate silicon pressure transducers with the planar steps developed for silicon transistors and integrated circuits. The result was a batch fabricated pressure transducer in what is termed a bulk micromachining process and is shown in Fig. 2.1.

The last decade has witnessed a remarkable advancement in the research and development of available technologies used in the fabrication of micro electromechanical systems (MEMS). Product demand driven by industrial, commercial and military applications has encouraged certain design methods and technologies for fabrication over others. The most common methods currently engaged in are discussed in the appendix.

A specific design that has been carried out using MEMSPro and submitted to the Canadian Microelectronics Corporation (CMC) for fabrication and packaging is presented in this chapter followed by a discussion of the method used in the post processing of the design which is carried out entirely in the Multi-User MEMS Processes (MUMPs) developed by researchers at the Berkeley Sensors and Actuators Center of the University of California at Berkeley in the late 1980's and early 1990's.

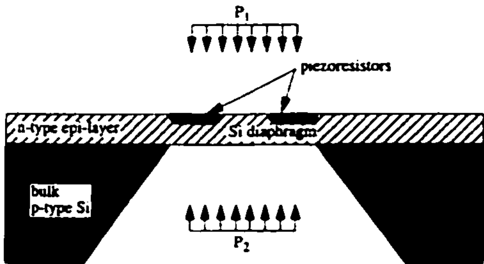

Fig. 2.1 An example of bulk micromachining

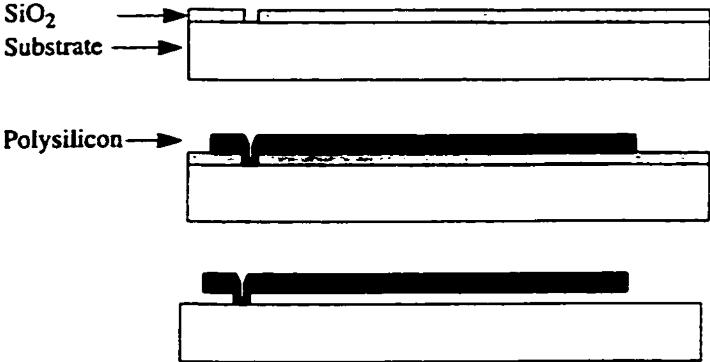

Fig. 2.2 An example of surface micromachining

2.2 DESIGN AND FABRICATION OF A MICROPLATE

In order to study the effect of curve veering on a microplate subject to an electrostatic force and the Casimir effect, the design and fabrication of the proposed structure for analysis is presented.

The microplate is designed and fabricated in the Multi-User MEMS Processes (MUMPs) using a commercial Computer-Aided Design (CAD) software tool, MEMSPro version 3. MUMPs offered by Cronos Integrated Systems, is a process that provides the international, industrial, governmental and academic communities with cost-effective, proof-of-concept surface micromachining fabrication. It is designed for general-purpose micromachining by outside users who would like to fabricate MEMS devices.

The MUMPs process is a three-layer polysilicon surface micromachining process enabling increased flexibility and versatility for the multi-user environment. A general description of the three-layer polysilicon surface micromachining MUMPs process is illustrated in Fig. 2.3 and tabulated in Table 2.1. This process has the general features of a standard surface micromachining process:

1. Polysilicon is used as the structural material
2. Deposited oxide (PSG) is used as the sacrificial layer
3. Silicon nitride is used as electrical isolation between the polysilicon and the substrate.

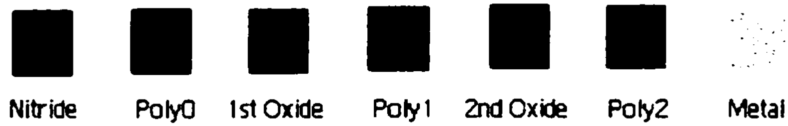

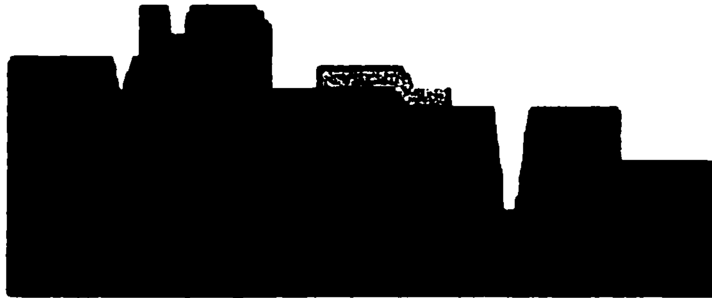

Fig. 2.3 Cross-sectional view showing all 7 layers of the MUMPs process (from the MUMPs Design Handbook)

Material Layer	Thickness (μm)	Lithography Level Name
Nitride	0.6	-
Poly 0	0.5	POLY0 (HOLE0)
First Oxide	2.0	DIMPLE ANCHOR1
Poly 1	2.0	POLY1 (HOLE1)
Second Oxide	0.75	POLY1_POLY2_VIA ANCHOR2
Poly 2	1.5	POLY2 (HOLE2)
Metal	0.5	METAL (HOLEM)

Table 2.1 Layer names, thicknesses and lithography levels.

(Hole levels are printed on the same line as their corresponding polysilicon or metal levels (MUMPs Handbook, 2001)

The process is different from most customized surface micromachining processes by the fact that it is designed to be as general as possible, and is capable of supporting many different designs on a single silicon wafer. Since the process was not optimized with the purpose of fabricating any specific device, the thickness of the structural and sacrificial layers were chosen to suit most users, and the layout design rules were defined conservatively to guarantee the highest yield possible. Hence it proved to be a suitable choice of technology in which to carry out our design for the present thesis.

In order to facilitate the production of a good design that can be successfully manufactured, it is imperative to conform to the design rules pertaining to feature size, spacing, enclosures and other considerations that must be adhered to. The MUMPs Design Handbook (2001) is an excellent reference material for this purpose. The rules are input in the setup for MEMSPro prior to commencement of the design process.

2.2.1 Process Design

It is imperative to have a perfect understanding of the design process to produce realistic analytical results for MEMS devices. Implications of the fabrication process requirements on the design and subsequent analysis should be clearly understood and taken into account. Such issues that may arise include geometric constrains on thickness and gap, perforations in the plates necessary for release and step up clamping conditions that affect the assumed boundary conditions.

The process flow for the design of a capacitive microelectromechanical structure modeled by a microplate used for analysis is presented in the following. MEMSPro version 3 is used to produce detailed drawings for the design and is shown in the accompanying figures for each step of the process flow. The conventions used in the various layer names are stated in Table 2.2.

Step 1: The Wafer

The process begins with 100 mm n-type (100) silicon wafers of 1-2 Ω-cm resistivity. The surface of the wafers is first heavily doped with phosphorus in a standard diffusion furnace. This helps to reduce or prevent charge feed-through to the substrate from electrostatic devices on the surface.

Mnemonic level name	Field type	Purpose
POLY0	light	pattern ground plane
ANCHOR1	dark	open holes for Poly 1 to Nitride or Poly 0 connection
DIMPLE	dark	create dimples/bushings for Poly 1
POLY1	light	pattern Poly 1
POLY1_POLY2_VIA	dark	open holes for Poly 1 to Poly 2 connection
ANCHOR2	dark	open holes for Poly 2 to Nitride or Poly 0 connection
POLY2	light	pattern Poly 2
METAL	light	pattern Metal
HOLE0	dark	provide holes for POLY0
HOLE1	dark	provide release holes for POLY1
HOLE2	dark	provide release holes for POLY2
HOLEM	dark	provide release holes in METAL

Table 2.2 Mask Conventions

Step 2: Silicon nitride layer

Next, a 600 nm low-stress LPCVD (low pressure chemical vapor deposition) silicon nitride layer is deposited in a conformal manner on the wafers as an electrical insulation layer.

Step 3: Poly 0 layer deposition and patterning

This is followed directly by a conformal deposition of 500 nm LPCVD polysilicon film- Poly 0. It is then patterned by photolithography, a process that includes the coating of the wafers with photoresist, exposure of the photoresist with the appropriate mask and developing the exposed photoresist to create the desired etch mask for subsequent pattern transfer into the underlying layer. After patterning the photoresist, the Poly 0 layer is etched in an RIE (Reactive Ion Etch) system to a depth of 0.5 μm on the outside (Fig. 2.4).

Fig. 2.4 Nitride and Poly 0 layers

Step 4: First oxide layer deposition and patterning

A 2.0 μm phosphosilicate glass (PSG) sacrificial layer is then deposited as a fill by LPCVD as shown in Fig. 2.5 and annealed at 1 050°C for 1 hour in argon. This layer of PSG, known as First Oxide, is removed at the end of the process in a ***post-processing*** step (described in a later section), to free the first mechanical layer of polysilicon. The wafers are then patterned with the second mask layer, ANCHOR1, and reactive ion etched on the inside to a depth of 2.5 μm This step provides anchor holes that will be filled by the Poly 1 layer.

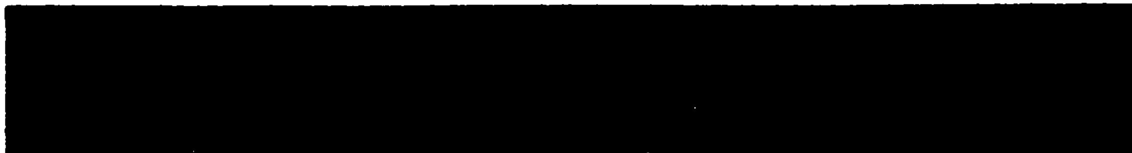

Fig. 2.5 Oxide 1 and Anchor 1 layers

Step 5: Poly 1 layer deposition and patterning

After etching ANCHOR 1, the first structural layer of polysilicon (Poly 1) is deposited to a thickness of 2.0 μm as a fill. A thin 200 nm layer of PSG is deposited over the polysilicon and the wafer is annealed at 1050°C for 1 hour. The anneal dopes the polysilicon with phosphorus from the PSG layers both above and below it. Annealing also serves to significantly reduce the net stress in the Poly 1 layer. The polysilicon and its PSG masking layer is lithographically patterned using a mask designed to form the first structural layer POLY1. The PSG layer is etched to produce a *hard mask* for subsequent polysilicon etch. The hard mask is more resistant to the polysilicon etch chemistry than the photoresist and ensures better transfer of the pattern into the polysilicon. The POLY1 is reactive ion etched on the outside to a depth of 2 μm. After etching the polysilicon (Fig. 2.6), the photoresist is stripped and the remaining oxide hard mask is removed by RIE.

Step 6: Second oxide layer deposition and patterning

After Poly 1 is etched, a second PSG layer, the second oxide, is deposited as a fill with a thickness of 0.75 μm and annealed as shown in Fig. 2.6. The second oxide is patterned using two different etch masks with different objectives. The first, an ANCHOR2 level mask is provided to etch both the first and second oxide layers in one step, thereby eliminating any misalignment between separately etched holes. More importantly, the ANCHOR2 etch eliminates the need to make a cut in first oxide unrelated to anchoring a Poly 1 structure, which needlessly exposes the substrate to subsequent processing that

can damage either Poly 0 or Nitride. The ANCHOR2 layer is lithographically patterned and etched by RIE to a depth of 5.25 μm on the inside.

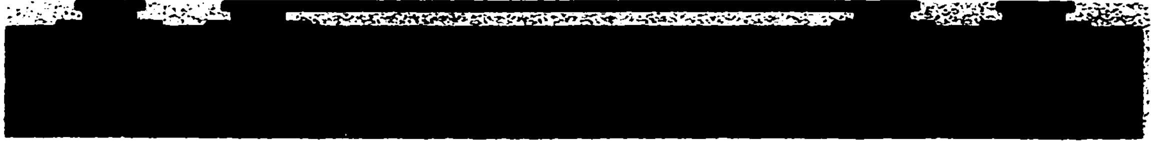

Fig. 2.6 Poly 1 and Oxide 2 layers

Step 7: Poly 2 layer deposition and patterning

The second structural layer, Poly 2, is then deposited in a conformal manner to a thickness of 1.5 μm followed by the deposition of 200 nm PSG. As with Poly 1, the thin PSG layer acts as both an etch mask and dopant source for Poly 2. The wafer is annealed for one hour at 1050 °C to dope the polysilicon and reduce the residual film stress. The Poly 2 layer is lithographically patterned with the POLY2 mask and the PSG and polysilicon layers are etched by RIE using the same processing conditions as for Poly 1. The photoresist then is stripped and the masking oxide is removed (Fig. 2.7).

Fig. 2.7 Poly2 layer

Step 8: Poly1_Poly 2 Via etch

POLY1_POLY2_VIA level mask is the second mask used to pattern the second oxide layer. It provides for etch holes in the second oxide down to the Poly 1 layer, also acting as a mechanical and electrical connection between the Poly 1 and Poly 2 layers. The POLY1_POLY2_VIA layer is lithographically patterned and etched by RIE to a depth of 1 µm on the inside.

Step 9: Metal layer deposition and patterning

The final deposited layer in the MUMPs process is a 0.5 µm metal layer that provides for probing, bonding, electrical routing and highly reflective mirror surfaces. The wafer is patterned lithographically with the mask, METAL and the metal is deposited and patterned using lift-off. Fig. 2.8 shows the device after sacrificial oxide release. The release is performed in a post-processing step described shortly.

Fig. 2.8 Released structure

2.2.2 LAYOUT DESIGN

The geometric design is done using the layout editor of MEMSPro Version 3 and is shown in Fig. 2.9. The geometry is constrained by adherence to the design rules for the MUMPs process and summarized in the handbook. In order to facilitate conformation to the design rules, a design rule check (DRC) is carried out utilizing MEMSPro. This is absolutely necessary in order to produce a functional device that will actually be manufactured in the MUMPs technology. This is essential to ensure that the etching in the fabrication process using this technology maintains the desired geometry, eliminating the possibility of an over-etch or under-etch which may result from non-conforming. If there are serious violations the integrity of the dimensions will be compromised, resulting in a non-functional device. The entire ensemble is positioned on a single chip for batch fabrication and post processing.

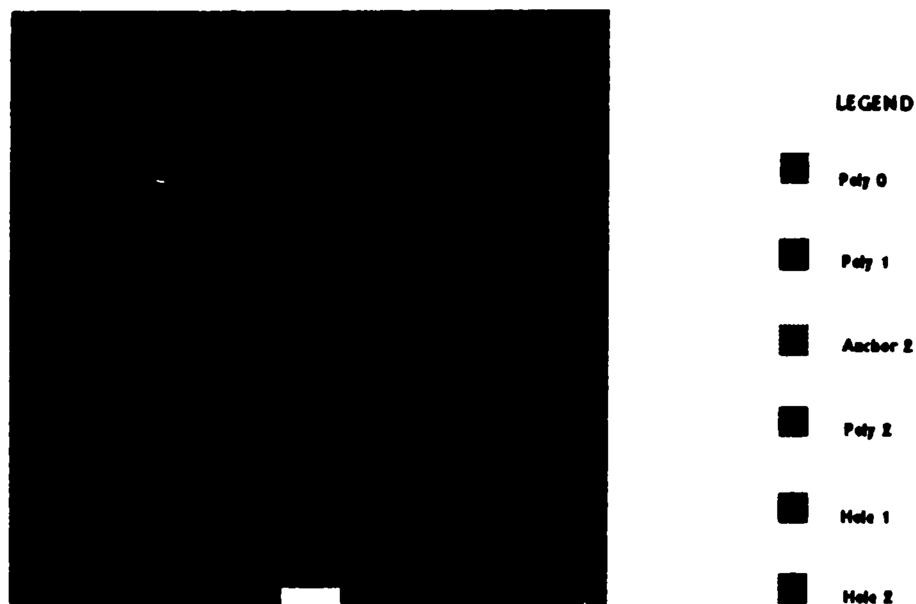

Fig. 2.9 Layout

2.3 POST PROCESSING

Once the dies with micromechanically fabricated devices in the MUMPs technology are ready, they have to undergo an appropriate and compatible post processing method to release the structural layers and obtain the desired MEMS device. The post processing can include special coating or some other operations for devices without free-standing structures, or alternatively micromachining for release of the free-standing structures.

Various methods for post processing have been investigated and reported for compatibility with different technologies and structural release objectives. Stiharu et al. (1999) introduced a post processing technique of deposition of humidity sensitive material on Mitel 1.5 μm chips and fabricated resistive as well as capacitive type humidity sensors.

However, an important aspect in the post processing of microsystems is the integrity of the contact pads after etching. Most wet etching processes described using substances such as NaOH, KOH, or TMAH attack the metal contact pads, which makes the electrical connections impossible. Hence, whether it is sacrificial or bulk micromachining, the use of wet etchants becomes limited. In general, as reported by Legtenberg et al (1993) and Mastrangelo et al (1993), the structures are subject to the problem of stiction when wet etchants are used in case of sacrificial etching. Hence, the use of wet etchants for sacrificial etching also requires additional anti-stiction drying methods. This becomes especially relevant in the release of capacitive plate structures where the gap between

plates is relatively small. Such is the present consideration in this thesis in which the analysis incorporates the range of influence of the Casimir force.

Besides, the post releasing mechanism for micromechanical structures could also adversely affect the overall performance of the microsystem. It would be desirable if the mechanical components only are released through a chemical etching process in such a way that microelectronics components, if integrated on the same chip, are protected without additional process or layers and also the stiction problem encountered in the case of wet sacrificial etching is avoided. Moreover, it would be advantageous if the same post-release process could be used for both sacrificial and bulk micromachining of MEMS devices.

Due to the above-mentioned limitations of the industrial CMOS process, the conventional liquid etchants such as EDP, KOH, TMAH and HNA or high-energy plasma etchants have restricted scope in post processing MEMS devices following an industrial CMOS process. In order to overcome all these constraints explained above and to fabricate useful MEMS devices, Muthukumaran et al (1999) proposed the gas phase xenon difluoride isotropic etching as a post-releasing process for microsystems fabricated using the Mitel 1.5 μm technology. This however is not compatible with the MUMPs process as xenon difluoride is selective to the silicon dioxide sacrificial layers and will not etch it.

Current methods used in the post processing of MEMS devices fabricated in MUMPs is based on a proprietary method developed by CRONOS laboratories. The method is generally described in the following steps:

Step 1: The fabricated structure is soaked in acetone for 30 minutes to remove the photoresist.

Step 2: In order to remove the acetone, the chip is further soaked in isopropanol for 5 minutes.

Step 3: The isopropanol is removed by rinsing in DI water for 10 minutes

Step 4: The sacrificial PSG layer is then etched by soaking the chip in a 49% hydrofluoric acid solution for exactly 3 ½ minutes at room temperature

Step 5: The HF is rinsed by soaking the chip in solution of methanol and water in a ratio of 4:1 for 9 minutes followed by pure methanol for 15 minutes.

Step 6: Liquid CO_2 is used in a super critical dry process to flush the methanol. It is then heated to 35°C, at which temperature the CO_2 will sublimate, thereby greatly reducing the tendency for stiction to occur.

In this chapter the most common method of fabrication of microelectromechanical systems (MEMS), photolithographic fabrication on a planar substrate is presented. This is the overwhelming choice for commercial and industrial processes. The current trends in post processing of MEMS structures with particular emphasis on the current method used for devices fabricated using MUMPs was also discussed.

The unit processes that make up this fabrication method include thermal oxidation, chemical vapor deposition (CVD), evaporation, sputtering and etching are described in the appendix. Combinations of these unit processes result in integrated processes such as surface micromachining, bulk micromachining, the dissolved wafer process and the standard CMOS process. An overview of another fabrication technology, the LIGA process, is also described in the appendix. The major advantage of producing three dimensional microstructures in LIGA was enunciated, achieved at a much greater comparative cost with fabrication on planar substrates.

As was mentioned at the beginning of this chapter, research and development into various fabrication technologies is ongoing and very active. Recent work by researchers at Massachusetts Institute of Technology in the United States have developed a new method of fabrication in which three-dimensional MEMS and electronic circuitry can be additively built on a substrate by ink-jet printing nanoparticle metal colloids (Fuller et al, 2002). As reported the method was used to fabricate such devices as linear and rotary electrostatic-drive motors, and in-plane and vertical electrothermal actuators. A major advantage of the method is the elimination of extreme processing conditions associated

with current methods, being able to form structures at plastic-compatible temperatures as low as 300°C. The potential for reduced cost and desktop fabrication of MEMS is an indication of future trends.

The thesis presents an analysis for curve veering of capacitive MEMS based on designs of microplates in the MUMPs technology, which is a surface micromachined integrated process. In order to do this, the following chapter presents the theory governing the operation of the microplate subject to electrostatic and Casimir forces. The analysis is carried out to obtain the natural frequencies for an investigation of the curve veering phenomenon occurrence in such plates. The influence of certain plate parameters is also studied in the subsequent chapter to determine their effect on plate stability, going on to establish the values for the occurrence of stiction resulting from a variation of the side dimensions and boundary conditions of devices designed and fabricated in this technology.

CHAPTER 3

ANALYSIS OF MICROPLATES INCLUDING ELECTROSTATIC AND CASIMIR FORCES

3.1 ELECTROSTATIC FORCE

Engineering components require accurate analysis, modeling and simulation in the design process to predict performance and functionality. The common techniques of microfabrication and the design process for a capacitive microelectromechanical system using the MUMPs technology were presented in the previous chapter. Based on this process and design for various conditions of geometry and boundary conditions, an analytical model will be developed in the present chapter. The necessity of an approximate solution will become evident due to the non-linearity of the formulation. The solution method presented here is based on a variational energy approach, the Rayleigh-Ritz method. Boundary characteristic orthogonal polynomials are derived and used as shape functions that approximate the deflection profile of the microplate. Subsequent minimization of the Rayleigh quotient result in a set of discrete simultaneous equations that represent an eigenvalue problem, the solution of which yield the natural frequencies of the system as eigenvalues.

The theory governing electrostatic actuation and capacitive sensing is based fundamentally on the established equations for electrostatics. However, certain considerations must be taken into account in the appropriate application of the theory (Bao, 2000). The following points are noted in the analysis:

- MEMS devices that incorporate capacitive sensing have electrostatic forces that are of the same order of magnitude as the elastic restoring forces. Coupling with other energy forms result in a mixed domain type problem that have to be solved simultaneously. One of such forms is the Casimir force, the effect of which is included in this thesis.

- The variation of electrostatic, elastic and Casimir forces with distance, give rise to non-linear problems that have to be accurately predicted to obtain the response of the system. Of particular interest would be the stability range in which devices perform efficiently and effectively.

- The decrease in dimensions for MEMS devices under electrostatic forces in the range in which the Casimir force is of significance, of the order of a few microns, give rise to fringing effects which are described but not included in the present analysis. The space charge layer effect is also not considered.

- Mechanical or electrical means are usually required to eliminate unwanted noise associated with the generated signal. In particular, the electrostatic forces which arise from the driving signal necessary for capacitive sensing is sometimes large enough to adversely distort the measured capacitance and must be reduced or eliminated.

Consider a capacitor made up of a pair of parallel electrodes as shown in Fig. 3.1 in which one end is fixed and the other free to move a distance x from the fixed end in the

normal direction. Assuming the dimensions of the electrodes are much larger than the distance between them, the fringe effects of the electric field may be neglected and the capacitance, C is given as

$$C = \frac{A\varepsilon\varepsilon_o}{x} \tag{3.1}$$

where A is the area of the electrode, ε is the relative permitivity of the medium between the electrodes, usually taken as unity for air, and ε_0 is the permitivity of a vacuum equal to 8.854×10^{-12} F/m where F stands for farads.

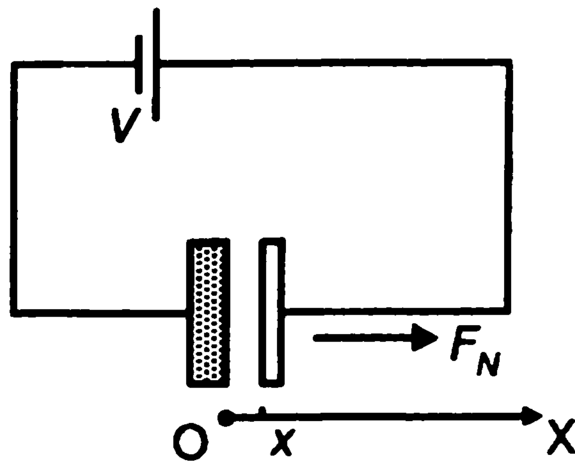

Fig. 3.1 The electrostatic normal force

The charge stored in the capacitor is given by:

$$Q_c = C(x)V \tag{3.2}$$

where V is the voltage applied across the electrodes from a battery source. The electric energy stored in the capacitor is given by

$$E_c = \frac{1}{2}C(x)V^2 \tag{3.3}$$

A force, F_n exists between the electrodes and causes the movable plate to be displaced by an infinitesimal distance δx. For conservation of energy of the system, the sum of the energy due to the plate displacement, stored capacitor energy and internal battery energy must be zero. This results in:

$$F_n \delta x + \frac{dE_c}{dx}\delta x + \frac{dE_b}{dx}\delta x = 0 \tag{3.4}$$

where E_b is the battery internal energy. This gives us:

$$F_n = -\frac{dE_c}{dx} - \frac{dE_b}{dx} \tag{3.5}$$

However, from Eq. 3.3 we obtain:

$$\frac{dE_c}{dx} = \frac{1}{2}\frac{\partial C(x)}{\partial x}V^2 \tag{3.6}$$

The internal energy of the battery, E_b is dependent on the charge flowing into and out of the battery, the voltage V remaining constant. This gives:

$$\frac{dE_b}{dx} = -V\frac{dQ_c}{dx} \tag{3.7}$$

Substituting Eq. 3.2 in Eq. 3.7 yields

$$\frac{dE_b}{dx} = -V^2\frac{\partial C(x)}{\partial x} \tag{3.8}$$

Substituting Eq. 3.6 and Eq. 3.8 in Eq. 3.5 results in

$$F_n = \frac{1}{2}\frac{\partial C(x)}{\partial x}V^2 \tag{3.9}$$

and using the relation from Eq. 3.1 we obtain the equation for electrostatic force on a pair of parallel plates separated by a gap x in an electric field given by:

$$F_n = -\frac{A\varepsilon\varepsilon_o}{2x^2}V^2 \tag{3.10}$$

The force is an attractive force as indicated by the negative sign in this result.

In the absence of a battery, the energy of the capacitor, E_c is obtained from Eqs. 3.2 and 3.3 as

$$E_c = \frac{Q_c^2}{2A\varepsilon\varepsilon_o}x \tag{3.11}$$

and the force applied on the free plate is

$$F_n = -\frac{Q_c^2}{2A\varepsilon\varepsilon_o} \tag{3.12}$$

In a similar manner the tangential force acting between the plates, F_t may be obtained. Consider Fig. 3.2 in which one plate is stationary and the other is free to move a distance y in a direction parallel to the plane containing the plates. A distance, z where z is much less than y, separates them. The capacitance between the two plates of constant width b is:

$$C = \frac{A_y\varepsilon\varepsilon_o}{x} \tag{3.13}$$

where $A_y = by$

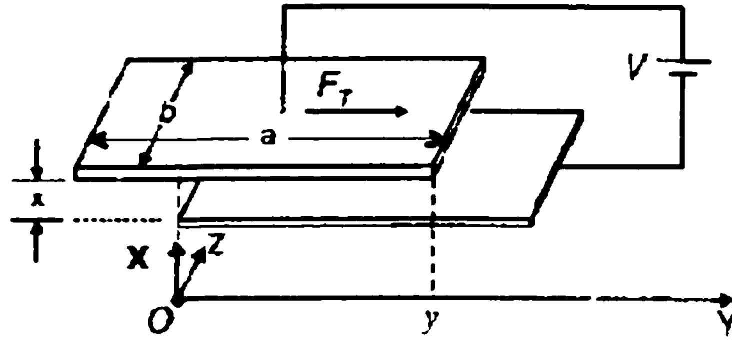

Fig. 3.2 Electrostatic tangential force

The charge stored in the capacitor is:

$$Q_c = C(y)V \tag{3.14}$$

and the energy stored in the capacitor is

$$E_c = \frac{by\varepsilon\varepsilon_o}{2x}V^2 \tag{3.15}$$

The principle of conservation of energy is applied to this system in which a force, F_t causes an infinitesimal displacement δy, electric energy E_c stored in the capacitor, and E_b is the energy stored in the battery. This gives:

$$F_t \delta y + \frac{dE_c}{dy} + \frac{dE_b}{dy} \delta y = 0 \tag{3.16}$$

Using Eq. 3.15 we obtain

$$\frac{dE_c}{dy} = \frac{b\varepsilon\varepsilon_o}{2x} V^2 \tag{3.17}$$

and

$$\frac{dE_b}{dy} = -\frac{d}{dy}(Q_c V) = -\frac{b\varepsilon\varepsilon_o}{2x} V^2 \tag{3.18}$$

Substituting Eqs. 3.17 and 3.18 in Eq. 3.16 yields the tangential force as

$$F_t = \frac{b\varepsilon\varepsilon_o}{2x} V^2 \tag{3.19}$$

The positive value of the tangential force implies that the movable plate is pulled together, increasing the overlap area of the two plates as shown in Fig. 3.2. It is interesting to note that the tangential force is independent of the overlap distance y.

Furthermore this force remains constant as the dimensions are scaled down with the gap between the plates, x consistent with the advantage of using electrostatic force in microelectromechanical devices.

The ratio of the normal force to the tangential force can be obtained from Eqs. 3.10 and 3.19 as

$$\frac{F_n}{F_t} = \frac{y}{x} \tag{3.20}$$

from which it is seen that the normal force is much larger than the tangential force, since y is usually much greater than x.

The foregoing has not taken into consideration the fringe effects induced by the electric charge, which arise and must be taken into account in the analysis of microplates subjected to electrostatic forces and is briefly mentioned shortly.

Fringing Effects

When the dimensions of the microplates are much larger than the distance between them a parallel-plate capacitor approximation to the capacitance will yield acceptable results as obtained from Eq. 3.1. However, in designs that have a dimension comparable to the gap between the plates, this approximation is no longer valid for sufficient accuracy and corrections to this are necessary due to the fact that the capacitance caused by the side edges and back sides (if applicable) significantly influence this quantity. This effect is referred to as *fringe effects*. It results in an increase of the estimated capacitance based on a parallel-plate capacitor model.

The capacitance of a pair of parallel plates taking into account fringing is not amenable to a closed form solution, hence numerical approximations are used to evaluate this quantity. Consider the parallel-plate capacitor shown in Fig. 3.2. A suitable approximation to the capacitance, $C(x)$, including fringe effects when $x<<b$, as is the case when consideration is given to the Casimir force is given by (Bao, 2000):

$$C(x) \approx \beta C_o(x) \tag{3.21}$$

in which $C_o(x)$ is the parallel-plate capacitance given by

$$C_o(z) = \frac{A\varepsilon\varepsilon_o}{x} = \frac{2ab\varepsilon\varepsilon_o}{x} \tag{3.22}$$

and β is the correction factor dependent on the dimensions of the structure given by (Bao, 2000)

$$\beta = 1 + \frac{x}{\pi a}\ln\frac{2\pi a}{x} + \frac{x}{\pi a}\ln\left(1 + \frac{2h}{x} + 2\sqrt{\frac{h}{x} + \frac{h^2}{x^2}}\right) \tag{3.23}$$

where h is the thickness of the microplate.

The electrostatic forces in the normal and tangential directions are given, respectively, as

$$F_n = -\frac{1}{2}\frac{\partial C(x)}{\partial x}V^2 \tag{3.24}$$

$$F_t = -\frac{\partial C(y)}{2\partial y}V^2 \tag{3.25}$$

3.2 CASIMIR FORCE

The Casimir force arises as a result of the interaction of a pair of neutral, parallel conducting planes, in which the vacuum of the electromagnetic field between them is disturbed. There is no force between the plates in classical electrodynamics, since the plates are assumed neutral. In the presence of the plates, the boundary conditions on the electromagnetic field are altered from the free field conditions resulting in an energy density in the space between the opposing parallel plates being less than that outside the plates (Serry et al, 1995). The attraction between the plates results from a quantum effect caused by the vacuum between them; the ground state of quantum electrodynamics (QED) causes the plates to attract each other. The boundary conditions imposed on the electromagnetic fields lead to a spatial redistribution of the mode density with respect to free space, creating a spatial gradient of the zero-point energy density and hence a net force between the plates (Chan et al, 2001).

Bordag et al (2001) derive the well known formula for the vacuum energy between two conducting parallel plates at zero temperature as

$$E = -\frac{\pi^2 \hbar c}{720 a^3} S \tag{3.26}$$

in which E is the vacuum energy, $\hbar$ is Planck's constant, c is the velocity of light, S is the surface area and a is the gap between the plates. In obtaining this result, it is assumed that S is much greater than a^2. The Casimir force, F is given by the derivative of the energy with respect to the gap, a as

$$F = -\frac{\pi^2 \hbar c}{240 a^4} S \tag{3.27}$$

From Bordag et al (2001) the Casimir energy for a rectangular cavity with perfectly conducting faces of sides a_1, a_2, a_3 and encompassing an electromagnetic vacuum is given by

$$E(a_1, a_2, a_3) = \hbar c \left[-\frac{\pi^2 a_2 a_3}{720 a_1^3} - \frac{\zeta_R(3)}{16\pi} \frac{a_3}{a_2^2} + \frac{\pi}{48}\left(\frac{1}{a_1} + \frac{1}{a_2}\right) + H\left(\frac{a_2}{a_1}, \frac{a_3}{a_1}, \frac{a_3}{a_2}\right)\right] \tag{3.28}$$

where function H is exponentially small in all its arguments if $a_1 \le a_2 \le a_3$ and can be found in Mamayev (1979) and for which $\zeta_R(3) \approx 1.202$

For a region in which $a_1 = a_2 \le a_3$ and considering the integral sums in H to be negligible, the following result is obtained:

$$E(a_1, a_3) = \frac{\hbar c}{a_1}\left[\frac{\pi}{24} - \left(\frac{\pi^2 a_2 a_3}{720 a_1^3} + \frac{\zeta_R(3)}{16\pi}\right)\frac{a_3}{a_1}\right] \tag{3.29}$$

Similarly for $a_1 = a_2 > a_3$, the vacuum energy becomes

$$E(a_1,a_3) \approx \frac{\hbar c}{a_1}\left[\frac{\pi}{48} - \frac{\zeta_R(3)}{16\pi} + \frac{\pi}{48}\frac{a_1}{a_3} - \frac{\pi^2}{720}\left(\frac{a_1}{a_3}\right)^3\right] \tag{3.30}$$

and for the case of a cube in which $a_1 = a_2 = a_3$,

$$E(a_1) \approx 0.0916\frac{\hbar c}{a_1} \tag{3.31}$$

The energy is positive in the range

$$0.408 < \frac{a_3}{a_1} < 3.48 \tag{3.32}$$

Outside this range the vacuum energy of the electromagnetic field inside the box is negative and is zero at the ends of the interval.

Subsequently the Casimir forces acting on opposite pairs of faces and directed normally towards them are Bordag (2001)

$$F_i(a_1,a_2,a_3) = -\frac{\partial E(a_1,a_2,a_3)}{\partial a_i} \tag{3.33}$$

and the total force is

$$\boldsymbol{F}(a_1,a_2,a_3) = -\nabla E(a_1,a_2,a_3) \tag{3.34}$$

where the operator ∇ is given by

$$\nabla = \frac{\partial}{\partial a_1} + \frac{\partial}{\partial a_2} + \frac{\partial}{\partial a_3}$$

It is interesting to note that the energy can be attractive or repulsive, depending on the relative dimensions of the sides of the rectangular cavity. The Casimir forces and energies for rectangular cavities of varying side lengths are numerically computed in Macklay (2000)

The repulsive Casimir forces on the interior of a sphere is obtained from the energy obtained as (Milton and Ng, 1998)

$$E = \frac{23}{1536\pi} \frac{(\varepsilon - 1)^2 \hbar c}{R} \tag{3.35}$$

in which ε is the permittivity of the interior of the sphere and R is its radius.

DeRaad and Milton (1981) investigated the Casimir effect for a cylinder obtaining the energy as

$$E = -\hbar c \frac{0.01356}{R^2} \tag{3.36}$$

The associated force with this energy is attractive.

The exact analytical calculation of Casimir energies and forces is only possible for configurations that are symmetrical. In experimental methods of interest that require the calculation of these quantities for non-symmetrical systems such as a sphere suspended over a disk, approximate methods of solutions are employed. The Casimir force for the specific configuration of a lens (sphere) over a disk, is approximately obtained as [160]

$$E = -\frac{\pi^3 \hbar c R}{360 a^3} \tag{3.37}$$

The accuracy of these results is contingent upon $a << R$.

All of the foregoing has been based on static considerations of the Casimir energies and forces. In the case where the gap, a is dependent on time, then the so-called Dynamical Casimir Effect arises giving rise to the force as (Bordag et al, 2001)

$$F(a(t)) = -\frac{\pi^2 \hbar c}{240 a(t)^4} S \tag{3.38}$$

The dynamics of a moving boundary results in a dependence of the Casimir force on the velocity and requires a correction to accurately account for this. However, the error that arises from this velocity dependence for an electromagnetic field is very small being less

than 8% of the static value (Bordag et al, 2001). Another effect of the moving boundaries is a quantum effect that manifests in the creation of photons from a vacuum.

The above results for the Casimir energies and forces are valid for ideal situations of perfect conductivity and zero temperature necessitating corrections that will arise in the use of real media. These corrections arise from the non-zero temperatures, finite conductivity, surface roughness characterized by imperfections in geometry or stochastically varying surface. Real media may require any one or a combination of these corrections. Serry et al (1995 and 1998) in their work on the Casimir effect in MEMS devices incorporate a constant factor applied to the Casimir force that ostensibly accounts for these imperfections. These factors are based on experimental validation of works by Arnold et al (1979) among others.

Macklay (2000) has given specific attention to the use of the Casimir Force in the design of Microelectromechanical Systems (MEMS). Chan et al (2001) have designed and fabricated non-linear micromechanical oscillators operated on the basis of the Casimir force using silicon microfabrication technology.

Due to the strong value of this force at distances of less than about 100 nm, stiction, a situation in which the device ceases to operate as a result of a collapse or sticking together, tends to occur compromising the integrity of the device. The Casimir force has a very dominant influence in this range.

3.3 ELASTIC FORCE

The free vibration behaviour of a rectangular plate is well documented in the literature (Leissa, 1973). From the classical theory, equation of motion for free vibration of the plate is given as (Timoshenko, 1990)

$$D\nabla^4 w + m\frac{\partial^2 w}{\partial t^2} = 0 \tag{3.39}$$

where,

w is the transverse deflection, t is the time,

∇^4 is the biharmonic operator given by

$\nabla^4 = \nabla^2\nabla^2$ $\quad\quad$ $\nabla^2 = \frac{\partial^2}{\partial x^2} + \frac{\partial^2}{\partial y^2}$ in rectangular Cartesian coordinates

m is the mass per unit area of plate

D is the flexural rigidity of the plate given by

$D = \frac{Eh^3}{12(1-\nu^2)}$ in which E is is Young's Modulus, h is plate thickness, and ν is Poisson's ratio.

Eq. 3.39 is based on certain assumptions that exclude complicating effects such as orthotropy, in-plane forces, variable thickness, the effects of surrounding media, large deflections, shear deformation and rotary inertia, and non-homogeneity. Hence Eq. 3.39

can be solved in a closed form when at least two opposite edges of the plate are simply supported.

Under the action of electrostatic field effects, the plate vibratory motion is subjected to attractive forces. The elastic restoring forces resist the resulting deformation.

This electrostatic force for a capacitive pair of plates subject to an elastic restraining force can be obtained from Eq. 3.10 as

$$F_{elec} = \frac{A\varepsilon\varepsilon_o}{2(d-w)^2}V^2 \tag{3.40}$$

where ε is the permittivity of air, V is the applied voltage, d is the gap and $w = w(x,y,t)$ is the time and space dependent lateral deflection of the plate.

As the plate dimensions are decreased correspondingly with the gap, the Casimir effect should be taken into account. This is given by (Maclay, 1999)

$$F_{Casimir} = \frac{A\pi^2\hbar c}{240(d-w)^4} \tag{3.41}$$

where h is Planck's constant and c is the speed of light.

Considering these effects, the equation of motion for the micro plate subjected to these forcing terms is given as

$$D\nabla^4 w + m\frac{\partial^2 w}{\partial t^2} - \frac{\varepsilon V^2}{2(d-w)^2} - \frac{\pi^2 \hbar c}{240(d-w)^4} = 0 \qquad (3.42)$$

Evidently, consideration of the field forces has resulted in a non-linear time dependent partial differential equation in two space variables. This non-linear system can be solved approximately by numerical methods such as the finite element method.

An alternate approach is employed in this thesis to solve this non-linear system in order to obtain an approximate solution for the response. The approximate method used is the Rayleigh-Ritz method in which the assumed deflection functions are boundary characteristic orthogonal polynomials.

3.4 BOUNDARY CHARACTERISTIC ORTHOGONAL POLYNOMIALS

As has been previously stated, the microplate is modeled as a thin uniform rectangular plate such that various boundary conditions could be defined. The uniform electric field and Casimir attraction between the flexible plate and the rigid back plate introduce forces, $\varepsilon V^2/2(d-w)^2$ and $\pi^2 hc/240(d-w)^4$ that opposes the restoring elastic force of the plate, where ε is the permittivity of the air, V is the applied voltage, d is the capacitive gap and $w = w(x,y)$ is the deflection function.

The deflection of a rectangular plate undergoing free flexural vibration can be expressed in terms of boundary characteristic orthogonal polynomials, based on the separation of variables in the x and y directions as

$$W(x,y) = \sum\sum A_{mn}\phi_m(x)\varphi_n(y) \tag{3.43}$$

where $x=\xi/a$ and $y=\eta/b$ and ξ and η are coordinates along the two sides of the microplate, and a and b are plate dimensions.

The first member of the orthogonal set ϕ_l is constructed to satisfy all the boundary conditions of the beam problems accompanying the plate problem. For a clamped plate, C-C-C-C shown in Fig. 3.3, this is obtained as follows:

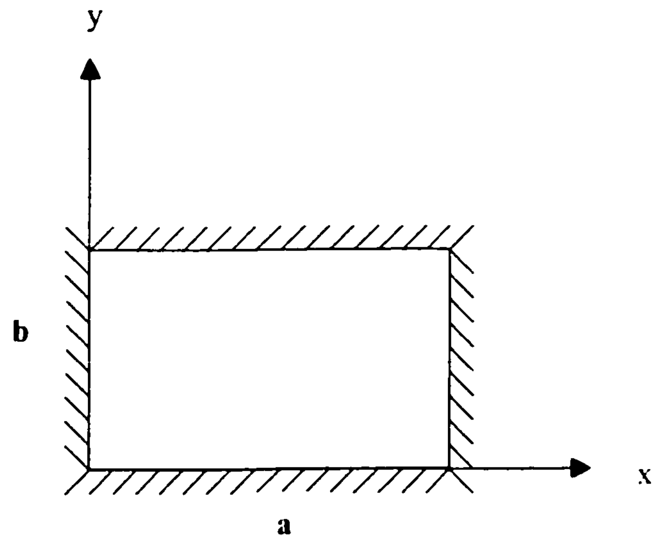

Fig 3.3 Sketch of C-C-C-C plate

The accompanying beam problem has identical boundaries in the two orthogonal directions of x and y respectively as (Bhat 1985)

$$X(0) = X'(0) = X(1) = X'(1) = 0 \qquad (3.44a)$$

$$Y(0) = Y'(0) = Y(1) = Y'(1) = 0 \qquad (3.44b)$$

In order to generate the first member of the orthogonal set we commence by assuming the beam deflection function in the x direction as

$$X(x) = a_0 + a_1 x + a_2 x^2 + a_3 x^3 + a_4 x^4 \tag{3.45}$$

It is necessary for the function to satisfy the geometric and natural boundary conditions. Applying the boundary conditions in Eq. 3.44 to Eq. 3.45 results in the deflection shape given by

$$X(x) = a_4 (x^2 - 2x^3 + x^4) \tag{3.46}$$

where a_4 is an arbitrary constant. The deflection function is obtained as

$$\phi_1(x) = x^2 - 2x^3 + x^4 \tag{3.47}$$

Generation of the higher members of the orthogonal polynomial set involves satisfaction of the geometric boundary conditions only. In line with the Gram-Schmidt process, this is obtained as (Burden and Faires, 1993)

$$\phi_2(x) = (x - B_2)\phi_1(x) \tag{3.48}$$

$$\phi_i(x) = (x - B_i)\phi_{i-1}(x) - C_i \phi_{i-2}(x) \tag{3.49}$$

where

$$B_i = \frac{\int_a^b x w(x)\phi_{i-1}^2(x)dx}{\int_a^b w(x)\phi_{i-1}^2(x)dx} \quad (3.50)$$

and

$$C_i = \frac{\int_a^b x w(x)\phi_{i-1}(x)\phi_{i-2}(x)dx}{\int_a^b w(x)\phi_{i-2}^2(x)dx} \quad (3.51)$$

In Eqs. 3.50 and 3.5, *w(x)* is a weighting function which is taken as unity. The interval is taken from 0 to 1 and the polynomials are chosen in such a way as to make the polynomials orthonormal. They are referred to as *Boundary Characteristic Orthogonal Polynomials*. These polynomials are used as approximations for the deflection shape to obtain the natural frequencies in an energy method of solution. As the number of polynomials used in the solution is increased, the accuracy of the results is enhanced.

The first member of the set of orthogonal polynomials for other boundary conditions is similarly obtained. Consider the case of 2 adjacent sides clamped and the other 2 free represented by C-C-F-F and shown in Fig. 3.4

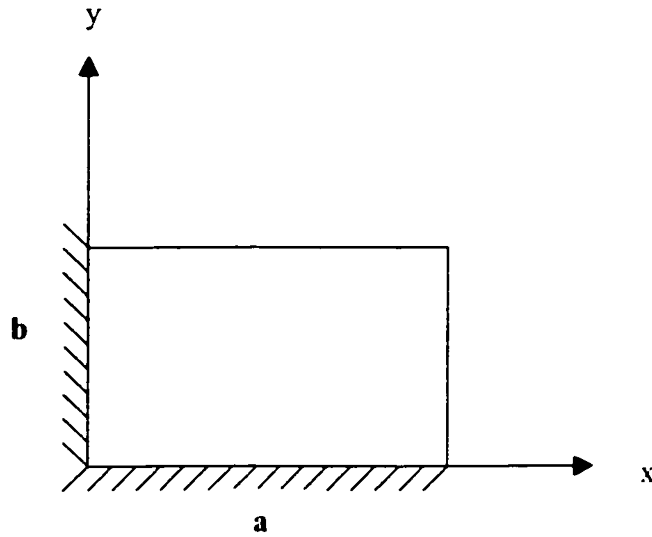

Fig. 3.4 Sketch of C-C-F-F plate

Both of the accompanying beam problems have the same boundary conditions, namely

$$X(0) = X'(0) = X''(1) = X'''(1) = 0 \tag{3.52a}$$

$$Y(0) = Y'(0) = Y''(1) = Y'''(1) = 0 \tag{3.52b}$$

Assuming the deflection function to be of the form given in Eq. 3.45 as

$$X(x) = a_0 + a_1 x + a_2 x^2 + a_3 x^3 + a_4 x^4$$

and applying the boundary conditions (Eq. 3.52) the first member of the set of orthogonal polynomials for a C-C-F-F plate is

$$\phi_1(x) = 6x^2 - 4x^3 + x^4 \tag{3.53a}$$

$$\varphi_1(y) = 6y^2 - 4y^3 + y^4 \tag{3.53b}$$

Furthermore, the Gram-Schmidt process is used to generate higher order polynomials.

For a plate with 3 sides clamped and 1 free (C-F-C-C), as shown in Fig. 3.5, the boundary conditions are different in each of the beam directions and are given by

$$X(0) = X'(0) = X''(1) = X'''(1) = 0 \tag{3.54a}$$

$$Y(0) = Y'(0) = Y(1) = Y'(1) = 0 \tag{3.54b}$$

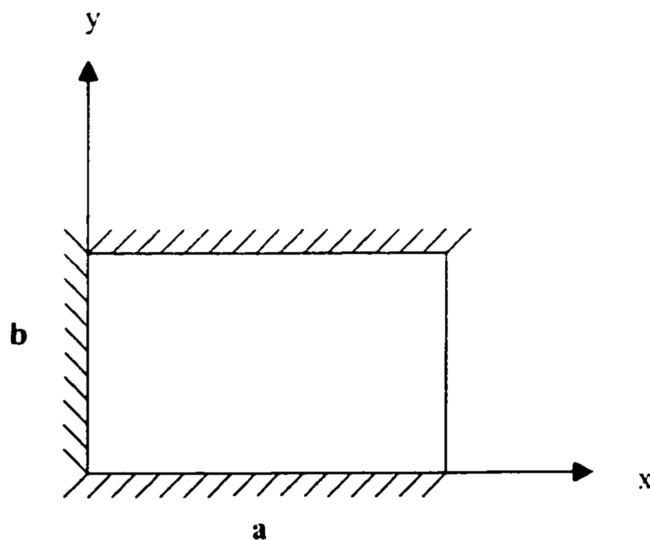

Fig. 3.5 Sketch of C-F-C-C plate

Assuming a deflection function given by Eq. 3.45 for both directions and applying the boundary conditions in Eqs. 3.54, the first set of orthogonal polynomials for this is

$$\phi_1(x) = 6x^2 - 4x^3 + x^4 \tag{3.55a}$$

$$\varphi_1(y) = y^2 - 2y^3 + y^4 \tag{3.55b}$$

For a plate clamped on 2 opposite sides and free on the other 2 opposite sides (C-F-C-F), shown in Fig. 3.6, the boundary conditions are different in each beam direction and are given by

$$X''(0) = X'''(0) = X''(1) = X'''(1) = 0 \tag{3.56a}$$

$$Y(0) = Y'(0) = Y(1) = Y'(1) = 0 \tag{3.56b}$$

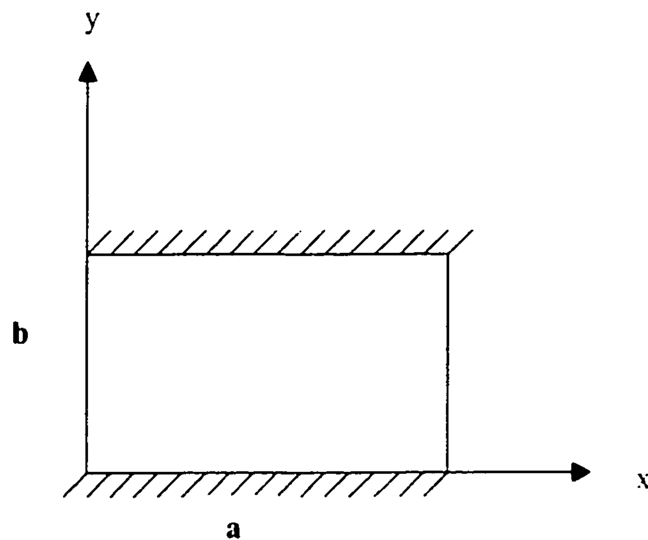

Fig. 3.6 Sketch of C-F-C-F plate

In this case the assumed deflection functions are of the form

$$X(x) = a_0 + a_1 x + a_2 x^2 + a_3 x^3 + a_4 x^4 + a_5 x^5 + a_6 x^6 \tag{3.57a}$$

$$Y(y) = a_0 + a_1 y + a_2 y^2 + a_3 y^3 + a_4 y^4 \tag{3.57b}$$

Applying the boundary conditions in Eqs. 3.56 to Eqs. 3.57 we obtain the first set of the orthogonal polynomials in each beam direction as

$$\phi_1(x) = C_1 + C_2 x + \frac{5}{2} x^4 - 3x^5 + x^6 \tag{3.58a}$$

$$\varphi_1(y) = y^2 - 2y^3 + y^4 \tag{3.58b}$$

From Eq. 3.58a it is seen that the function $X(x)$ satisfies the boundary conditions for any combination of C_1 and C_2 and the natural frequencies obtained would vary with each set of values of C. Hence these constants are chosen in such a way that the natural frequencies are minimized. This can be achieved by setting C_1 to zero. The natural frequency decreases monotonically with increasing C_2 (Bhat, 1985) and hence any arbitrarily large number would suffice. After numerical computations, a suitable value of C_2 chosen that does not change the natural frequency to 7 decimal places is 1,200,000.

Next, a cantilever plate (F-F-F-C) is considered and shown in Fig. 3.7. Once again the boundary conditions are different in each beam direction and are given by

$$X(0) = X'(0) = X''(1) = X'''(1) = 0 \quad (3.59a)$$

$$Y''(0) = Y'''(0) = Y''(1) = Y'''(1) = 0 \quad (3.59b)$$

The assumed deflection function in the x direction is the same as in Eq. 3.45 and that for the y direction is from Eq. 3.57a. Applying these functions and boundary conditions the first set of orthogonal polynomials for a cantilever plate are obtained as

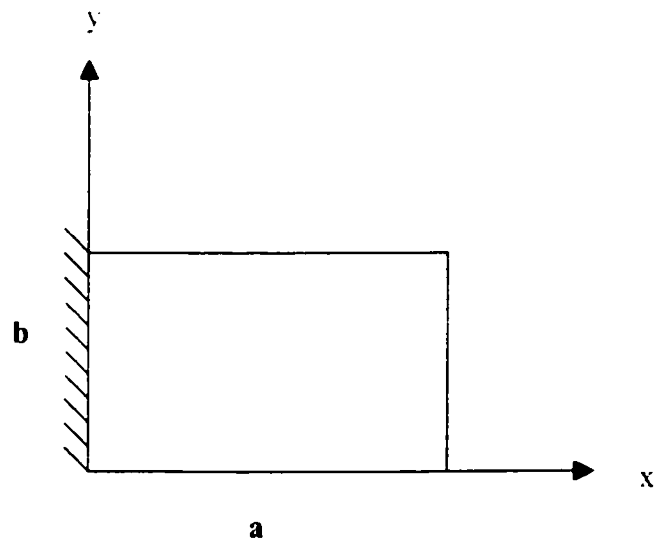

Fig. 3.7 Sketch of F-F-F-C (Cantilever) plate

$$\phi_1(x) = 6x^2 - 4x^3 + x^4 \quad (3.60a)$$

$$\varphi_1(y) = C_1 + C_2 y + \frac{5}{2} y^4 - 3y^5 + y^6 \quad (3.60b)$$

in which C_1 and C_2 are chosen as earlier stated.

The orthogonal polynomials obtained in this section for the various boundary conditions are used in the Rayleigh-Ritz method of analysis to obtain the natural frequencies of vibration for the microplate in order to study the curve veering behaviour and identify the combinations of side ratios at which it occurs for a given set of boundary conditions. The analysis will go on to demonstrate the influence of the electrostatic and Casimir forces on these natural frequencies. The influence of variations in voltage, side dimensions and boundary conditions on the stability of such capacitive microelectromechanical systems is also investigated.

3.5 THE RAYLEIGH-RITZ METHOD

Eq. 3.42 is a differential formulation of the microplate model subject to electrostatic and Casimir forces and is based on equilibrium principles or Newtonian mechanics. However in system models in which the shapes are irregular, materials are anisotropic, or loads are non-uniform as considered in the present thesis, Newtonian formulations require demanding and complicated analysis that may be cumbersome for a study of this nature. An alternative approach is to use energy methods based on Lagrangian mechanics to establish the system model for microplates. The basis of this method is the Lagrange equation of motion given by:

$$\frac{\partial}{\partial t}\left(\frac{\partial L}{\partial \dot{q}_i}\right)-\frac{\partial L}{\partial q_i}=Q_i \tag{3.61}$$

where

$$L = T - U$$

and T = Kinetic energy

U = Strain energy

Q_i = Generalized forces due to unbalance

q_i = generalized coordinates

As mentioned in Rajalingham and Bhat (1998), the determination of a large number of natural frequencies for the vibration of the microplate is more appropriately carried out using an energy method such as the Rayleigh-Ritz and is adopted in the present analysis.

Furthermore it has been stated earlier in Eq. 3.43 that the deflection of a rectangular plate undergoing free flexural vibration can be expressed in terms of boundary characteristic orthogonal polynomials in the x and y directions as

$$W(x,y) = \sum\sum A_{mn}\phi_m(x)\varphi_n(y)$$

where x and y are dimensionless coordinates given by

$$x = \frac{\xi}{a} \qquad y = \frac{\eta}{b}$$

ξ, η are Cartesian coordinates for the ordinate and abscissa respectively.

The application of the principle of conservation of energy results in the condition

$$U_{max} = T_{max} \tag{3.62}$$

The natural frequency may be written as

$$\omega^2 = \frac{U_{max}}{T^*_{max}} \tag{3.63}$$

where

$$T_{max} = \omega^2 T^*_{max} \tag{3.64}$$

The condition

$$\frac{\partial \omega^2}{\partial A_{mn}} = 0 \tag{3.65}$$

leads to

$$\frac{\partial U_{max}}{\partial A_{mn}} - \omega^2 \frac{\partial T_{max}}{\partial A_{mn}} = 0 \tag{3.66}$$

where T_{max} is the maximum kinetic energy of the system given by (Timoshenko, 1990)

$$T_{max} = \frac{1}{2}\rho hab\omega^2 \int_0^1\int_0^1 W^2(x,y)dxdy \tag{3.67}$$

The maximum strain energy due to the elastic forces acting on the microplate is also given by

$$U_{elastic} = \frac{Dab}{2a^4}\int_0^1\int_0^1 [W_{xx}^2 + \alpha^4 W^2{}_{yy} + 2\nu\alpha^2 W_{xx}W_{yy} + 2(1-\nu)\alpha^2 W_{xy}^2]dxdy \tag{3.68}$$

where ρ is the density of the plate material, h is the thickness of the plate, D is the flexural rigidity of the plate, α is the side ratio a/b, ν is Poisson's ratio, and the subscripts x and y refer to differentiation with respect to the subscript and the number of times the subscript appears denotes the order of differentiation.

The maximum potential due to the action of the electrostatic force on the plate is

$$U_{elec} = -\frac{\varepsilon\varepsilon_o V^2}{2}\int_0^b\int_0^a\int_0^w \frac{dwd\xi d\eta}{[d - w(\xi,\eta)]^2} \tag{3.69}$$

and that due to the Casimir force is

$$U_{casimir} = -\frac{\pi^2 \hbar c}{240} \int_0^b \int_0^a \int_0^w \frac{dw\, d\xi\, d\eta}{[d - w(\xi, \eta)]^4} \tag{3.70}$$

From a Taylor series expansion of the integrand (which represents the respective electrostatic and Casimir forces) and assuming small values of w/d, a first order approximation to Eq. 3.69 for the maximum electric potential is

$$U'_{elec} = -\frac{\varepsilon V^2 ab}{2} \int_0^1 \int_0^1 \left(\frac{w^2}{d^3} + \frac{w}{2d^2} \right) dx\, dy \tag{3.71}$$

Similarly for the maximum potential due to the Casimir effect can be expressed as

$$U'_{casimir} = -\frac{\pi^2 \hbar c}{2} \int_0^1 \int_0^1 \left(\frac{w^2}{60 d^5} + \frac{w}{240 d^2} \right) dx\, dy \tag{3.72}$$

The maximum potential energy is then

$$U_{max} = U'_{elastic} + U'_{elec} + U'_{casimir} \tag{3.73}$$

The deflection function in Eq. 3.43 may be rewritten as

$$W(x,y) = \sum\sum A_{mn} w_{mn}(x,y) \tag{3.74}$$

Furthermore,

$$W^2(x,y) = \sum_{m=1}^{M}\sum_{n=1}^{N}\sum_{r=1}^{R}\sum_{s=1}^{S} A_{mn} A_{rs} w_{mn}(x,y) w_{rs}(x,y) \tag{3.75}$$

from which

$$\frac{\partial}{\partial A_{mn}} W^2(x,y) = 2W(x,y)\frac{\partial W(x,y)}{\partial A_{mn}} = 2\sum_{r=1}^{R}\sum_{s=1}^{S} A_{rs} w_{rs}(x,y) w_{mn}(x,y) \tag{3.76a}$$

The following relations are similarly obtained

$$\frac{\partial}{\partial A_{mn}} W_{xx}^2 = 2W_{xx}^{rs}\frac{\partial W_{xx}^{mn}}{\partial A_{mn}} = 2\sum_{r=1}^{R}\sum_{s=1}^{S} A_{rs} W_{xx}^{rs} W_{xx}^{mn} \tag{3.76b}$$

$$\frac{\partial}{\partial A_{mn}} W_{yy}^2 = 2W_{yy}^{rs}\frac{\partial W_{yy}^{mn}}{\partial A_{mn}} = 2\sum_{r=1}^{R}\sum_{s=1}^{S} A_{rs} W_{yy}^{rs} W_{yy}^{mn} \tag{3.76c}$$

$$\frac{\partial}{\partial A_{mn}} W_{xx} W_{yy} = W_{xx} \frac{\partial W_{yy}}{\partial A_{mn}} + W_{yy} \frac{\partial W_{xx}}{\partial A_{mn}} = W_{xx}^{rs} \frac{\partial W_{yy}^{mn}}{\partial A_{mn}} + W_{yy}^{rs} \frac{\partial W_{xx}^{mn}}{\partial A_{mn}}$$

$$= \sum_{r=1}^{R} \sum_{s=1}^{S} A_{rs} W_{xx}^{rs} W_{yy}^{mn} + \sum_{r=1}^{R} \sum_{s=1}^{S} A_{rs} W_{yy}^{rs} W_{xx}^{mn} \tag{3.76d}$$

$$\frac{\partial}{\partial A_{mn}} W_{xy}^{2} = 2 W_{xy}^{rs} \frac{\partial W_{xy}^{mn}}{\partial A_{mn}} = 2 \sum_{r=1}^{R} \sum_{s=1}^{S} A_{rs} W_{xy}^{rs} W_{xy}^{mn} \tag{3.76e}$$

Substitution of the deflection function (Eq. 3.43) into the kinetic and strain energy expressions and minimizing the Rayleigh quotient with respect to the coefficients A_{ij} yields the desired eigenvalue equation

$$\sum_{m} \sum_{n} [B_{mnij} + \beta C_{mnij} + \gamma D_{mnij} - \lambda E_{mi}^{(0,0)} F_{nj}^{(0,0)}] A_{mn} = 0 \tag{3.77}$$

where

$$B_{mnij} = E_{mi}^{(2,2)} F_{nj}^{(0,0)} + \alpha^{4} E_{mi}^{(0,0)} F_{nj}^{(2,2)} + \nu \alpha^{2} [E_{mi}^{(0,2)} F_{nj}^{(2,0)} + E_{mi}^{(2,0)} F_{nj}^{(0,2)}] + 2(1-\nu) \alpha^{2} E_{mi}^{(1,1)} F_{nj}^{(1,1)} \tag{3.78a}$$

$$C_{mnij} = E_{mi}^{(0,0)} F_{nj}^{(0,0)} \qquad D_{mnij} = E_{mi}^{(0,0)} F_{nj}^{(0,0)} \tag{3.78b}$$

$$E_{mi}^{(r,s)} = \int_0^1 \left(d^r\phi_m/dx^r\right)\left(d^s\phi_i/dx^s\right)dx$$

$$F_{nj}^{(r,s)} = \int_0^1 \left(d^r\varphi_n/dy^r\right)\left(d^s\varphi_j/dy^s\right)dy \tag{3.78c}$$

$$\alpha = a/b \qquad m,n,i,j = 1,2,3,\ldots, \qquad r,s = 0,1,2$$

$$\beta = \frac{\varepsilon V^2 a^4}{Dd^3} \qquad \gamma = \frac{\pi^2 \hbar c a^3}{60Dd^5} \qquad \lambda = \frac{\rho h \varpi^2 a^4}{D} \tag{3.78d}$$

Solution of the eigenvalue equation will yield the natural frequencies and the mode shapes of the plate necessary for an investigation of the curve veering behaviour of the system and a parametric study of the influence of certain variables on the natural frequencies for the various boundary conditions considered in here.

CHAPTER 4

RESULTS AND DISCUSSIONS

4.1 NATURAL FREQUENCIES

The capacitive microelectromechanical system used for analysis is modeled as a microplate with various boundary conditions. The presence of an electrostatic force and the Casimir force acting on the plate introduces deflection dependent load intensities in the plate vibration problem. An approximate method of analysis is used to obtain solutions to this non-linear system represented in differential form by Eq. 3.42. The natural frequencies of the system are obtained using an energy approach, the Rayleigh-Ritz method of analysis. In this solution method, the shape functions used in approximating the microplate deflection are boundary characteristic orthogonal polynomials as derived in section 3.4. The resulting eigenvalue problem (Eq. 3.77) is solved numerically using *MATLAB*. Computer programs are written to obtain the natural frequencies using various boundary characteristic orthogonal polynomials to represent the deflection profiles of plates with different boundary conditions. The various boundary conditions considered are for rectangular microplates clamped on all four sides and denoted by C-C-C-C, clamped on three sides and free on one (C-F-C-C), clamped on two opposite sides and free on the other two (C-F-C-F), clamped on two adjacent sides and free on the other two sides (C-C-F-F), and a cantilever plate (F-F-F-C). These five boundary conditions represent typical situations that arise in the design of capacitive MEMS.

The parameters of the microplate used for determination of the natural frequencies include the side ratio, which is varied for values of a/b ranging from 0.1 to 3.0. Although for symmetric plates a range of 0.1 to 1.0 may have been used, for plates with asymmetrical boundary conditions it is necessary to use a/b ratios from 0.1 to 1 and above. The side ratio a/b used in these computations are based on a fixed value of the width, b equal to 300 μm (see Figs 3.3 to 3.8). The variable thickness and gap between parallel plates range from 0.1 μm to 2 μm. Other parameters used are density ρ, 2330 kg/m^3, permittivity of air ε, 8.87 x 10^{-12} F/m, Young's Modulus E, 1.6 x 10^{11} N/m^2, Planck's constant 6.6260755 x 10^{-34} and the speed of light c, 299792458 m/s.

Table 4.1 shows a comparison of the non-dimensional natural frequencies of vibration for a rectangular plate clamped on all four sides with values obtained in the literature. The results shown from this analysis were obtained using 6 orthogonal polynomials in each direction. This was sufficient to achieve accuracy comparable to values reported by Leissa (1973), Dickson and Li (1982) and Bhat (1985), for the first 9 modes of vibration. However, when the plates are subjected to a load intensity arising from the electrostatic force, the natural frequencies are reduced, implying an increase in the stiffness of the plates as previously reported by Stiharu and Bhat (1997), Rajalingham and Bhat (1998), Chan et al (1999), and Nemirovsky and Bochobza-Degani (2001). These works present results for the fundamental mode of vibration in plates that are clamped on all boundaries. In this work the influence of various boundary conditions that arise in the design and microfabrication of capacitive MEMS using the MUMPs technology on the natural frequencies of the microplate as it is subjected to various field intensities and the

Casimir effect is obtained. This is illustrated in Tables 4.2 to 4.6, which compare the first 9 modes of natural frequencies for various loading intensities and boundary conditions using 3 orthogonal polynomials in each direction. Specifically when a voltage of 110 volts is applied to the pair of parallel microplates clamped on all 4 sides (C-C-C-C) as shown in Table 4.2, and with a thickness of 2 μm and a gap of 2 μm, a reduction of the non-dimensional fundamental natural frequency from 35.9855 to 16.6561 is obtained, amounting to about 50 % reduction. Non-dimensional parameters are used in the presentation of the results generalization. In this work reductions are noted for natural frequencies of higher vibration modes but not by as much a percentage as can be seen from these tables. It is also seen in Table 4.2 that the 2-1 and 1-2 mode have *apparently* identical natural frequencies and are reduced from 74.18434 to 66.97362 for an increase in voltage from 0 to 110 volts, respectively. This apparent coincidence of symmetric modes of vibration shall be discussed in detail shortly. Tables 4.7 and 4.8 show the variation of natural frequency with gap in the absence of any applied voltage for the first 9 modes of vibration of a square plate in which a/b equals 1. In Table 4.7, which gives values for a C-C-C-C microplate, it is seen that as the gap decreases from 2 μm to 0.1 μm, there is a decrease in the non-dimensional fundamental natural frequency from 35.98997 to 32.36309; a decrease of about 10%. The Casimir effect which is significant at submicron orders of feature size accounts for this reduction. This is more apparent and critical in Table 4.8, which gives these values for a cantilever microplate. In this table it is observed that there is a substantial reduction in the fundamental non-dimensional natural frequency from 5.88392 at 2 μm to zero at 0.1 μm. This implies that at 0.1 μm the cantilever plate will experience instability as a result of stiction. Serry et al (1998)

have previously investigated the role of the Casimir effect in the static deflection and stiction of membrane strips in MEMS. They have shown that for some systems having the Casimir force as the only operative external force and a system dimensional constant $K_C > 0.245$, a collapsed strip is inevitable. More work is required to obtain similar parameters for two-dimensional vibrating structures as considered here. However, dynamical studies carried out by Chan et al (2001) show how the Casimir effect introduces non-linearities in an anharmonic oscillator. Table 4.9 presents a comparison of the natural frequencies of the microplates having various boundary conditions and subject to an electrostatic loading of 20 volts. From this table it is seen that the C-C-C-C plate has a greater elastic restoring force than all the others.

The implications for designers of capacitive MEMS devices with gaps of microplates in the sub-micron range is that it may be necessary to incorporate the Casimir effect in the analysis, design and simulations for accurate characterization of devices in this range of feature size.

Boundary Conditions: C-C-C-C
Plate thickness : 2 microns
Applied Voltage : 0 volt
Side dimensions : 300 x 300 microns
6 orthogonal polynomials used in each direction

Vibration Mode	Beam Functions	S.S. Plate Functions	Orthogonal Polynomials
1-1	35.992000	35.988000	35.985513
1-2	73.413000	73.406000	73.394711
2-1	73.413000	73.406000	73.394711
2-2	108.270000	108.250000	108.217926
1-3	131.640000	131.620000	131.778859
3-1	132.240000	132.230000	132.409722

Table 4.1 - Comparison of non-dimensional natural frequencies

Boundary Conditions: C-C-C-C
Plate thickness : 2 microns
Gap : 2 microns
Side dimensions : 300 x 300 microns
3 orthogonal polynomials used in each direction

Vibration Mode	Applied voltage, V (volts) 0	20	40	60	70	80	90	100	110
1-1	35.98997	35.51943	34.06884	31.50311	29.71683	27.51200	24.77713	21.30912	16.65613
1-2	74.18434	73.95721	73.27158	72.11439	71.35215	70.46239	69.44023	68.27970	66.97362
2-1	74.18434	73.95721	73.27158	72.11439	71.35215	70.46239	69.44023	68.27970	66.97362
2-2	108.59098	108.43594	107.96948	107.18754	106.67620	106.08314	105.40697	104.64607	103.79860
1-3	137.29385	137.17125	136.80281	136.18652	135.78443	135.31900	134.78957	134.19538	133.53557
3-1	138.07004	137.94814	137.58177	136.96899	136.56921	136.10646	135.58011	134.98940	134.33349
2-3	168.81909	168.71940	168.41999	167.91978	167.59384	167.21697	166.78883	166.30900	165.77706
3-2	168.81909	168.71940	168.41999	167.91978	167.59384	167.21697	166.78883	166.30900	165.77706
3-3	224.17874	224.10368	223.87835	223.50229	223.25752	222.97475	222.65384	222.29464	221.89695

Table 4.2 Non-dimensional natural frequencies influenced by various applied voltages for C-C-C-C microplate

Boundary Conditions: C-F-C-C
Plate thickness : 2 microns
Gap : 2 microns
Side dimensions : 300 x 300 microns
3 orthogonal polynomials used in each direction

Vibration Mode	Applied voltage, V (volts) 0	20	40	60	70	80
1-1	24.43234	23.73376	21.50227	17.14957	13.59234	7.65323
1-2	41.39488	40.98644	39.73593	37.55935	36.07421	34.28074
2-1	65.09102	64.83203	64.04880	62.72168	61.84378	60.81507
2-2	83.03570	82.83284	82.22126	81.19172	80.51546	79.72804
1-3	110.11367	109.96078	109.50082	108.72989	108.22585	107.64132
3-1	129.75902	129.62930	129.23936	128.58683	128.16090	127.66768
2-3	147.36100	147.24679	146.90362	146.32988	145.95574	145.52284
3-2	157.61720	157.51043	157.18966	156.65360	156.30417	155.90002
3-3	227.20440	227.13034	226.90801	226.53699	226.29549	226.01653

Table 4.3 Non-dimensional natural frequencies influenced by various applied voltages for C-F-C-C microplate

Boundary Conditions: C-F-C-F
Plate thickness : 2 microns
Gap : 2 microns
Side dimensions : 300 x 300 microns
3 orthogonal polynomials used in each direction

Vibration Mode	**Applied voltage, V (volts)**					
	0	**20**	**40**	**60**	**70**	**80**
1-1	23.75898	23.03999	20.73396	16.17582	12.34104	5.11091
1-2	38.21158	37.76873	36.40787	34.01901	32.37186	30.36046
2-1	64.66470	64.40400	63.61550	62.27914	61.39492	60.35856
2-2	80.71194	80.50322	79.87381	78.81361	78.11677	77.30491
1-3	88.13157	87.94047	87.36465	86.39643	85.76122	85.02239
3-1	129.44098	129.31094	128.92003	128.26587	127.83888	127.34441
2-3	134.18965	134.06422	133.68721	133.05649	132.64492	132.16843
3-2	145.62835	145.51278	145.16551	144.58487	144.20620	143.76804
3-3	202.24627	202.16307	201.91326	201.49621	201.22467	200.91089

Table 4.4 Non-dimensional natural frequencies influenced by various applied voltages for C-F-C-F microplate

Boundary Conditions: C-C-F-F
Plate thickness : 2 microns
Gap : 2 microns
Side dimensions : 300 x 300 microns
3 orthogonal polynomials used in each direction

Vibration Mode	Applied voltage, V (volts) 0	10	15	20	25	30
1-1	7.44337	6.85505	6.03960	4.66431	1.68190	0.00000
1-2	26.13344	25.97200	25.76877	25.48153	25.10740	24.[illegible]4242
2-1	26.92524	26.76857	26.57144	26.29297	25.93055	25.48059
2-2	51.25740	51.17528	51.07244	50.92812	50.74196	50.51349
1-3	95.60337	95.55937	95.50433	95.42723	95.32801	95.20660
3-1	96.75098	96.70750	96.65312	96.57694	96.47890	96.35894
2-3	125.71711	125.68365	125.64181	125.58321	125.50783	125.41564
3-2	128.54042	128.50769	128.46677	128.40946	128.33575	128.24559
3-3	243.68183	243.66457	243.64299	243.61278	243.57393	243.52643

Table 4.5 Non-dimensional natural frequencies influenced by various applied voltages for C-C-F-F microplate

Boundary Conditions: F-F-F-C
Plate thickness : 2 microns
Gap : 2 microns
Side dimensions : 300 x 300 microns
3 orthogonal polynomials used in each direction

	Applied voltage, V (volts)						
Vibration Mode	**0**	**10**	**12**	**14**	**16**	**18**	**20**
1-1	5.88392	5.11943	4.74418	4.25829	3.61743	2.71398	0.98618
1-2	22.28818	22.09866	22.01476	21.91519	21.79973	21.66813	21.52010
2-1	25.64457	25.48003	25.40730	25.32107	25.22121	25.10755	24.97992
2-2	48.07359	47.98602	47.94743	47.90180	47.84909	47.78928	47.72234
1-3	74.18189	74.12517	74.10020	74.07068	74.03660	73.99796	73.95475
3-1	95.58796	95.54395	95.52458	95.50168	95.47525	95.44529	95.41179
2-3	103.92371	103.88323	103.86541	103.84435	103.82005	103.79250	103.76169
3-2	124.90794	124.87426	124.85944	124.84192	124.82171	124.79879	124.77317
3-3	210.47529	210.45531	210.44652	210.43612	210.42413	210.41054	210.39535

Table 4.6 Non-dimensional natural frequencies influenced by various applied voltages for cantilever (F-F-F-C) microplate

Boundary Conditions: C-C-C-C
Plate thickness : 2 microns
Applied Voltage : 0 volt
Side dimensions : 300 x 300 microns
3 orthogonal polynomials used in each direction

Vibration Mode	Gap, d (microns) 2.0	0.5	0.3	0.1
1-1	35.98997	35.98887	35.97579	32.36309
1-2	74.18434	74.18381	74.17747	72.49420
2-1	74.18434	74.18381	74.17747	72.49420
2-2	108.59098	108.59061	108.58628	107.44344
1-3	137.29385	137.29356	137.29013	136.38802
3-1	138.07004	138.06975	138.06635	137.16934
2-3	168.81909	168.81885	168.81606	168.08324
3-2	168.81909	168.81885	168.81606	168.08324
3-3	224.17874	224.17856	224.17646	223.62513

Table 4.7 Non-dimensional natural frequencies of a C-C-C-C microplate showing the influence of the Casimir effect

Boundary Conditions: F-F-F-C

Plate thickness : 2 microns

Applied Voltage : 0 volt

Side dimensions : 300 x 300 microns

3 orthogonal polynomials used in each direction

	Gap, d (microns)							
Vibration Mode	**2.00**	**1.00**	**0.75**	**0.50**	**0.25**	**0.20**	**0.15**	**0.10**
1-1	5.884	5.884	5.883	5.877	5.664	5.184	1.405	0.000
1-2	22.288	22.288	22.288	22.286	22.231	22.114	21.543	15.775
2-1	25.645	25.645	25.644	25.643	25.595	25.493	25.000	20.242
2-2	48.074	48.074	48.073	48.073	48.047	47.993	47.733	45.422
1-3	74.182	74.182	74.182	74.181	74.165	74.130	73.962	72.492
3-1	95.588	95.588	95.588	95.588	95.575	95.547	95.417	94.282
2-3	103.924	103.924	103.924	103.923	103.911	103.886	103.767	102.724
3-2	124.908	124.908	124.908	124.908	124.898	124.877	124.777	123.912
3-3	210.475	210.475	210.475	210.475	210.469	210.457	210.398	209.886

Table 4.8 Non-dimensional natural frequencies of a F-F-F-C microplate showing the influence of the Casimir effect

Plate thickness : 2 microns
Gap : 2 microns
Side dimensions : 300 x 300 microns
3 orthogonal polynomials used in each direction

Vibration Mode	C-C-C-C	C-F-C-C	C-F-C-F	C-C-F-F-	F-F-F-C
1-1	35.51943	23.73376	23.03999	4.66431	0.98618
1-2	73.95721	40.98644	37.76873	25.48153	21.52010
2-1	73.95721	64.83203	64.40400	26.29297	24.97992
2-2	108.43594	82.83284	80.50322	50.92812	47.72234
1-3	137.17125	109.96078	87.94047	95.42723	73.95475
3-1	137.94814	129.62930	129.31094	96.57694	95.41179
2-3	168.71940	147.24679	134.06422	125.58321	103.76169
3-2	168.71940	157.51043	145.51278	128.40946	124.77317
3-3	224.10368	227.13034	202.16307	243.61278	210.39535

Table 4.9 Non-dimensional natural frequencies for various boundary conditions and subjected to an applied voltage of 20 volts and the Casimir effect

4.2 CURVE VEERING

Leissa (1974) demonstrated the curve veering aberration using the well-known solution to the problem of a vibrating membrane in which the phenomenon was proved to occur when an approximate method, the Galerkin Method, was used to obtain the frequency curves. The plots show that the curves corresponding to λ^2_{31} and λ^2_{13} plotted against the side ratio veered away from each other as shown in Fig. 1.2. Using an exact solution the corresponding curves crossed at $a/b = 1$. He went on further to show that for a rectangular plate there are 21 distinct cases having clamped, simply supported, or free boundaries. Exact solutions exist for six of these cases – those having at least two opposite edges simply supported. Frequency coalescence was exhibited in these curves while the other fifteen having approximate solutions exhibited curve veering.

In the present thesis, the natural frequencies of vibration are plotted against a geometric parameter, the side ratio a/b of the microplate, ranging from 0.1 to 3. The results are obtained using a computer program written in *MATLAB*. 3 orthogonal polynomials are used in each direction to obtain the first 9 modes of vibration used for the plots. Fig. 4.1 shows the natural frequencies plotted against side ratio in which the electrostatic force and the Casimir force are not considered. The MUMPs technology used for the design of the plates requires that the gap (Oxide1) and first structural layer (Poly1) have a thickness of 2 μm, respectively. The design is modeled as a microplate with boundary conditions that are clamped on all four sides. From this figure it appears that the symmetric modes of vibration cross each other at certain values of the side ratio. In particular, the 2-1 and 1-2, the 3-1 and 1-3, and the 2-3 and 3-2 modes of vibration all appear to cross at a side

ratio of 1.0. However on a closer inspection as illustrated by Fig. 4.1a, the symmetric modes do not actually cross but veer away from each other on approach at a side ratio of 1.0 (not shown in Fig. 4.1). At this value of *a/b* it is seen that the curve for the 1-3 natural vibration frequency abruptly but continuously changes, rapidly increasing in curvature until it reaches a curvature that is coincident with the path the 3-1 curve would have taken had it crossed with the 1-3 mode at a side ratio of 1.0. The 1-3 mode continues along this path in a smooth curve until it encounters another curve. Similarly the curve for the natural frequency of the 3-1 mode abruptly but continuously changes to go along the path the 1-3 mode would have taken immediately after the side ratio of 1.0. They do not cross as expected. The same curve veering behavior is applicable to the natural frequency for the1-2, 2-1 and 2-3, 3-2 modes of vibration as shown in Fig. 4.1a.

An implication of curve veering introduced by approximate analysis is made more apparent in the estimation of natural frequencies for capacitive microplates used as MEMS actuators. In these systems it is desirous to obtain the maximum possible amplitude of excitation, which occurs close to a specific frequency of interest. Supposing a designer was interested in excitations of the 2-1 mode for a microplate with a side ratio of 1.2. An analysis carried out would expect the non-dimensional natural frequency to be 80. As a result of curve veering introduced by the approximate analysis, numerical results would be obtained as 100 corresponding to the assumed continuity of the 2-1 curve which is in fact the 1-2 curve and introduces a very significant error as illustrated in Fig. 4.1a.

Curve veering is not limited to natural frequencies corresponding to a side ratio of 1.0 but also occurs at side ratios of 0.84, 0.77 and 0.65 for the C-C-C-C microplate as shown in Fig. 4.1a and highlighted in Figs. 4.1b, 4.1c and 4.1d respectively. These results are summarized in Table 4.4. At a side ratio of 0.84, the frequency modes of 3-1 and 2-3 veer away from each other rather than cross as shown in Fig. 4.1b. In particular, the curve for the 3-1 mode veers abruptly and continuously to go along the path the curve the 2-3 mode would have followed had there been frequency coalescence of the curves. At a side ratio of 0.77, the modes represented by the 2-2 and 1-3 veer away from each other, resulting in curve veering or an *avoided crossing* as it is sometimes referred to in the literature and indicated in Fig. 4.1c. Fig. 4.1d shows the curve veering behaviour at a side ratio of 0.65. The interacting modes of vibration are the 2-1 and 2-2.

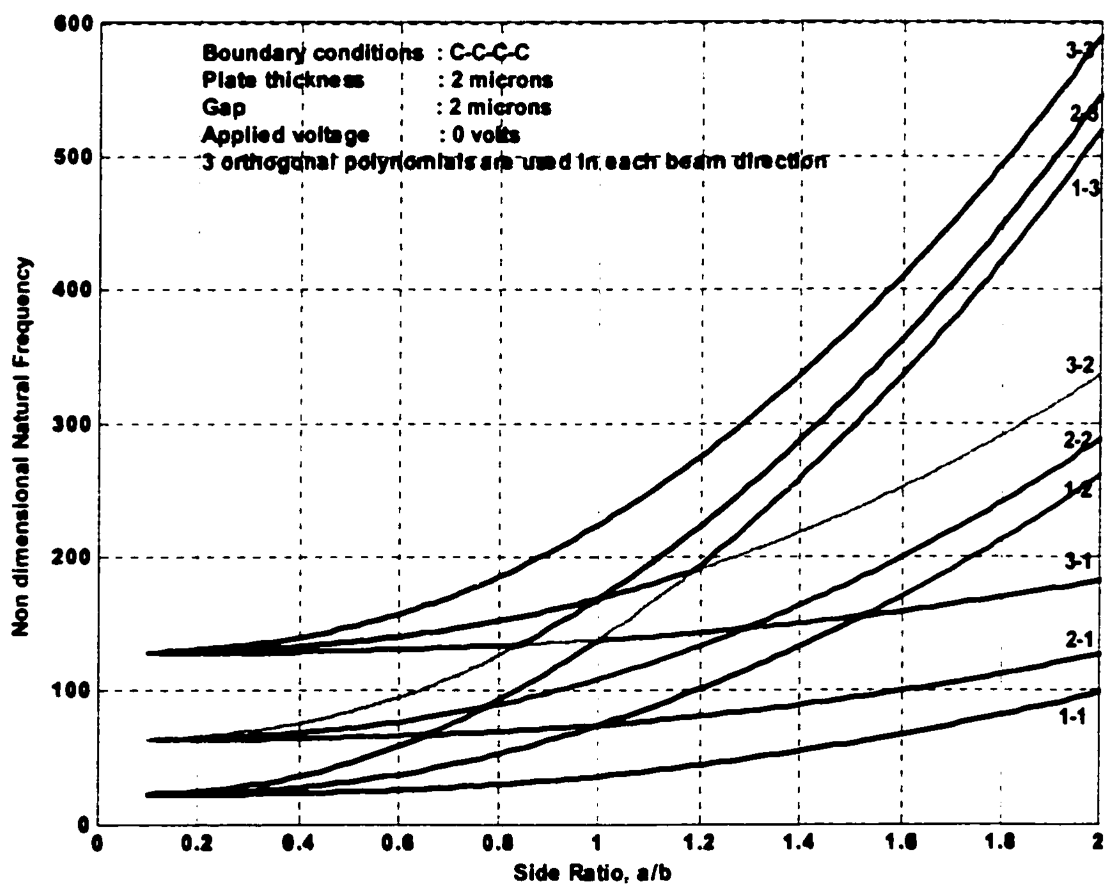

Fig. 4.1 Natural frequency versus side ratio for a C-C-C-C microplate

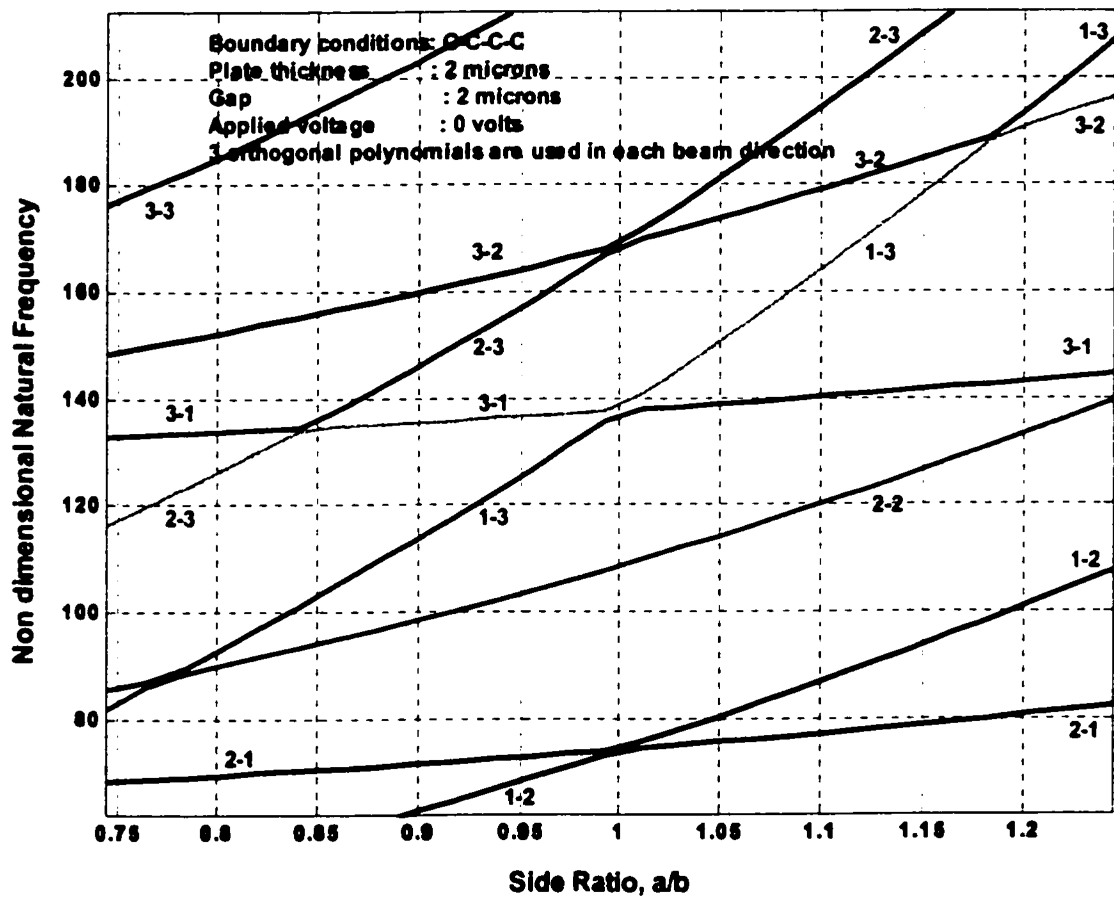

Fig. 4.1a Natural frequency versus side ratio showing curve veering

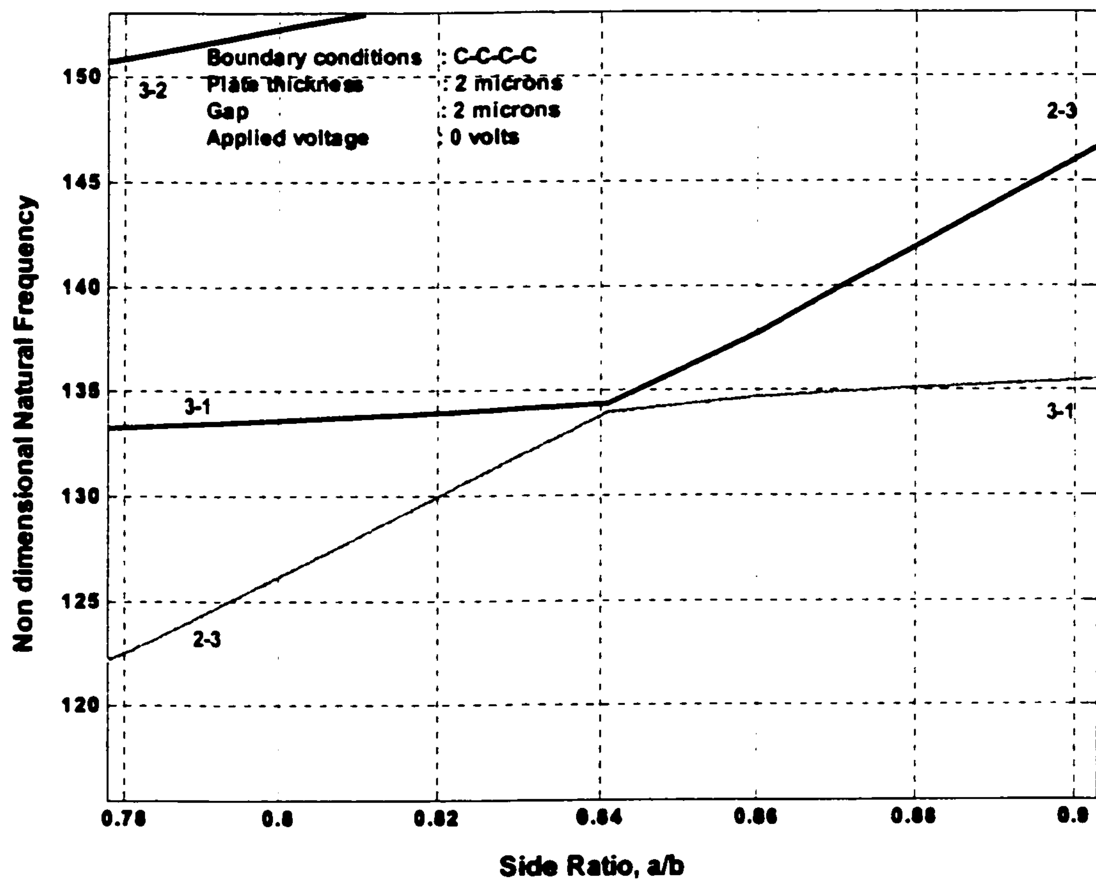

Fig. 4.1b Curve veering between modes 3-1 and 2-3 at a side ratio of 0.84

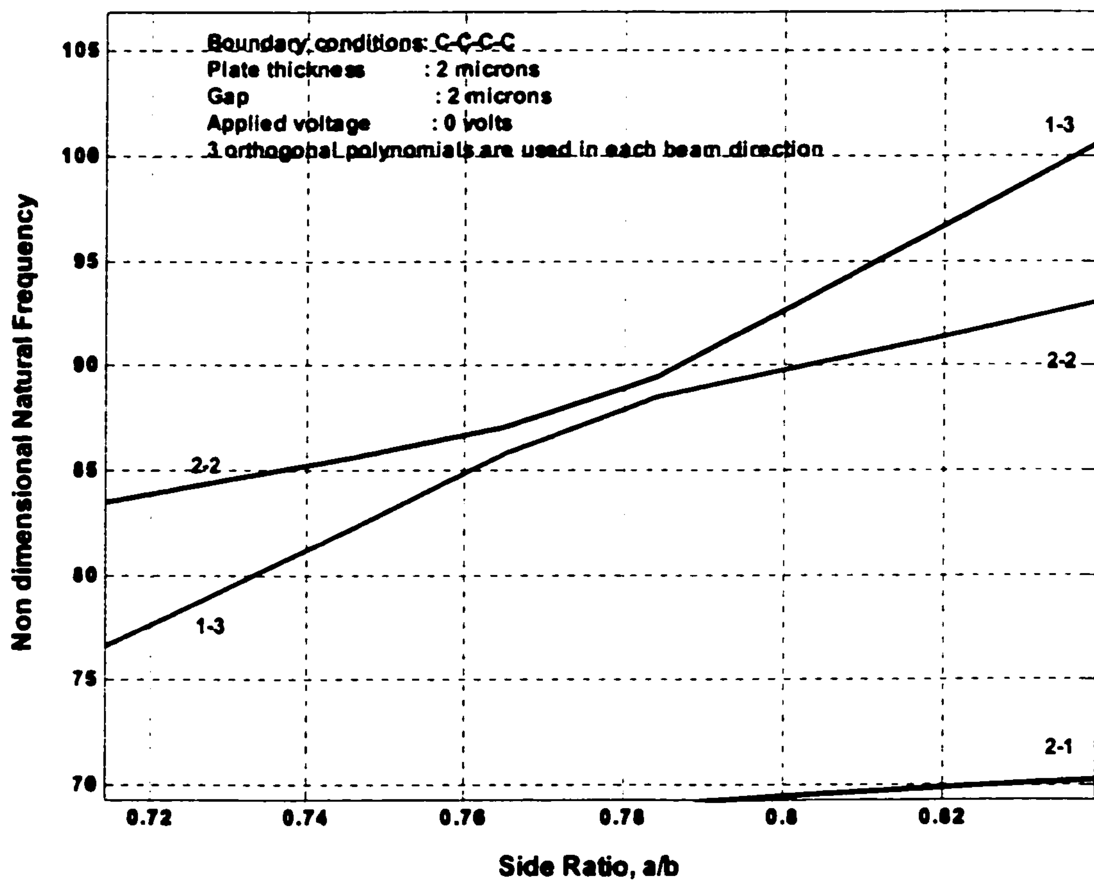

Fig. 4.1c Curve veering between modes 2-2 and 1-3 at a side ratio of 0.77

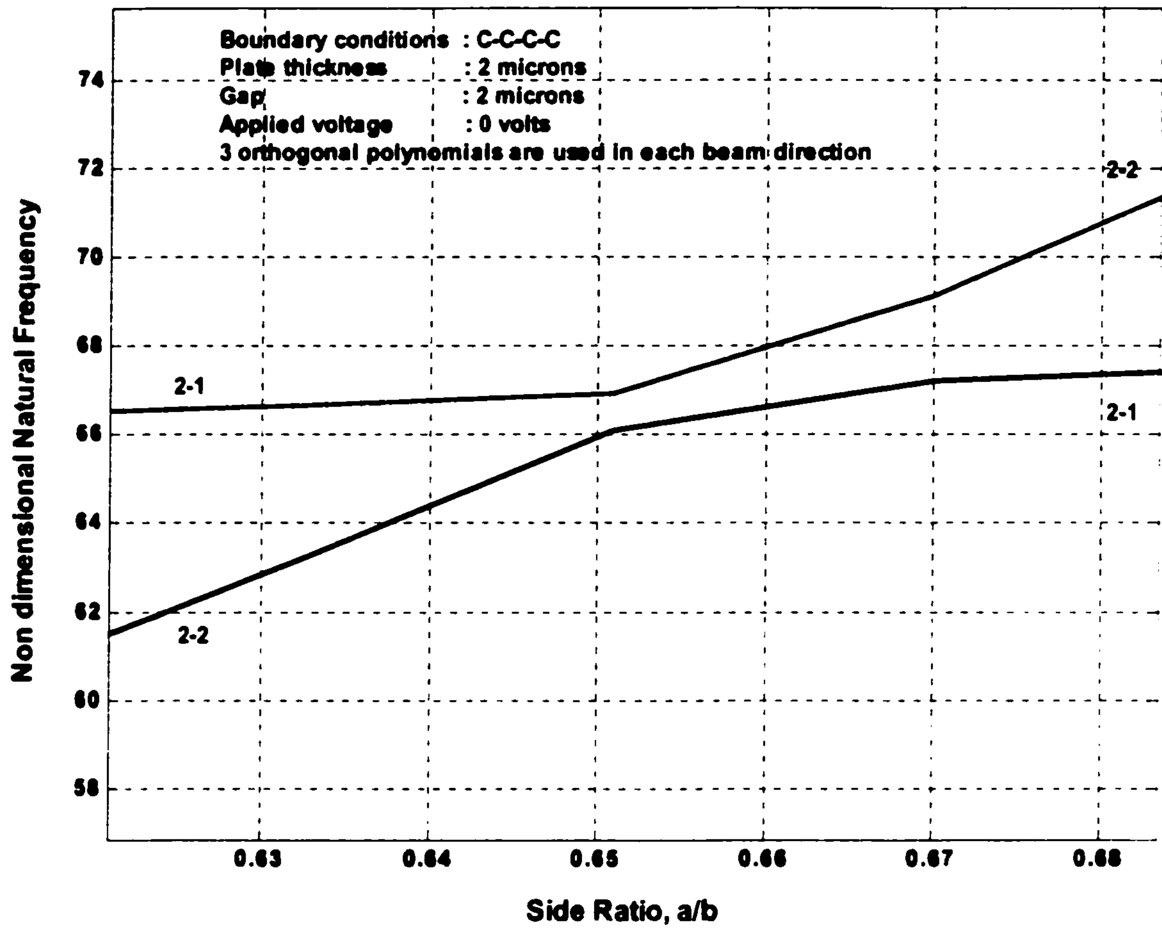

Fig 4.1d Curve veering between modes 2-1 and 2-2 at a side ratio of 0.651

It is interesting to note that as Leissa (1974), pointed out, the curves behave "like a dragonfly in one instant and a butterfly the next". The curve veer locations shown after the side ratio of 1 in Fig. 4.1a are identical to those before this value simply noting that the side ratio in the latter case is the same for corresponding cases of the rectangular plate rotated through 90 degrees. It is further noted that veering is strongest with 1-3 and 3-1 modes, this being the mode that accounts for the greatest inaccuracy to the deflection function in this 3-term solution as shown in Tables 4.1 and 4.2.

The foregoing discussion on natural frequencies has not considered the influence of the electrostatic force or the Casimir effect in the analysis. The effect of the application of 110 volts was shown in Table 4.2 and is depicted graphically in Fig. 4.2. This figure shows the variation of natural frequency with the side ratio *a/b* ranging from 0.1 to 3. The plots show an apparent coalescence of the curves for various frequency modes of vibration. A closer examination of these curves in the region around the side ratio of 1.0 show the phenomenon of curve veering present between modes 1-2/2-1, 1-3/3-1 and 2-3/3-2, depicted in Fig. 4.2a (not obvious from Fig. 4.2). The veering occurring at other locations in the side ratio domain are shown in Figs. 4.2b, 4.2c and 4.2d for the interactions of the 3-1/2-3, 2-2/1-3 and 2-1/2-2 at side ratios of 0.825, 0.776 and 0.66, respectively. It is to be noted that the effect of the electrostatic loading causes the locations of the curve veering to shift from the side ratios corresponding to veering in an unloaded state. The curves also show that the loading intensities resulting from the voltage application cause the plates to become unstable at certain side ratios for a given mode of vibration. This point shall be elaborated upon in a subsequent section.

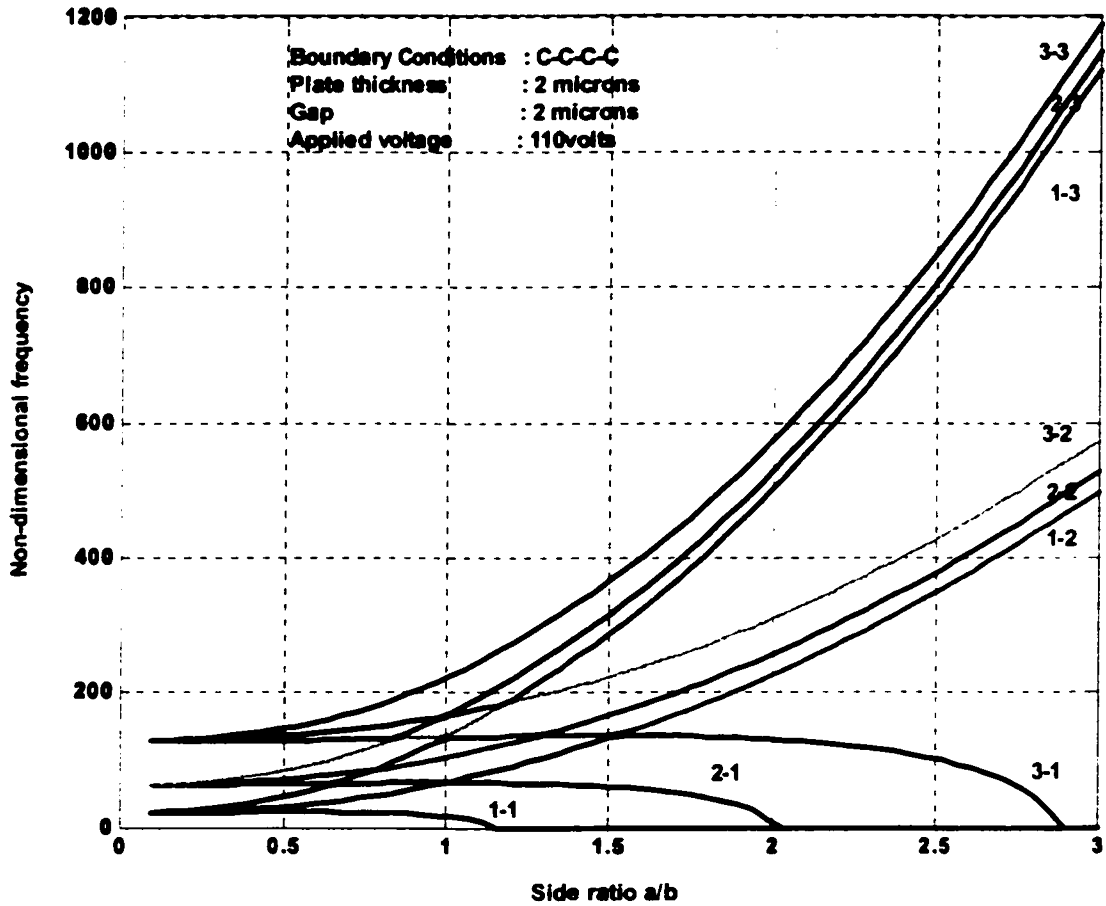

Fig. 4.2 **Natural frequency showing regions of instability for an applied voltage of 110 volts**

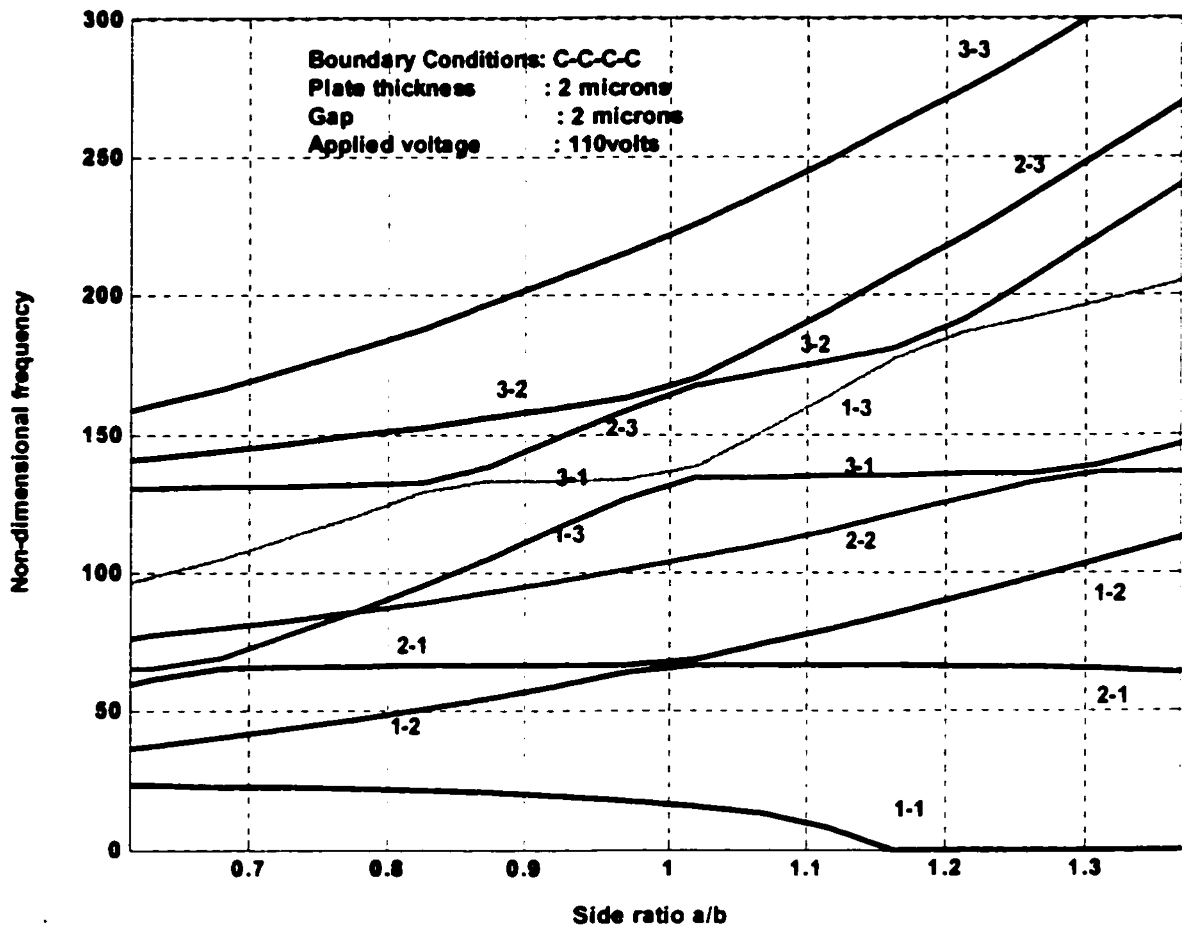

Fig. 4.2a Natural frequency versus side ratio for an applied voltage of 110 volts showing curve veering

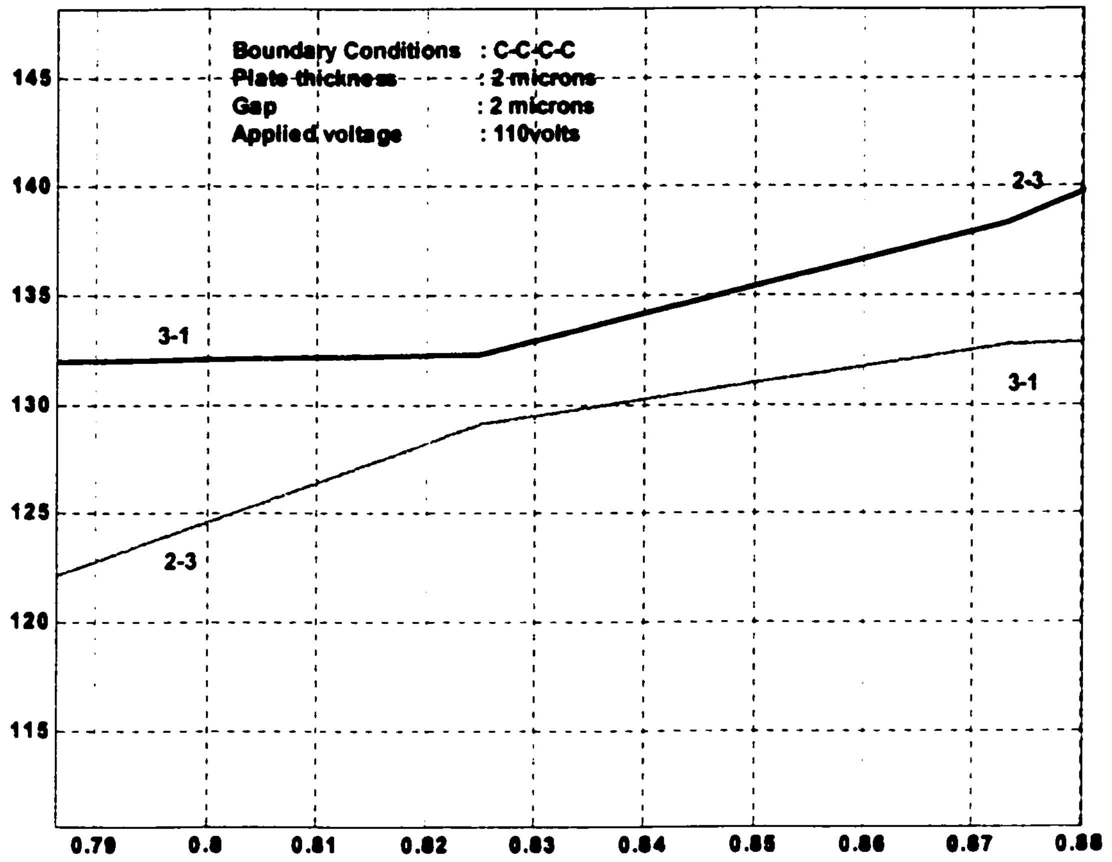

Fig. 4.2b Curve veering between modes 3-1 and 2-3 at a side ratio of 0.84

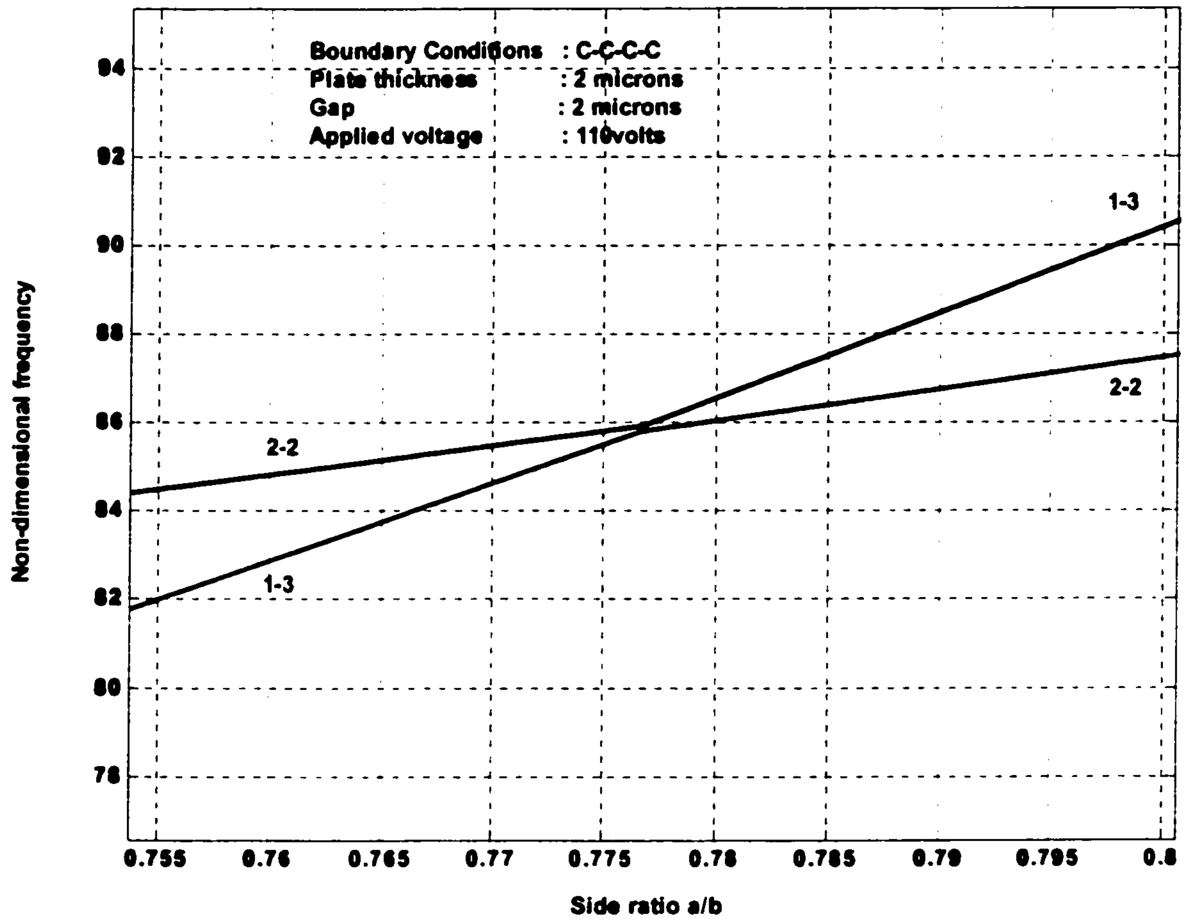

Fig. 4.2c Curve veering for modes 2-2 and 1-3 at a side ratio of 0.776

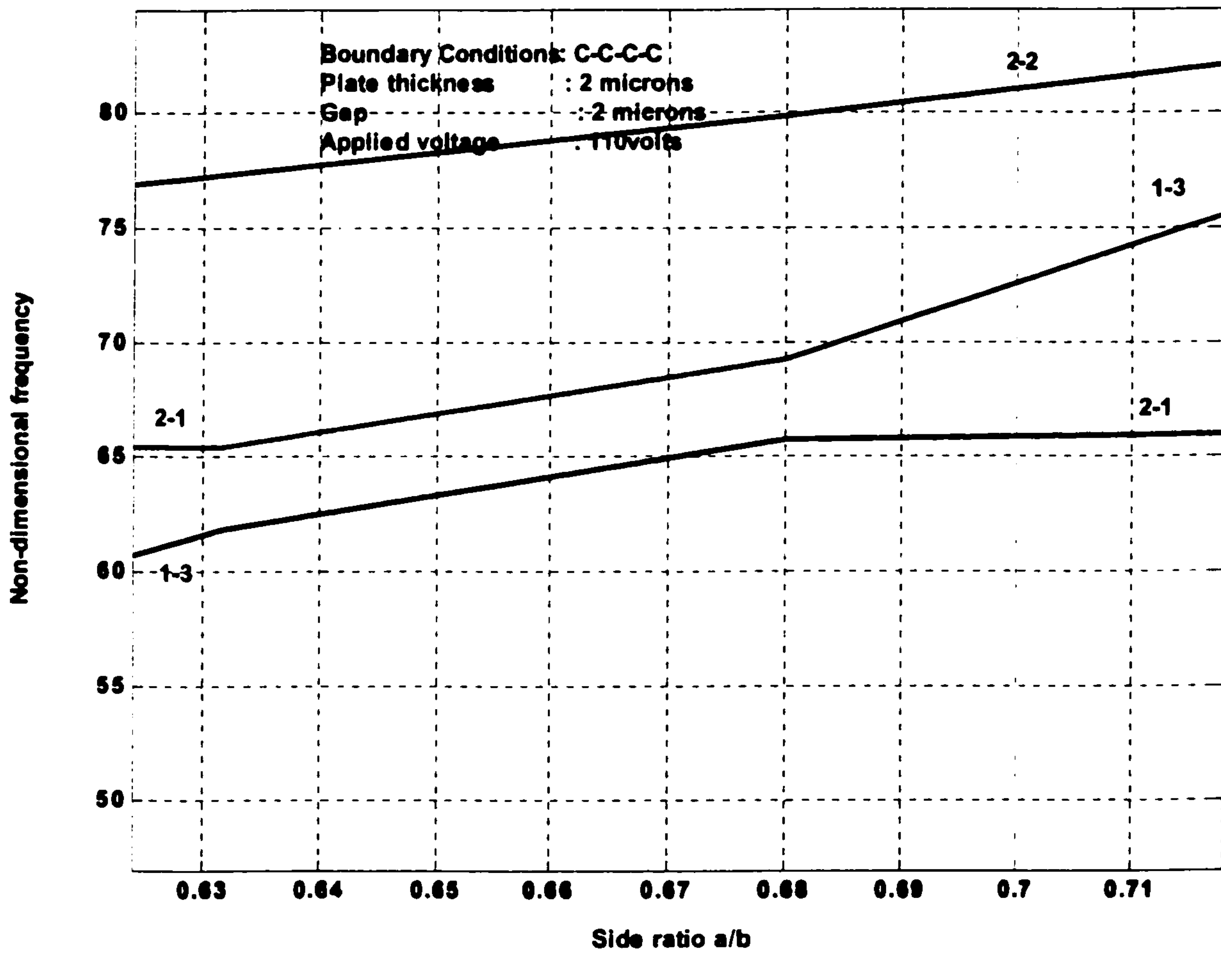

Fig. 4.2d Curve veering for modes 2-1 and 2-2 at a side ratio of 0.66

Thus far curve veering of the frequency plots have been considered based on an approximate analysis using 3 orthogonal polynomials in each of the directions in the Rayleigh-Ritz method. As mentioned earlier and shown in Table 4.1, improved accuracy of the non-dimensional natural frequencies was obtained using 6 orthogonal polynomials in each direction. A plot of the non-dimensional natural frequency using these 6 orthogonal polynomials and in the absence of any external loading intensity for a C-C-C-C microplate is shown in Fig. 4.3. Although 36 natural frequencies are calculated from the Rayleigh-Ritz method, only the first 9 are depicted for comparison with solutions using 3 orthogonal polynomials earlier shown in Fig. 4.1. A closer examination of the behavior of the plots is shown in Fig. 4.3a, which highlights the avoided crossings at a side ratio of 1.0. Once again curve veering is seen to occur between the 1-2/2-1, 1-3/3-1 and 2-3/3-1 modes of vibration, which was obtained using 3 orthogonal polynomials and shown in Figs. 4.1. However, the multiplicity of the locations of avoided crossings is markedly different in the side ratio domain for a 6-OP solution. At a side ratio of 0.825 one observes that there are actually 2 pairs of interacting modes of vibration exhibiting curve veering. At non-dimensional frequencies of about 128 and 148, the 3-1/2-3 and 3-2/3-3 modes veer away from each other as illustrated in Fig. 4.3b. It is instructive to note that in the 3-OP solution for a side ratio of 0.84 (Fig. 4.2b), only the 3-1/2-3 mode of vibration were present to exhibit veering. The 6-OP solution results in an avoided crossing occurring at a side ratio of 0.80 between the 2-2 and 1-3 modes (Fig. 4.3c), similar to the 3-OP solution but with a shift in location to 0.77 in the latter (Fig. 4.2c). At a side ratio of 0.776 for this 6-OP solution, curve veering is exhibited between the 2-3 and 3-2 modes, which is a repetition of the mode interaction for curve veering that

occurred at a side ratio of 1.0 but at a higher non-dimensional frequency value (Fig. 4.3d). Once again for an *a/b* value of 0.68 we have 2 pairs of modes interacting to exhibit the curve veering phenomenon; the 2-1/2-2 and 3-1/2-3 at non-dimensional frequencies of 67 and 105 respectively (Fig 4.3e). This compares with a single interaction mode of 2-1/2-2 obtained with the 3-OP solution and occurring at 0.651 for about the same frequency (see Fig.4.1d). The multiplicity of veering is made more manifest in Fig. 4.3f. In this range the veer points occur for side ratios of 0.439 and 0.486 for the 2-3/3-2 and 2-2/1-3 modes of vibration respectively.

The application of 110 volts to the plate creates an electrostatic field that results in the frequency curves shown in Figs. 4.4 using a 6-OP solution. The behavior is similar to that obtained in Figs 4.3 but with minor shifts in location accounted for by the electrostatic load. The curves also show locations of instability for the 1-1, 1-2 and 2-1 modes of vibration for side ratios ranging from 0.1 to 3.0. The influence of voltage and other system parameters on the natural frequency of the system shall be discussed shortly.

The effect of the boundary conditions on the location of curve veering will now be examined.

The variation of non-dimensional natural frequencies with side ratio for a C-C-F-F microplate is shown in Figs. 4.5. A comparison of Fig 4.1a and Fig 4.5a show the location of curve veering to be the same for the C-C-F-F and C-C-C-C boundary conditions occurring at a side ratios of 1.0. The C-C-F-F plate has lower natural

frequencies than the C-C-C-C plate at this location. The similarity is not applicable to the curve veering locations for all the other boundary conditions, namely the C-F-C-C, C-F-C-F, and the cantilever microplate, F-F-F-C. One marked difference is that none of the microplates with these 3 boundary conditions have curve veering occurring at a side ratio of *a/b* equal to 1.0. This is shown in the Figs. 4.6, 4.7 and 4.8, respectively. In the literature on curve veering in rectangular plates, emphasis has been placed on the occurrence of this phenomenon at an aspect ratio of 1.0, which holds true for a plate simply supported on all 4 sides (S-S-S-S) as well as the C-C-C-C and C-C-F-F. The results presented here suggest that when the boundary conditions are symmetrical about a diagonal axis of the plate (with orientations as shown in Figs 3.3 to 3.8), curve veering may be expected to occur for a side ratio of *a/b* equal to 1.0, that is a square plate. For asymmetrical boundary conditions, curve veering does not occur at this side ratio.

The foregoing has implications on the solutions to frequently encountered eigenvalue problems in engineering, which require the use of well- established approximate numerical method such as the Finite Element Method. These methods should be used with greater care, as results obtained would be affected by the presence of curve veering (Bhat and Stiharu, 2000). Particular attention should be paid to the accuracy of results especially in the neighborhood of points where coalescence of curves is expected. Usually trade offs are made between accuracy and computational time. With less accurate modeling, it is expected that curve veering would influence the results to some degree. Knowing the side ratios for which veering is likely to occur would enable the analyst and designer to avoid such geometries in capacitive MEMS devices. It enables

one to avoid potentially inaccurate results in these regions, results for which device sensitivity and performance may be adversely affected.

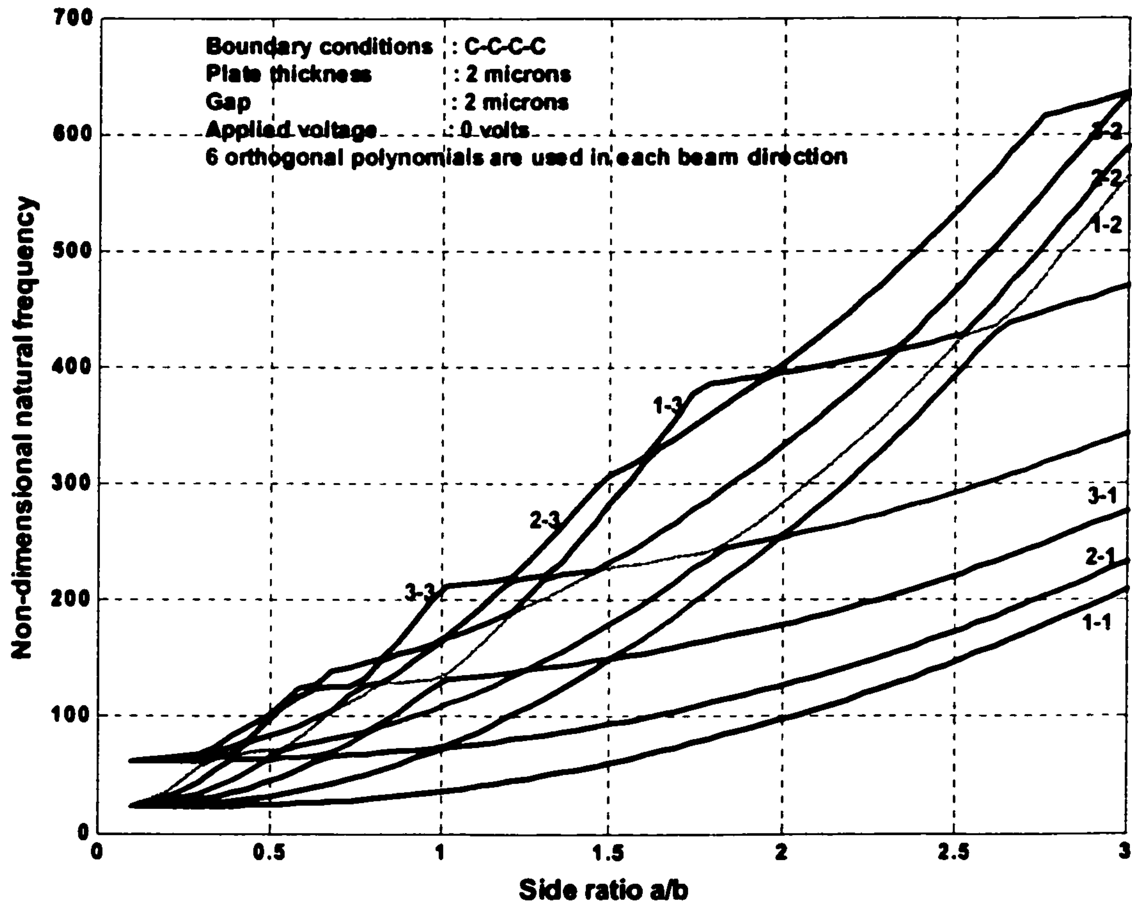

Fig. 4.3 **Natural frequency versus side ratio**

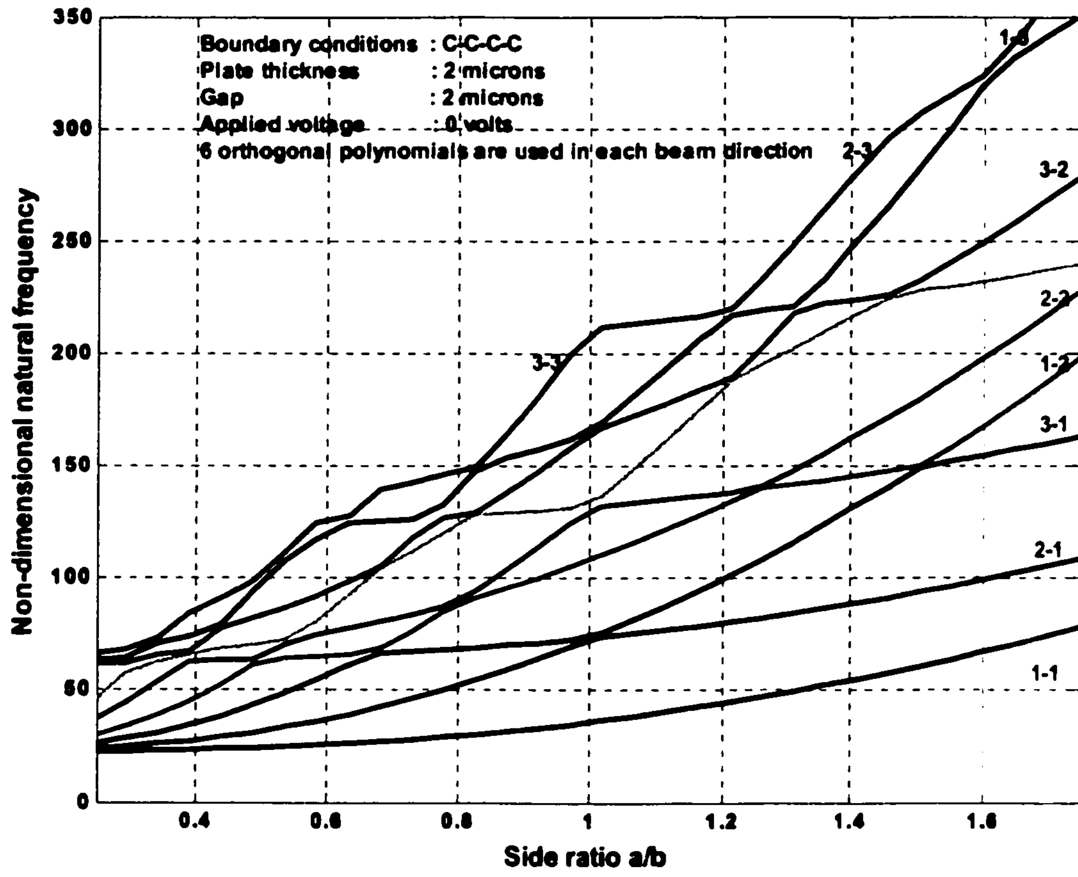

Fig. 4.3a Natural frequency versus side ratio showing curve veering

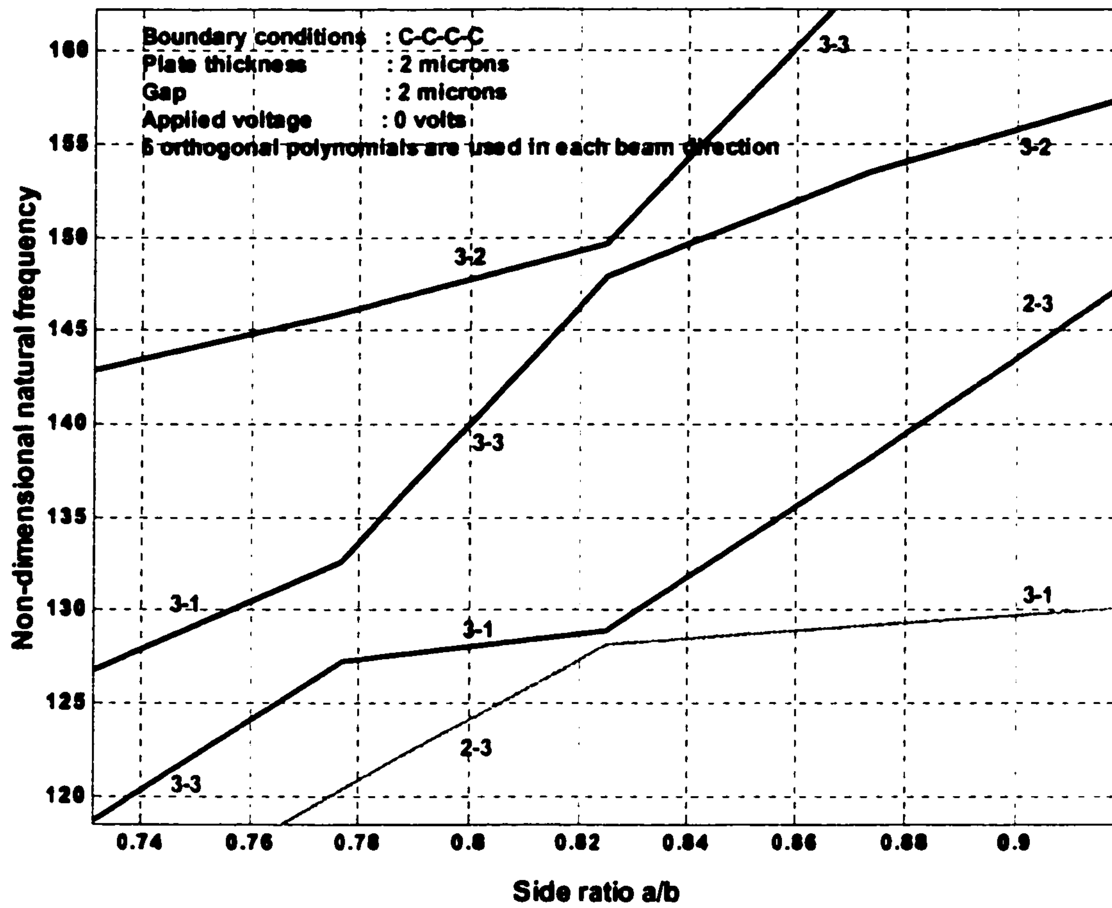

Fig. 4.3b Curve veering at a side ratio of 0.825

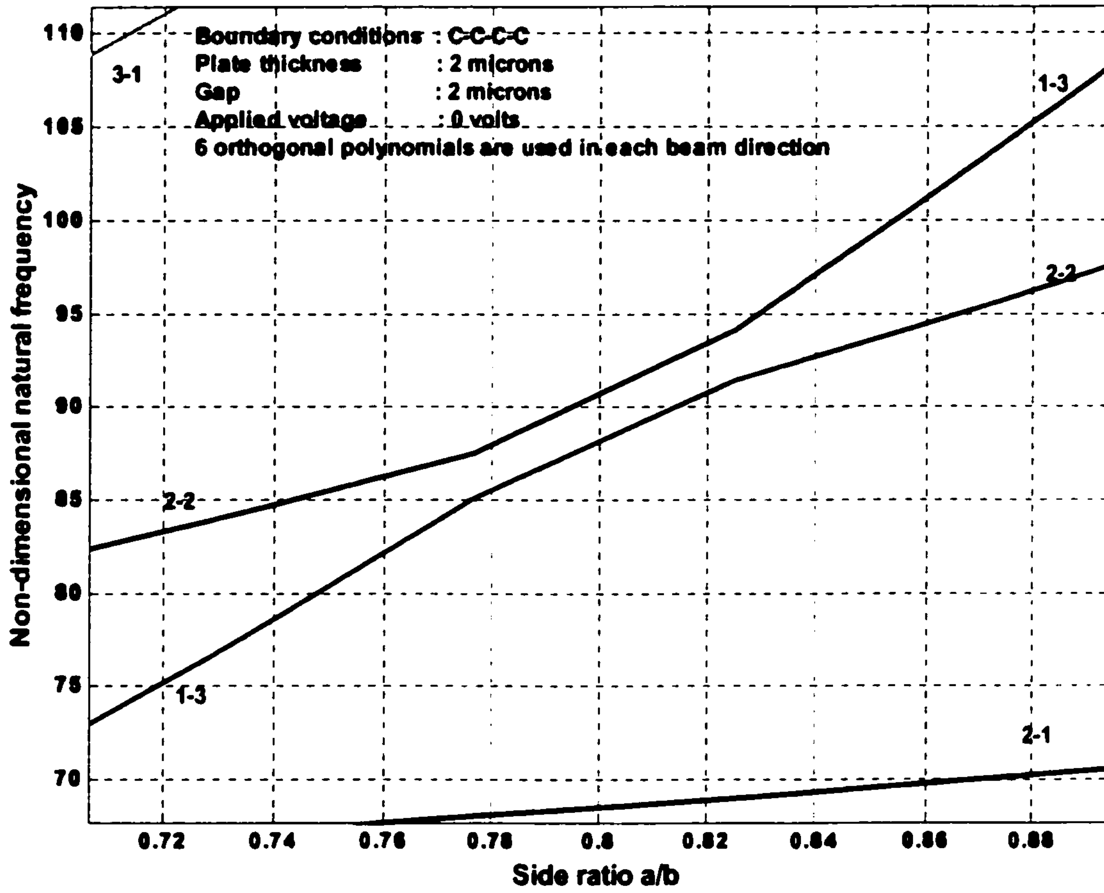

Fig. 4.3c Curve veering at a side ratio of 0.8

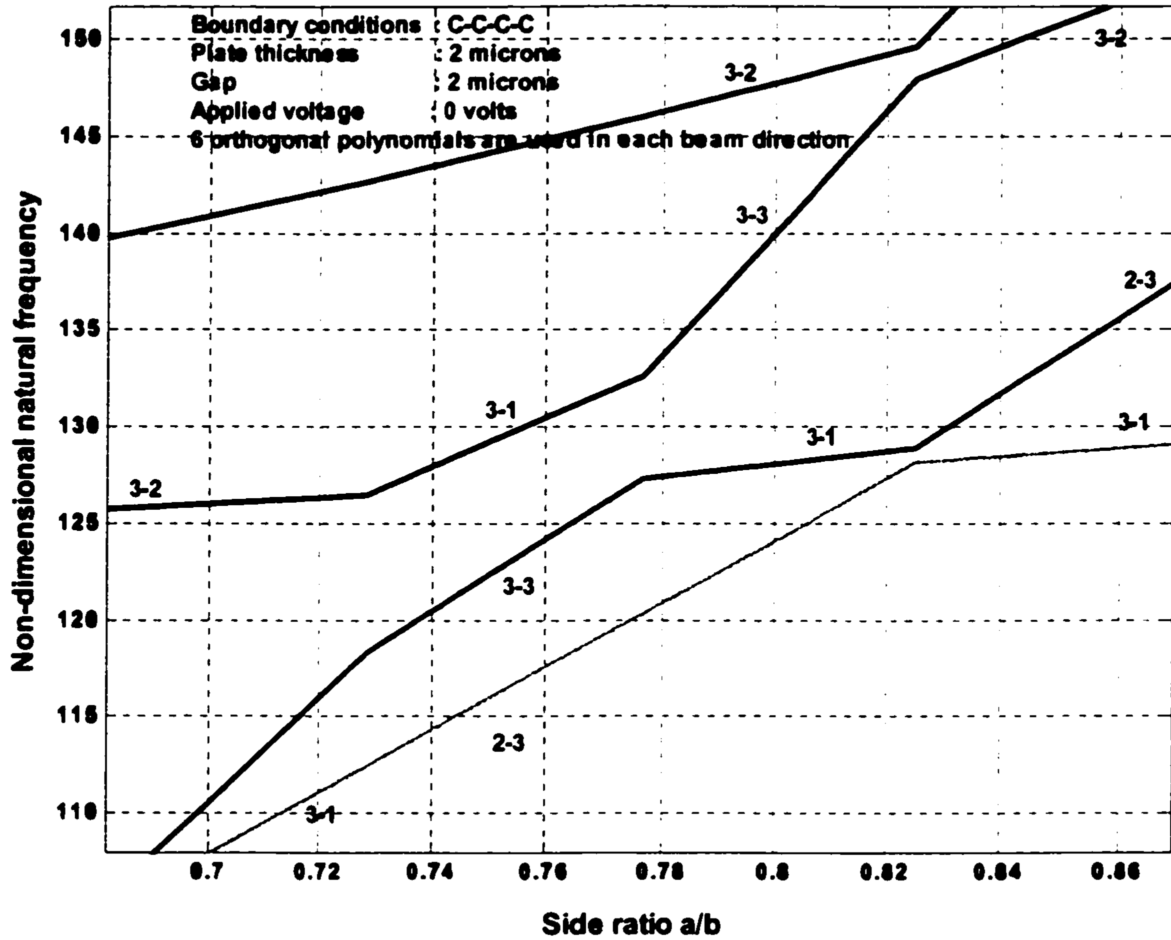

Fig. 4.3d Curve veering at a side ratio of 0.776

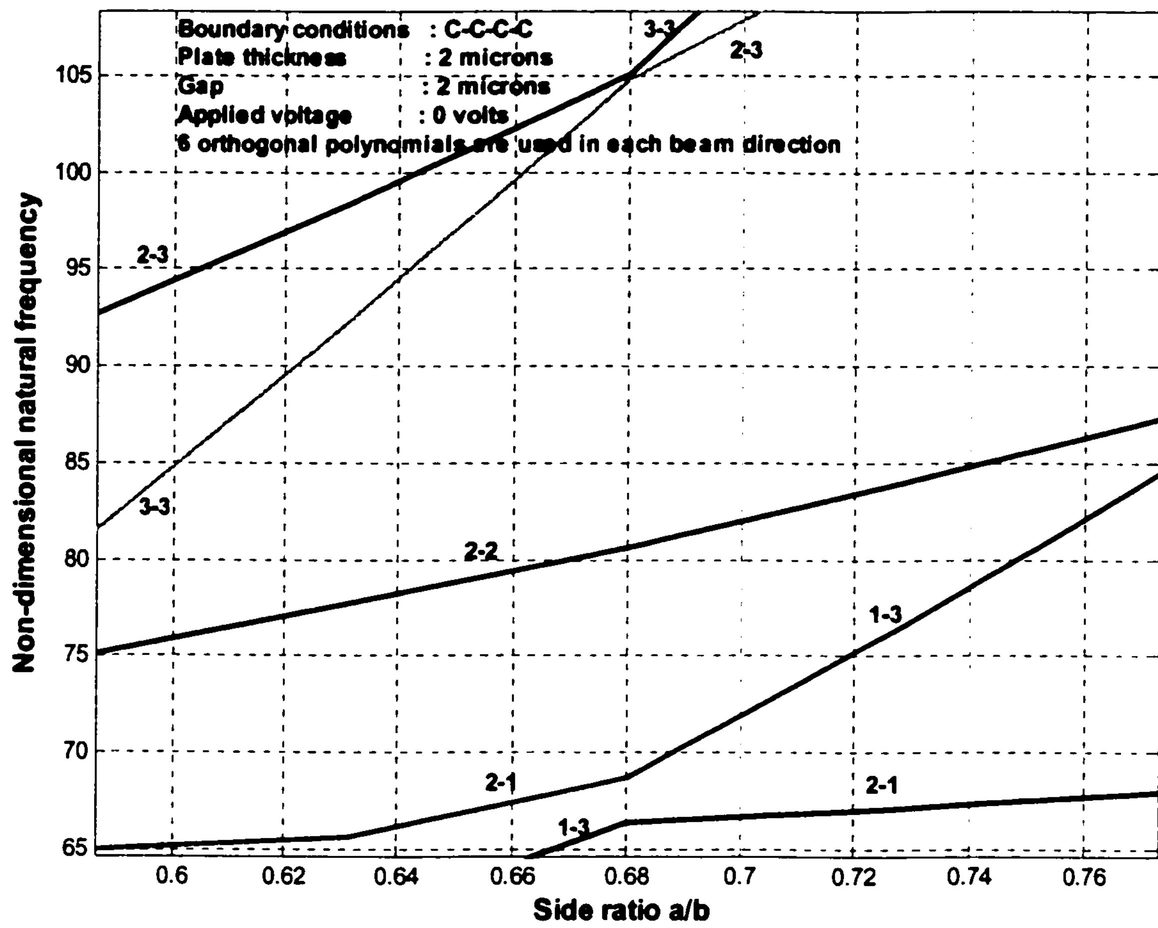

Fig. 4.3e Curve veering at a side ratio of 0.68

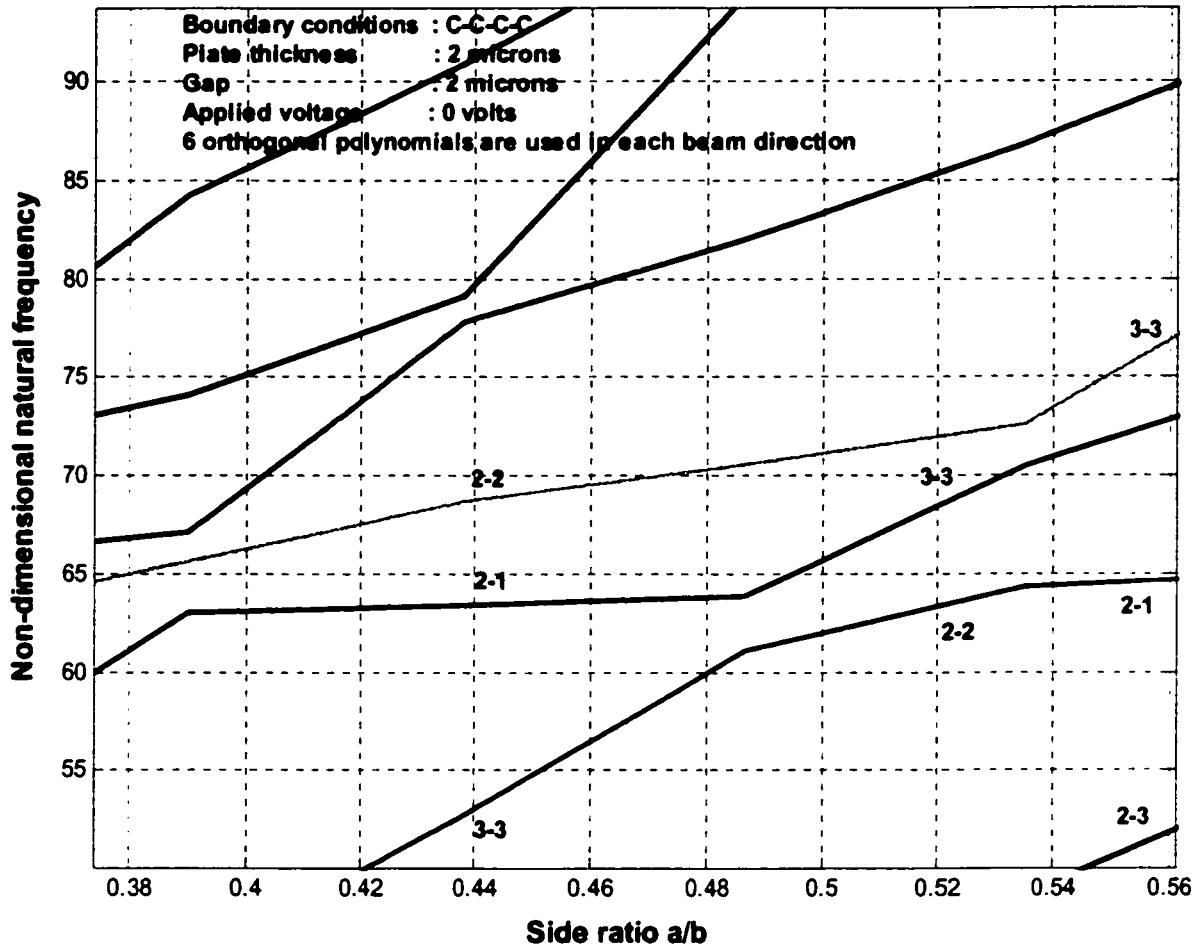

Fig. 4.3f Curve veering at side ratios of 0.535, 0.486, 0.439 and 0.39

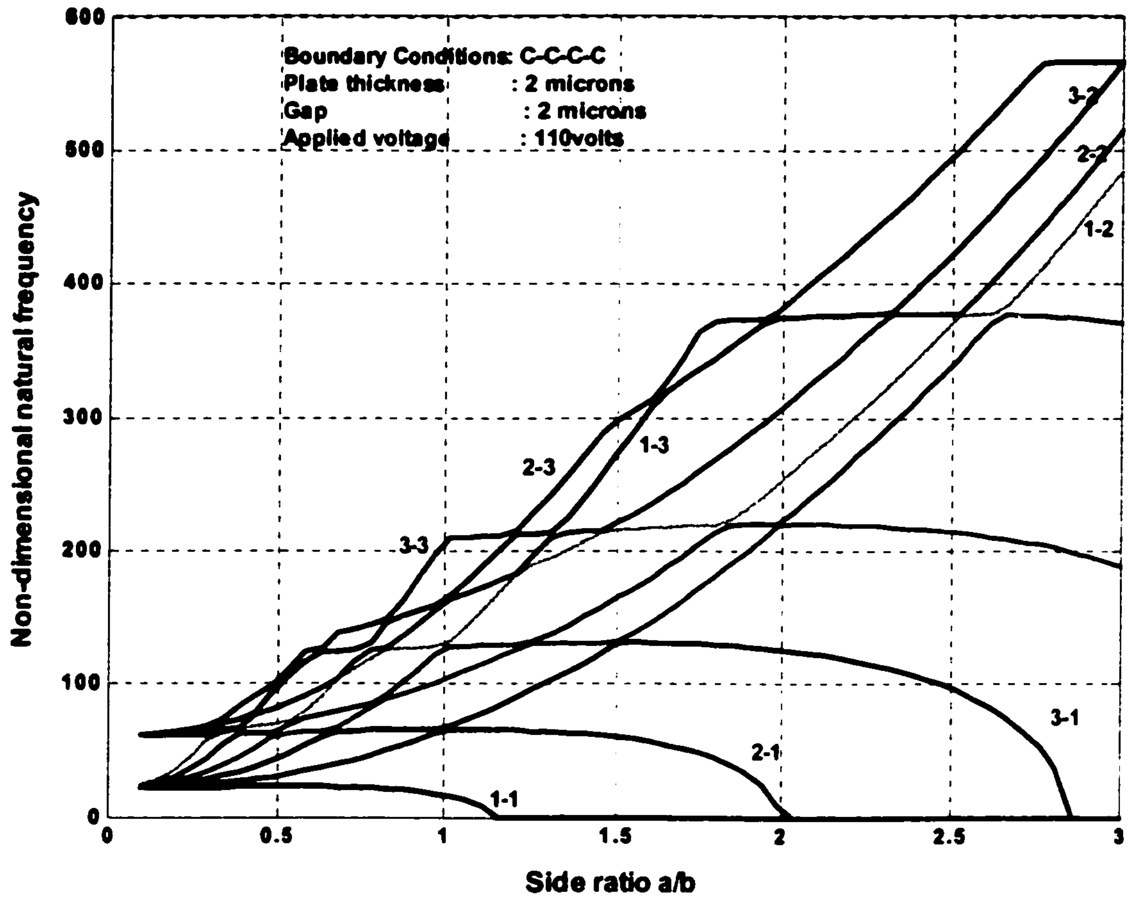

Fig. 4.4 Natural frequency showing regions of instability for an applied voltage of 110 volts

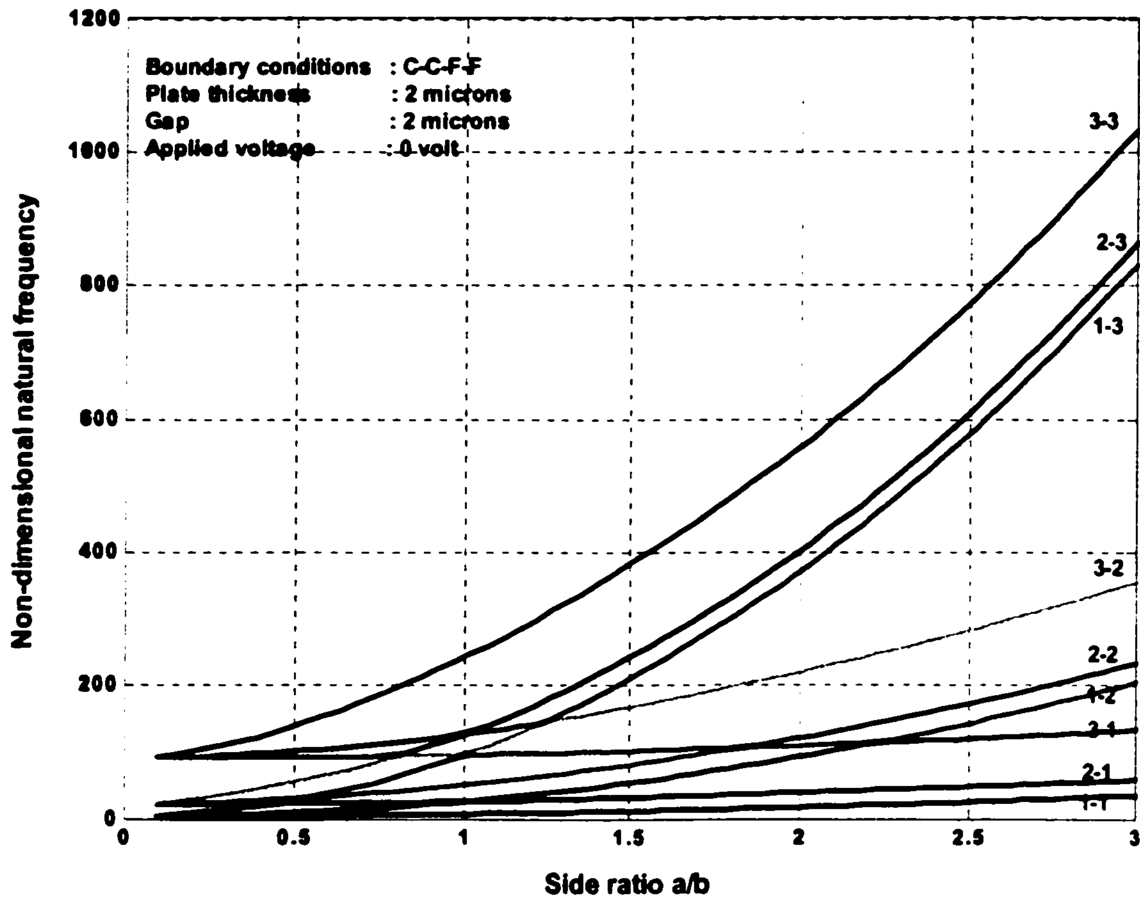

Fig. 4.5 Natural frequency versus side ratio for C-C-F-F microplate

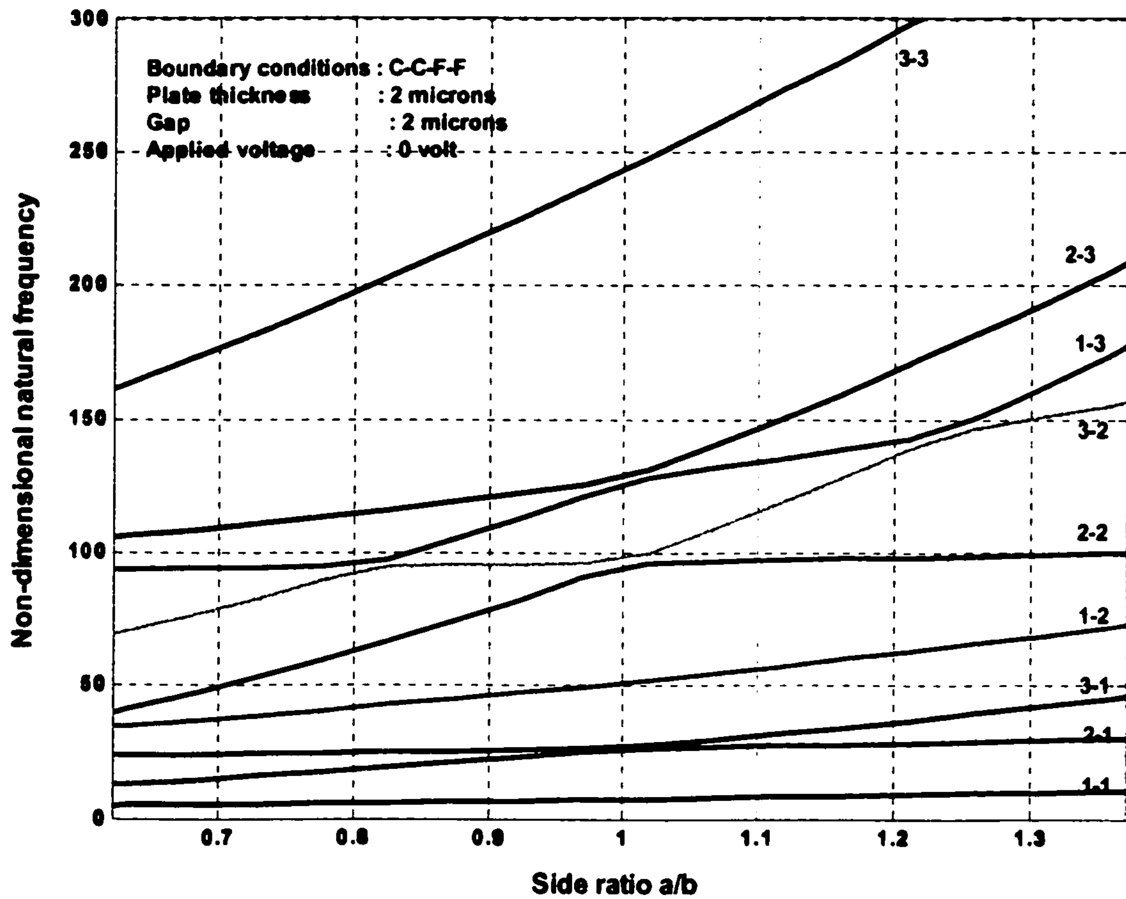

Fig. 4.5a Natural frequency versus side ratio showing curve veering for a C-C-F-F

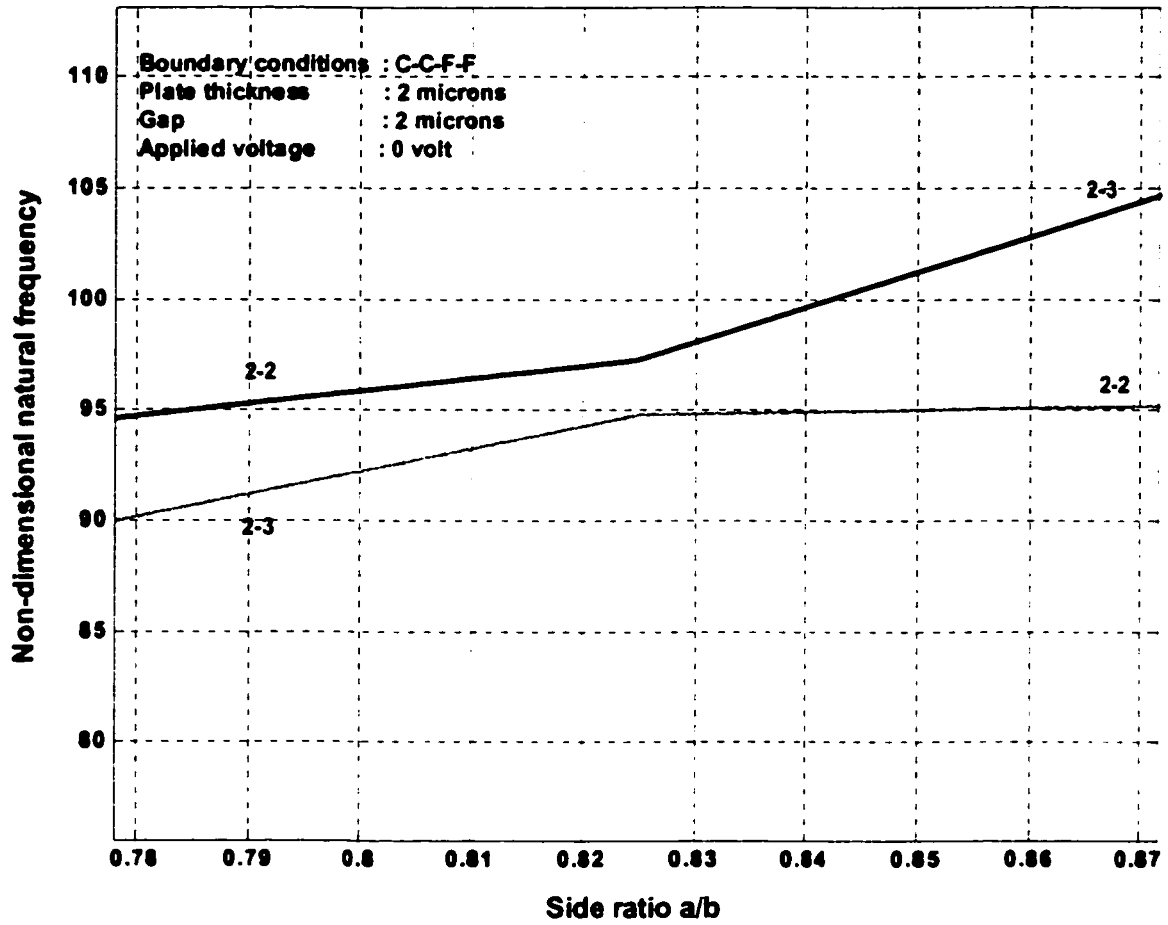

Fig. 4.5b Curve veering between modes 3-1 and 2-3 at a side ratio of 0.825

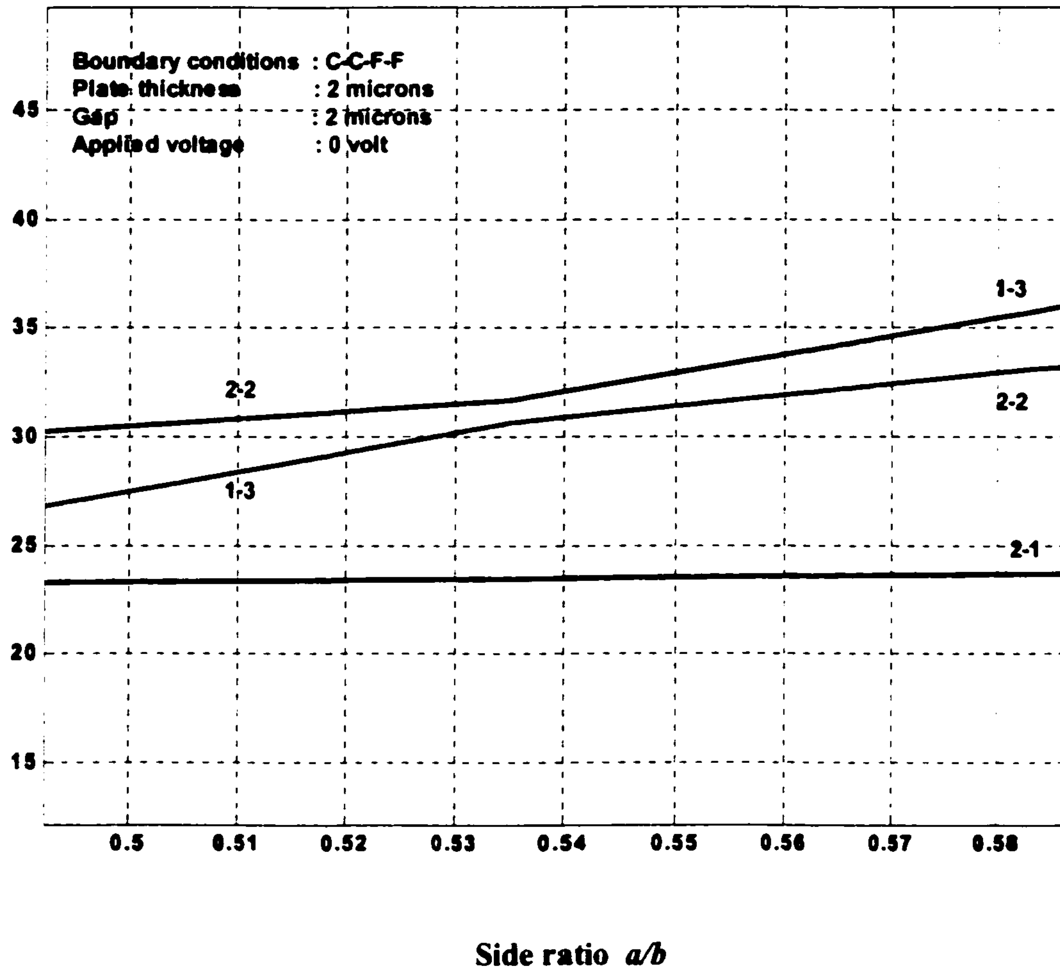

Fig. 4.5c Curve veering between modes 2-2 and 1-3 at a side ratio of 0.535

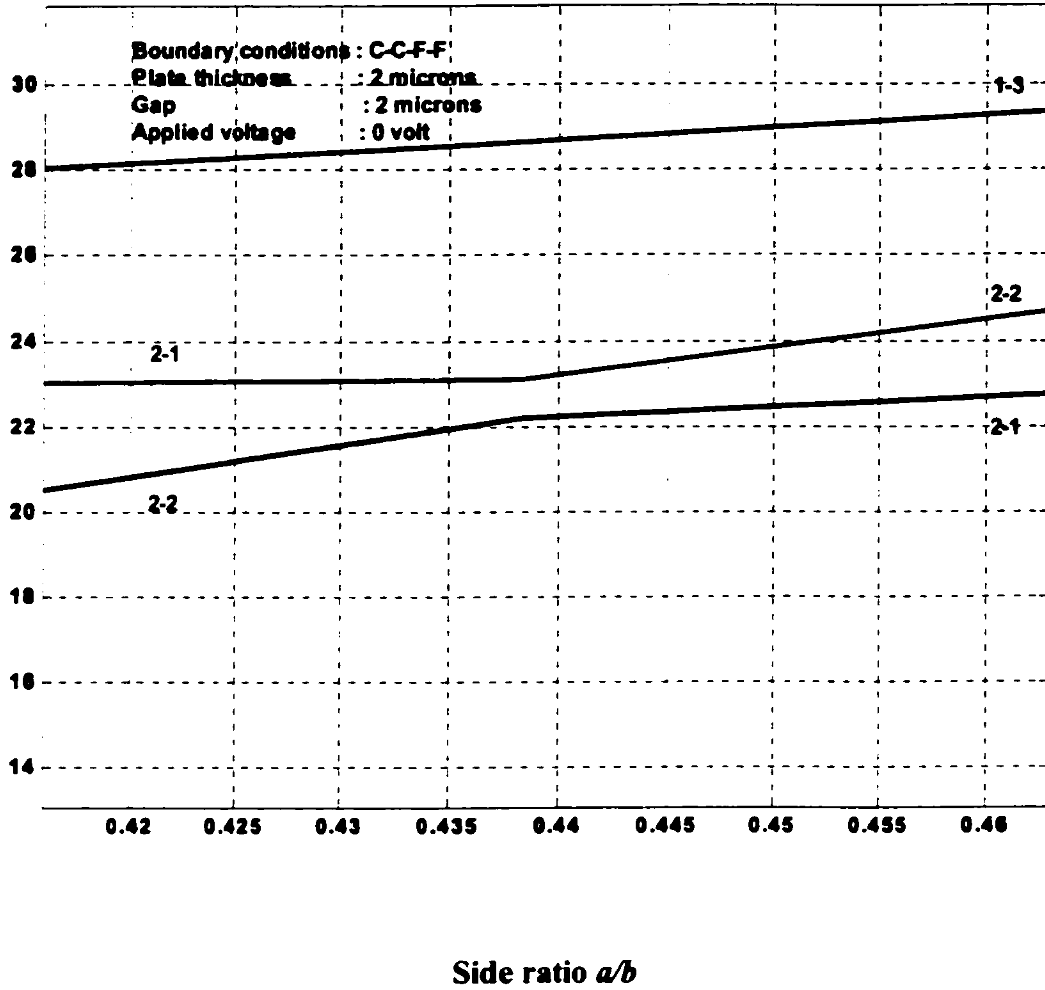

Side ratio *a/b*

Fig 4.5d Curve veering between modes 2-1 and 2-2 at a side ratio of 0.44

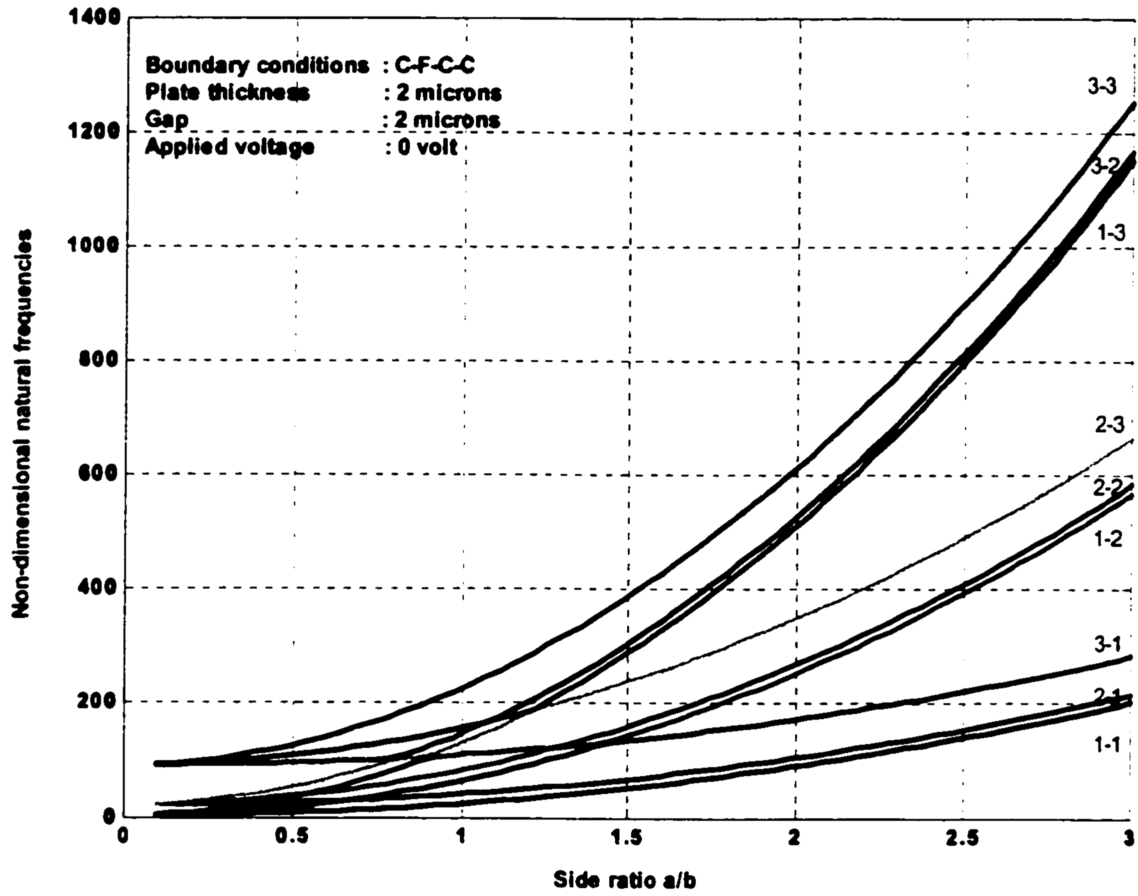

Fig. 4.6 Natural frequency versus side ratio for a C-F-C-C microplate

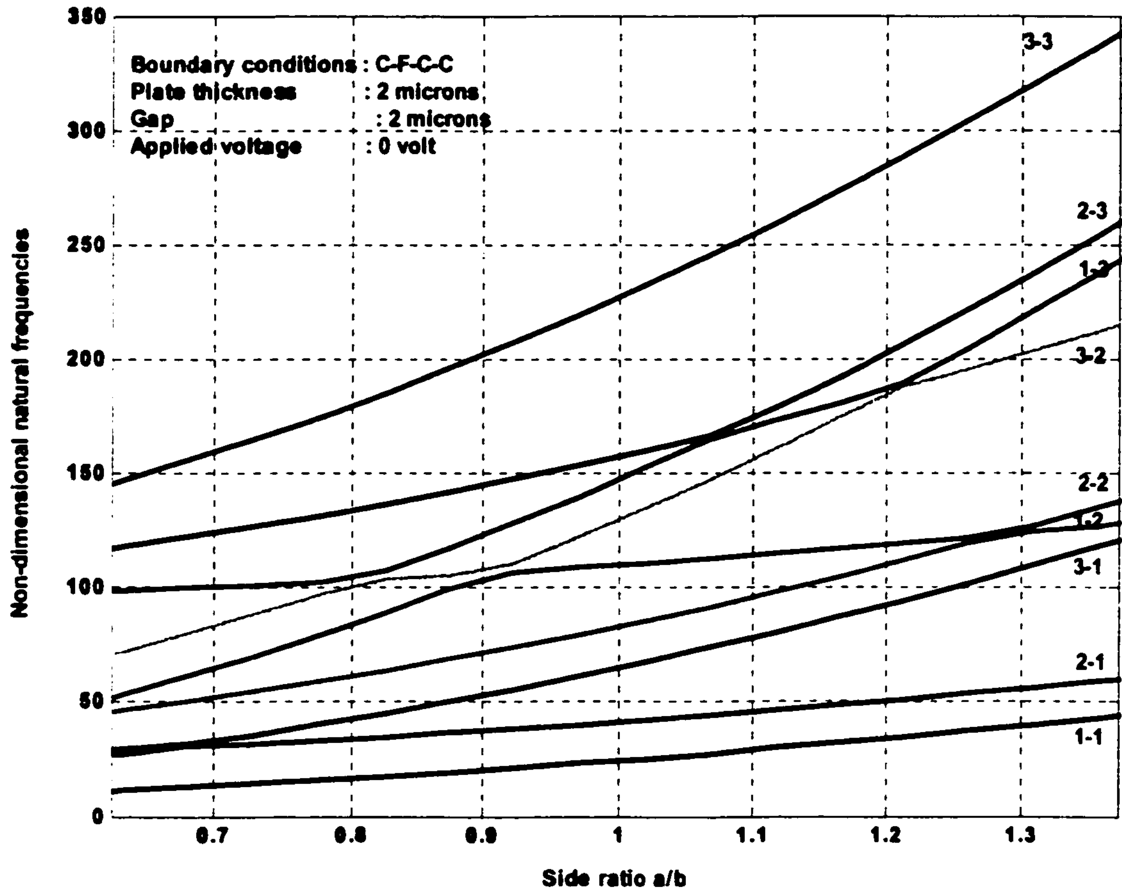

Fig. 4.6a Natural frequency versus side ratio showing curve veering

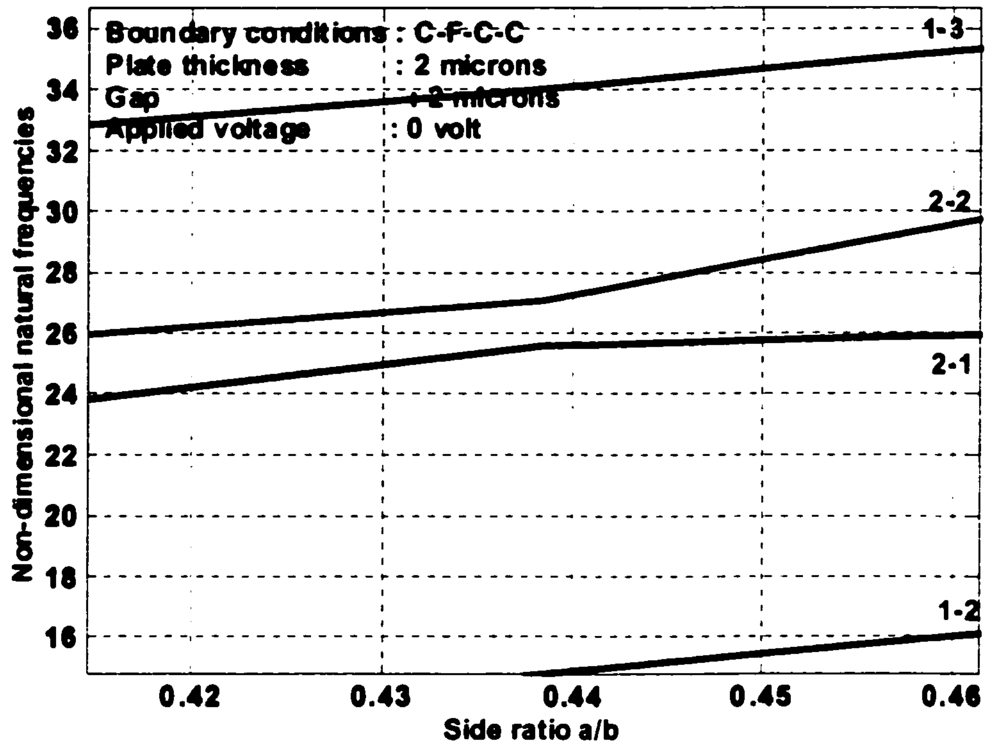

Fig. 4.6b Curve veering between modes 2-1 and 2-2 at a side ratio of 0.438

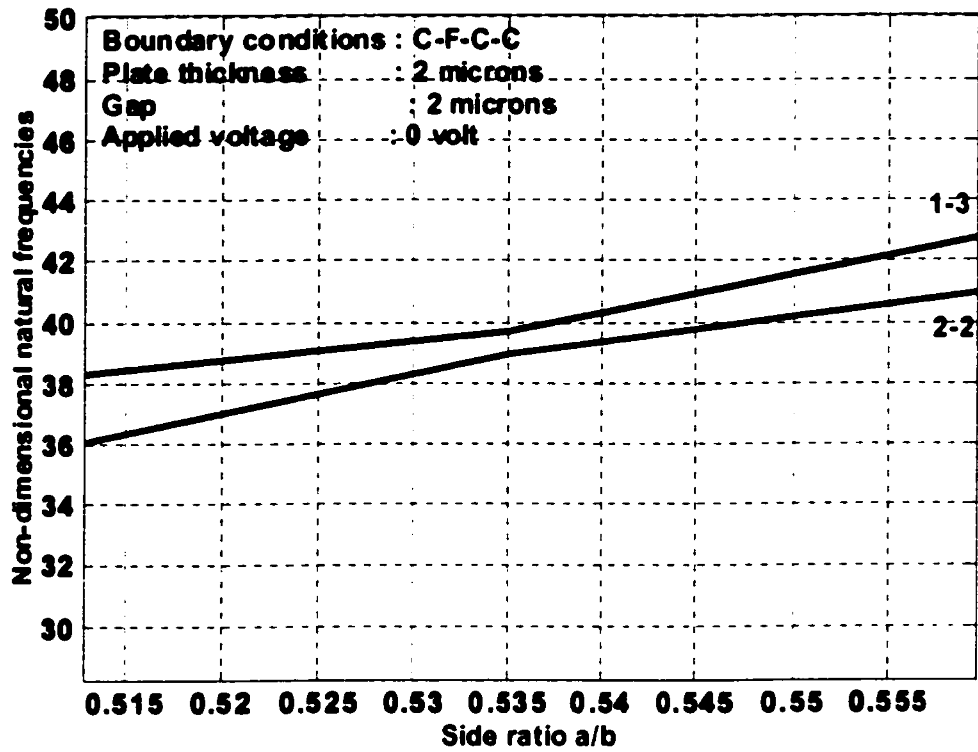

Fig. 4.6c Curve veering between modes 2-2 and 1-3 at a side ratio of 0.535

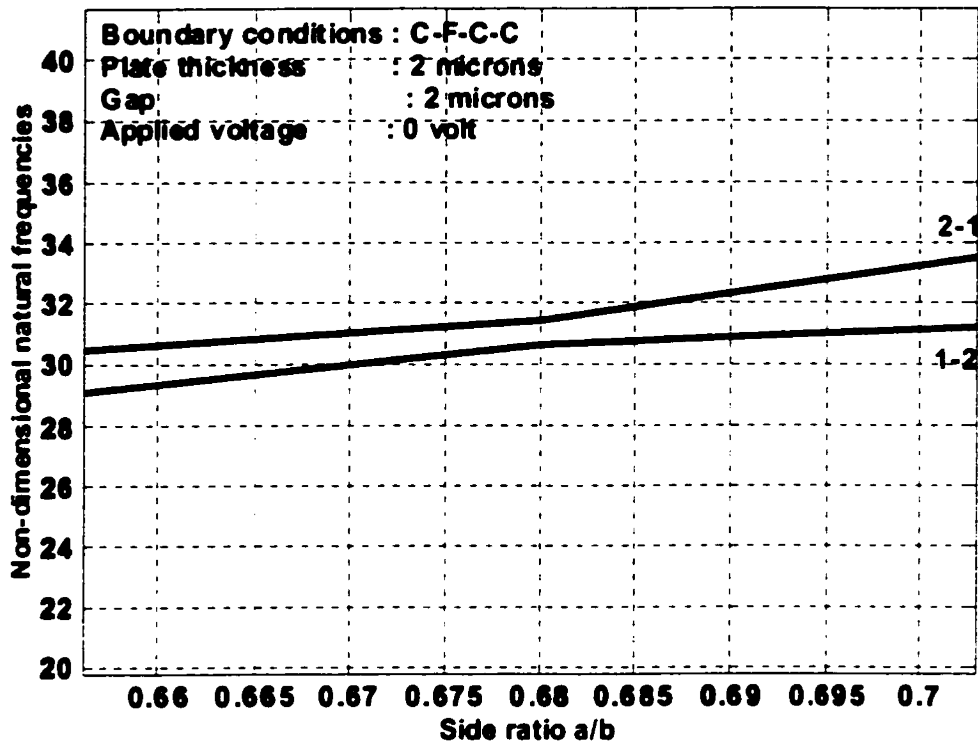

Fig 4.6d Curve veering between modes 1-2 and 2-1 at a side ratio of 0.68

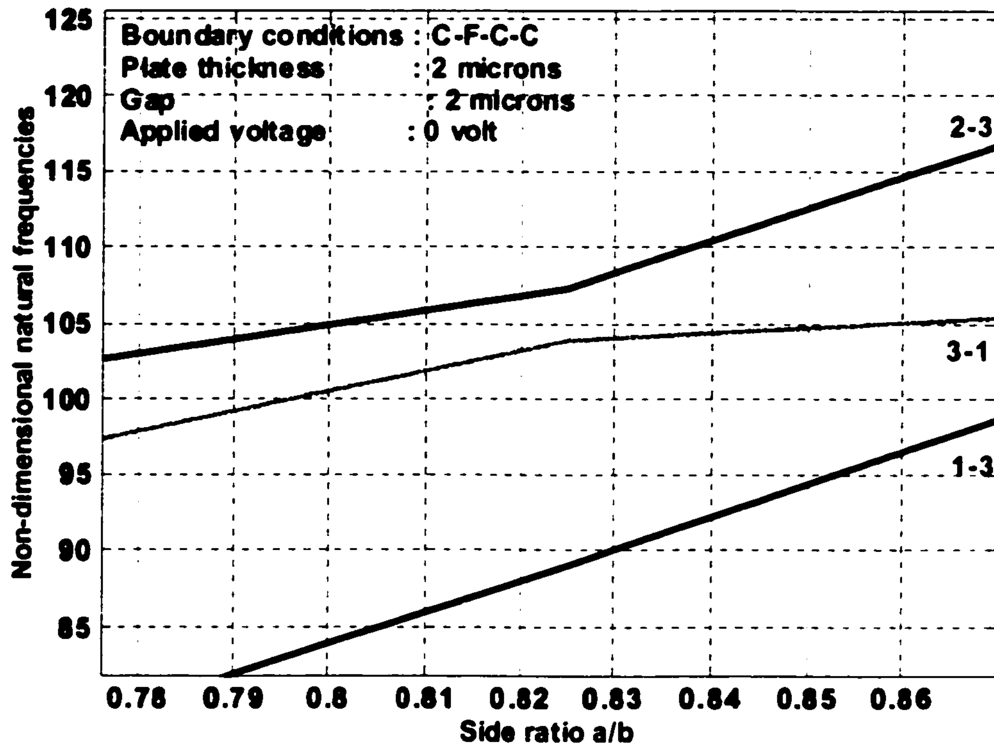

Fig 4.6e Curve veering between modes 3-1 and 2-3 at a side ratio of 0.825

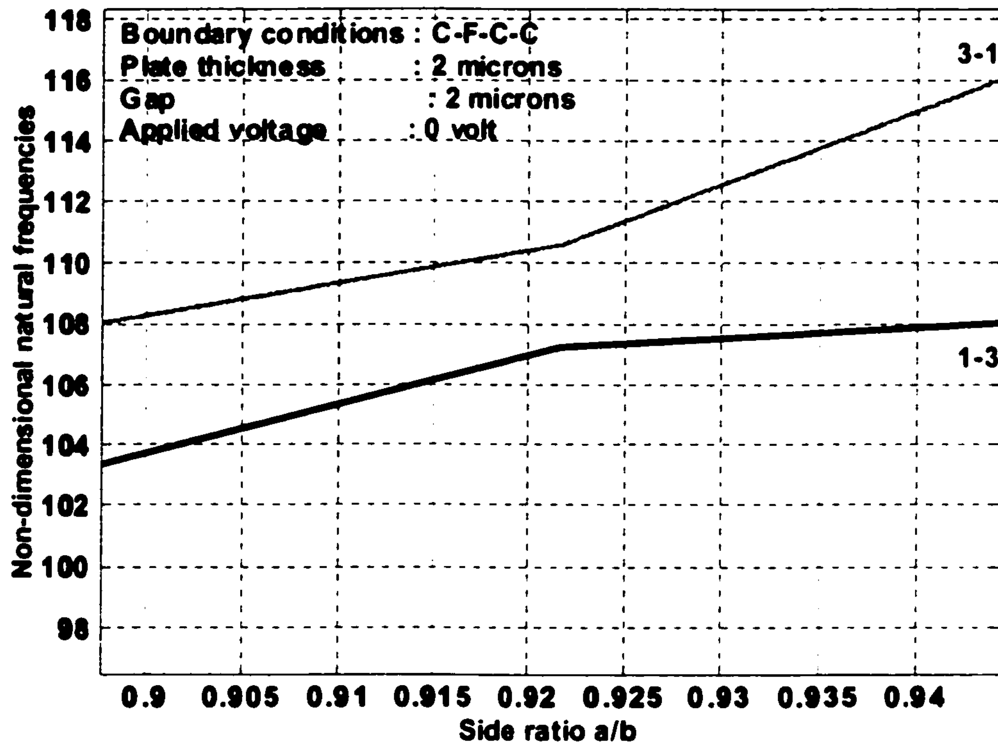

Fig 4.6f Curve veering between modes 1-3 and 3-1 at a side ratio of 0.922

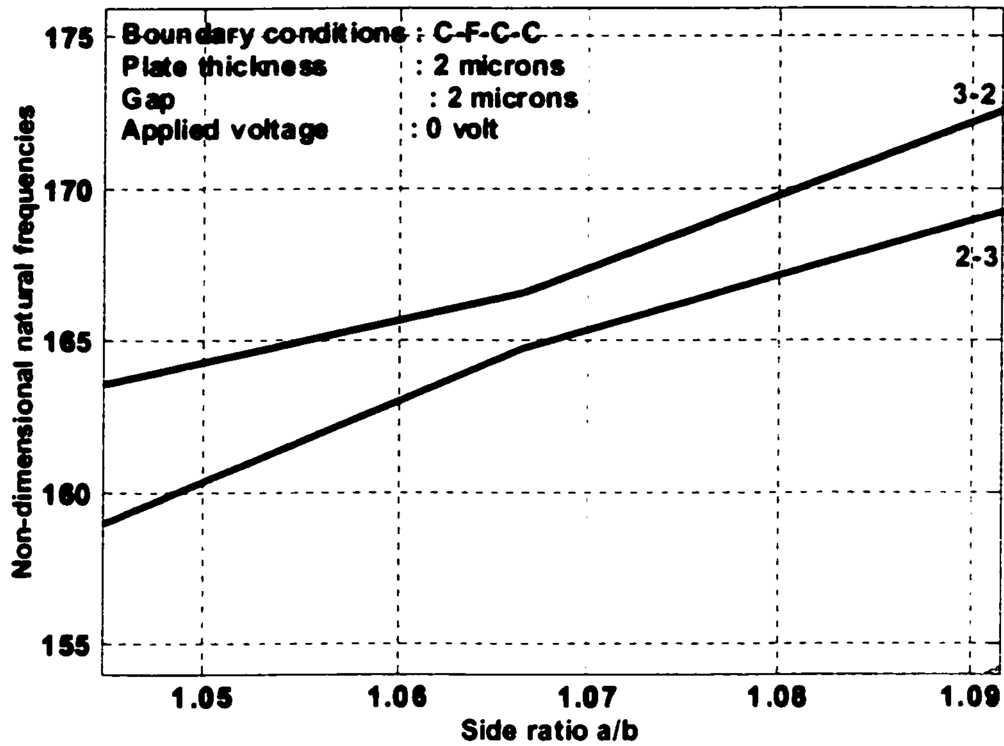

Fig 4.6g Curve veering between modes 2-3 and 3-2 at a side ratio of 1.067

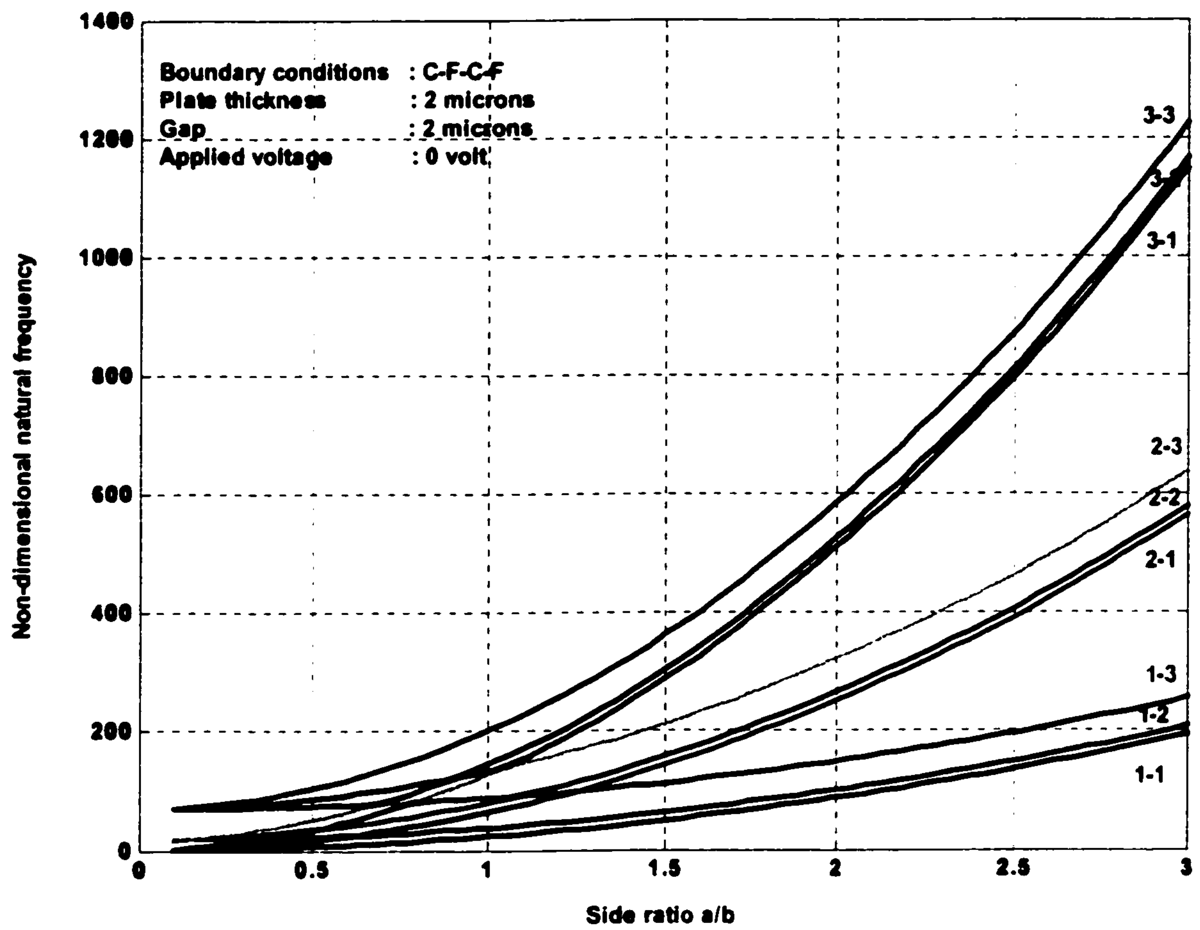

Fig. 4.7 Natural frequency versus side ratio for a C-F-C-F microplate

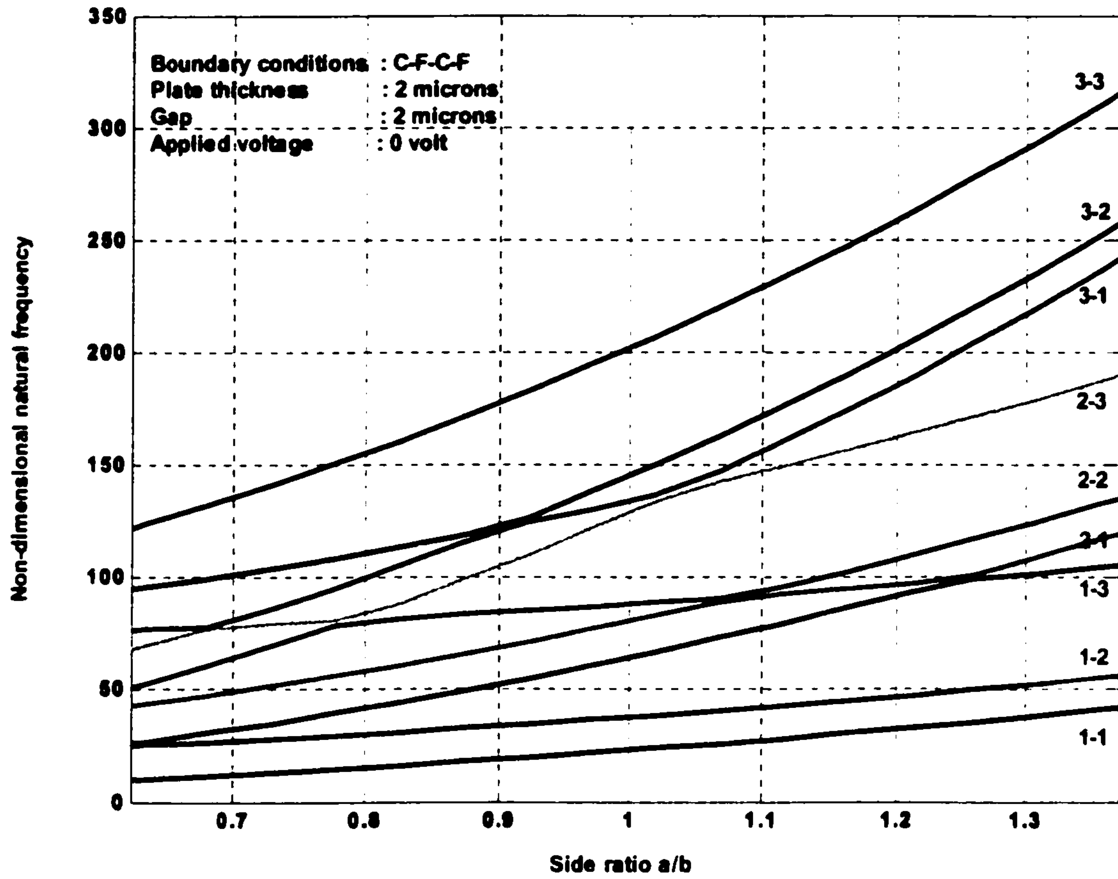

Fig. 4.7a Natural frequency versus side ratio showing curve veering

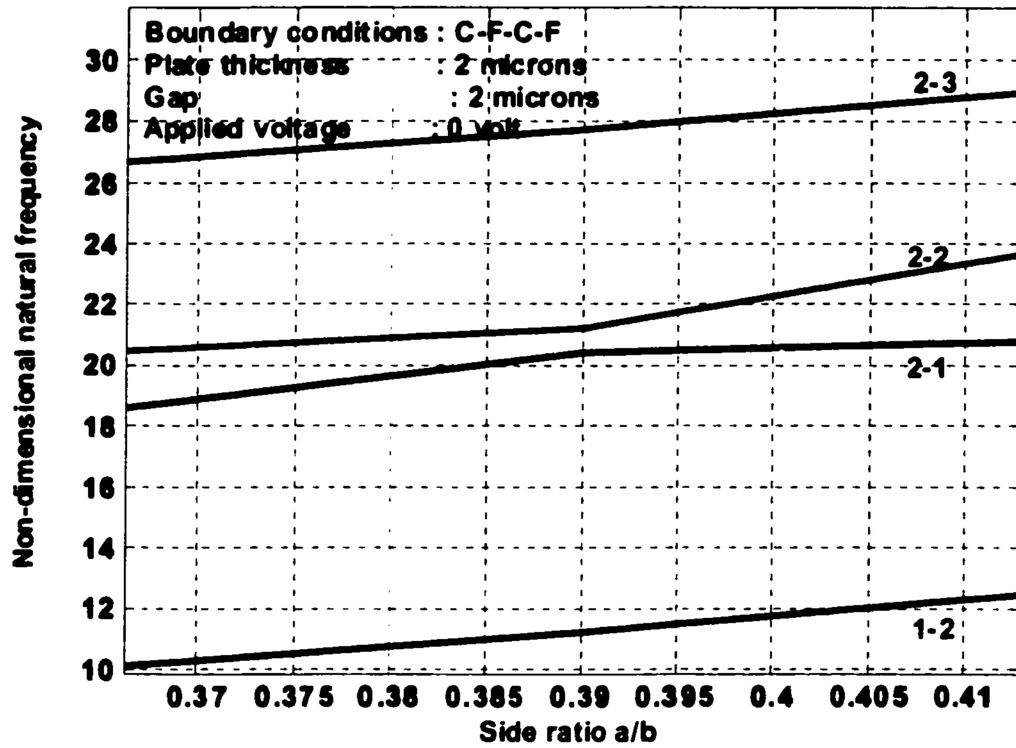

Fig 4.7b Curve veering between modes 2-1 and 2-2 at a side ratio of 0.39

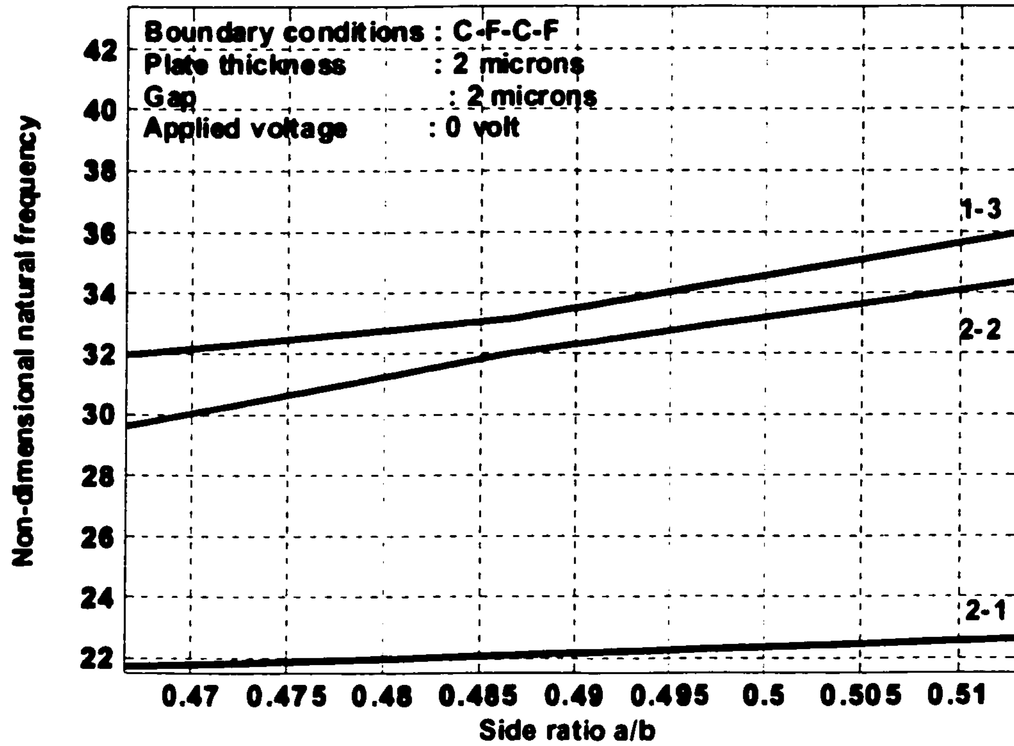

Fig. 4.7c Curve veering between modes 2-2 and 1-3 at a side ratio of 0.49

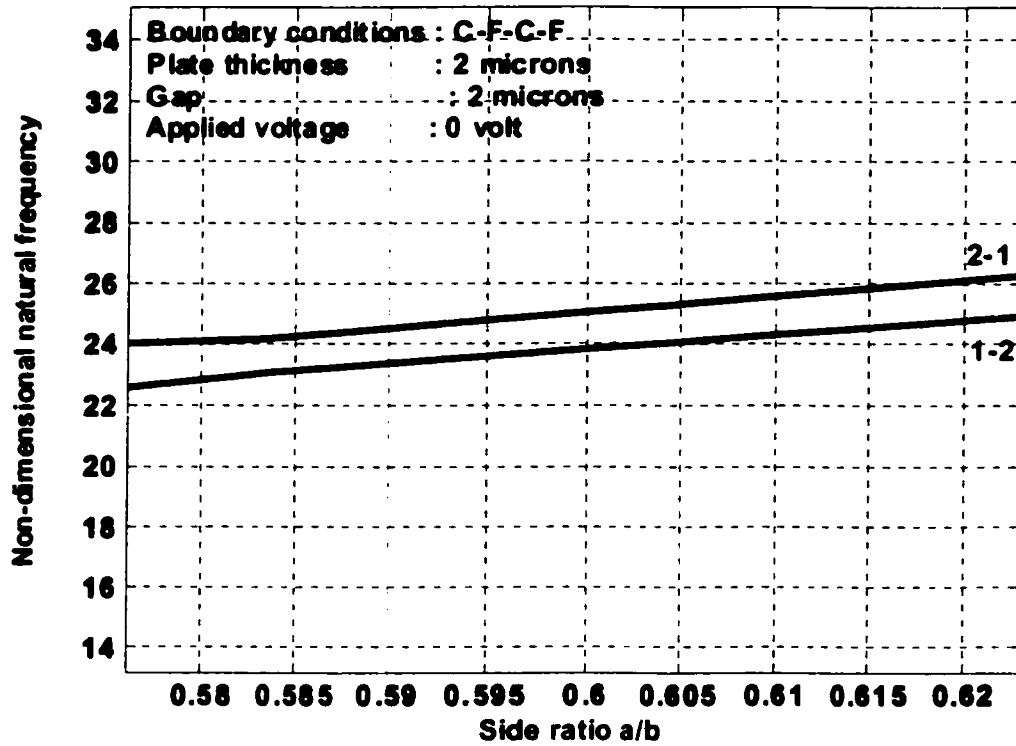

Fig. 4.7d Curve veering between modes 2-1 and 1-2 at a side ratio of 0.60

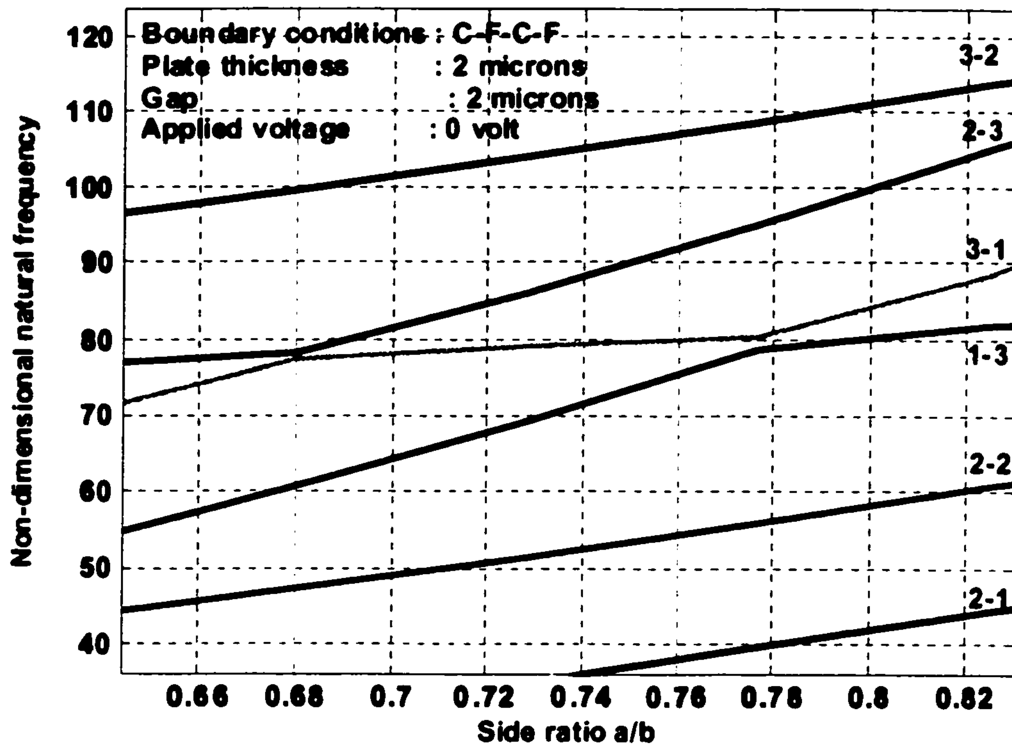

Fig. 4.7e Curve veering between modes 3-1 and 2-3 at a side ratio of 0.68, 1-3 and 3-1 at a side ratio of 0.776

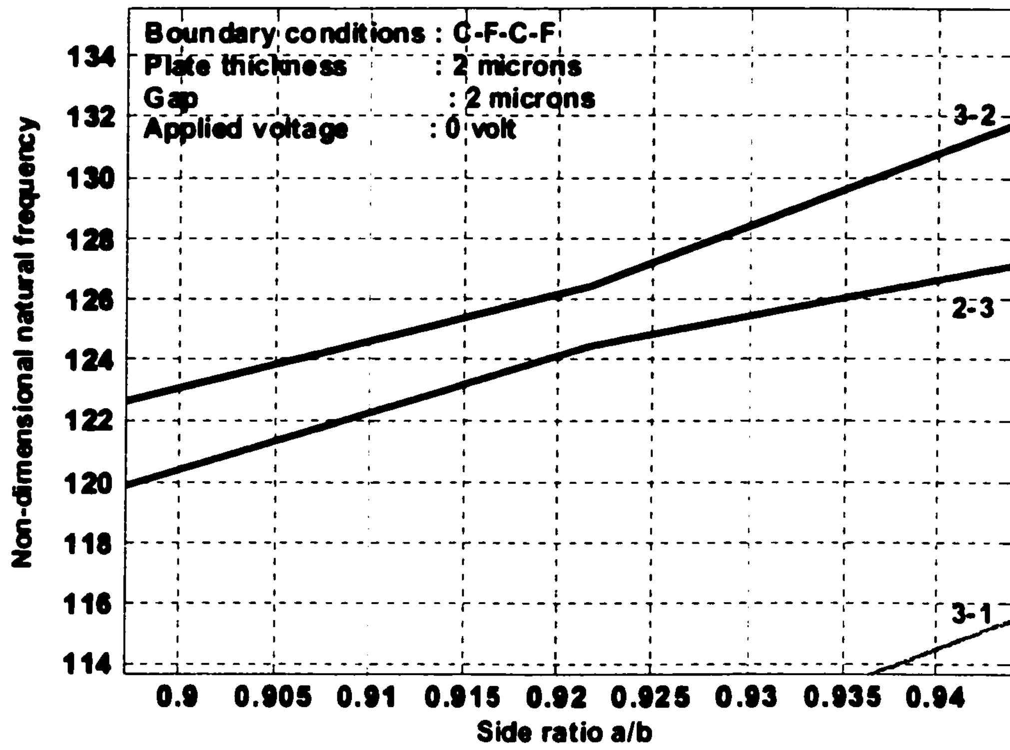

Fig. 4.7f Curve veering between modes 2-3 and 3-2 at a side ratio of 0.92

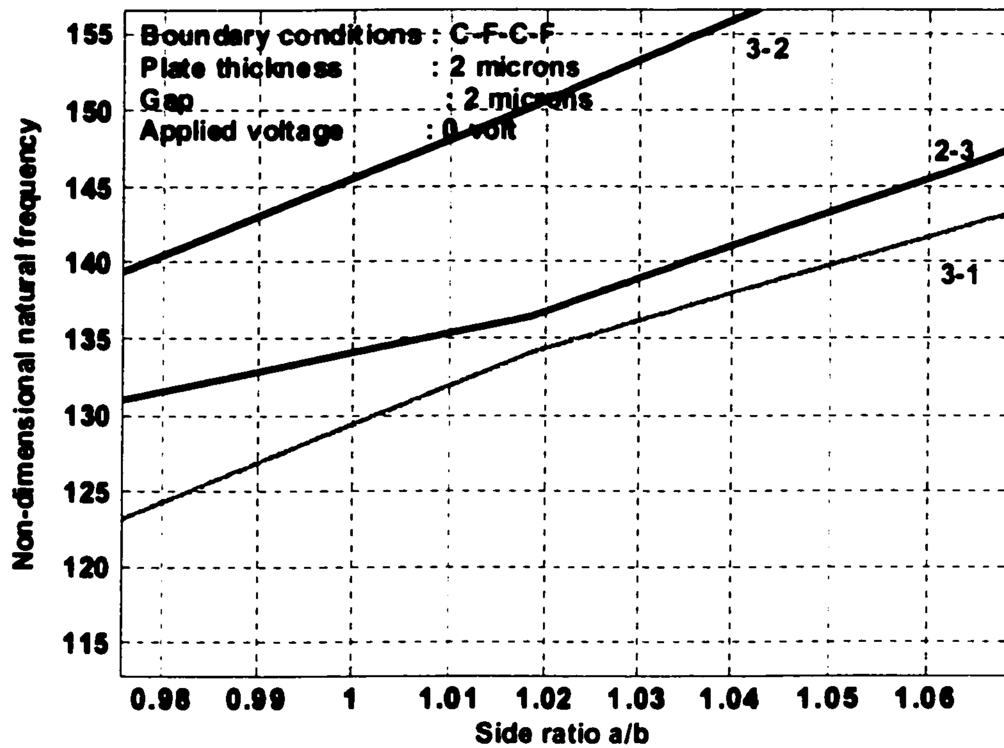

Fig. 4.7g Curve veering between modes 3-1 and 2-3 at a side ratio of 1.02

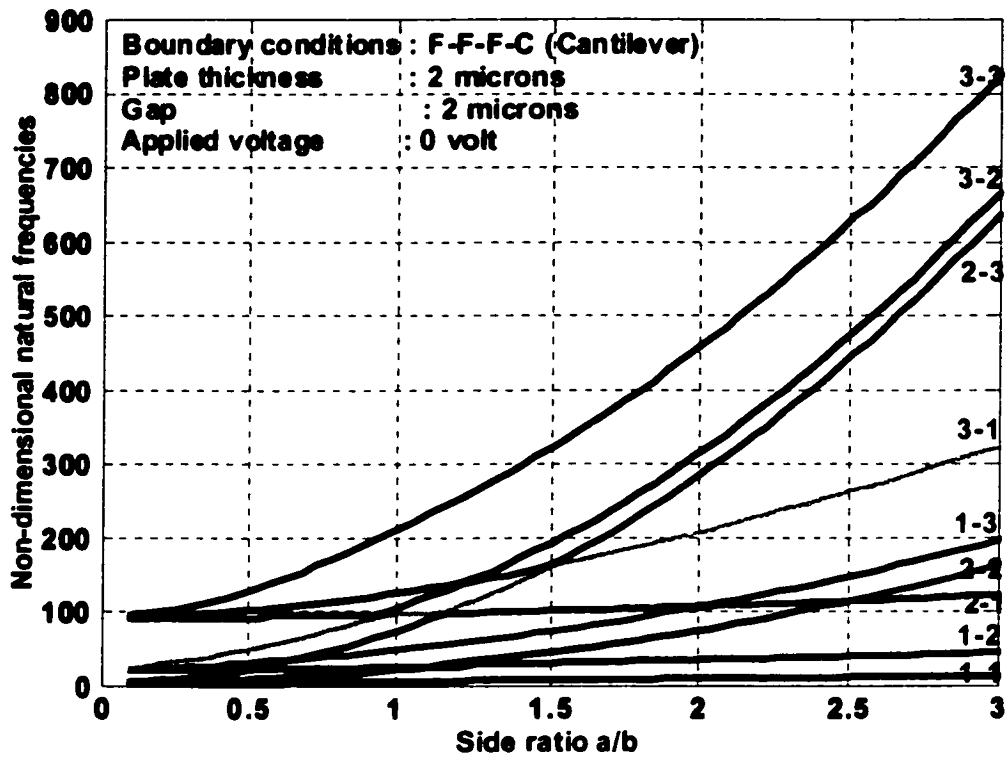

Fig. 4.8 Natural frequency versus side ratio for a cantilever (F-F-F-C) microplate

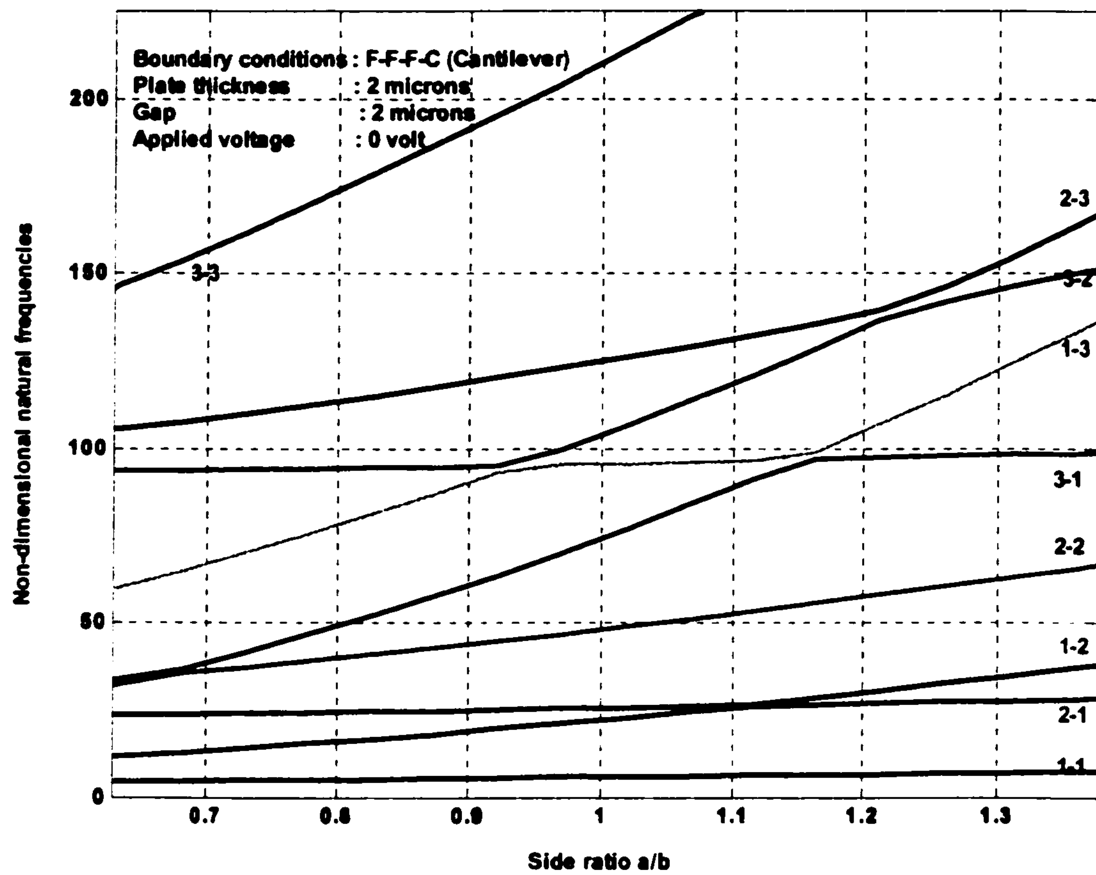

Fig. 4.8a Natural frequency versus side ratio showing curve veering

4.3 PARAMETRIC STUDY

Studies on capacitive microelectromechanical systems (MEMS) subject to electrostatic forces have been previously studied in the literature in connection with factors that result in *stiction* or the *pull-in* effect. Dagani et al (1998) obtained a polynomial equation used to determine the pull-in voltage and pull-in angle for an electrostatic torsion microactuator. Chan et al (1999) use pull-in voltage measurements to characterize contact electromechanics in the extraction of material properties. In the parametric study carried out by Nemirovsky and Bochobza-Degani (2001), the pull-in voltage, pull-in charge, and pull-in displacement are obtained using an algebraic equation referred to in their paper as the pull-in equation. In this paper the pull-in voltage is calculated for a parallel plate actuator, approximating its mechanical energy by a simple spring system even though a non-linear analysis is considered. Rajalingham and Bhat (1998) have obtained more accurate approximate solutions accounting for the non-linear nature of the capacitive microplate system given by Eq. (3.42) using an iterative scheme in which the Casimir force was ignored.

To the best of our knowledge, consideration has not been given to the influence of the side ratio on the stability of capacitive microelectromechanical systems such as the microplate structures designed in this thesis. Furthermore, the effect of various boundary conditions on the pull-in voltage for microplates designed in the MUMPs process has not been previously reported in the literature and is presented here.

In the design of capacitive MEMS components it may be desirable to have boundary conditions other than C-C-C-C and geometries not limited to square structures. Hence the need to consider the effect a change in boundary conditions and plate side dimensions is necessary to effectively predict the response and performance of the device, avoiding the occurrence of stiction.

The pull-in voltage that results in stiction is obtained from the present analysis using 3 orthogonal polynomials in each beam direction, as approximate deflection functions in the Rayleigh-Ritz method. The results of the method used in this thesis are presented in Fig. 4.9, which shows the variation of non-dimensional natural frequencies, γ of the first 9 modes with the non-dimensional voltage β. As reported by Rajalingham and Bhat (1998) and Nemirovsky and Bochobza-Degani (2001), an increase in the non-dimensional voltage results in a decrease in the non-dimensional natural frequency, which is similarly obtained here. Zero values of β indicate instability due to stiction, at a corresponding value of γ. The aforementioned papers considered the variation for the fundamental mode of vibration at fixed dimensions. In this thesis, consideration is given to other vibration modes at various side ratios.

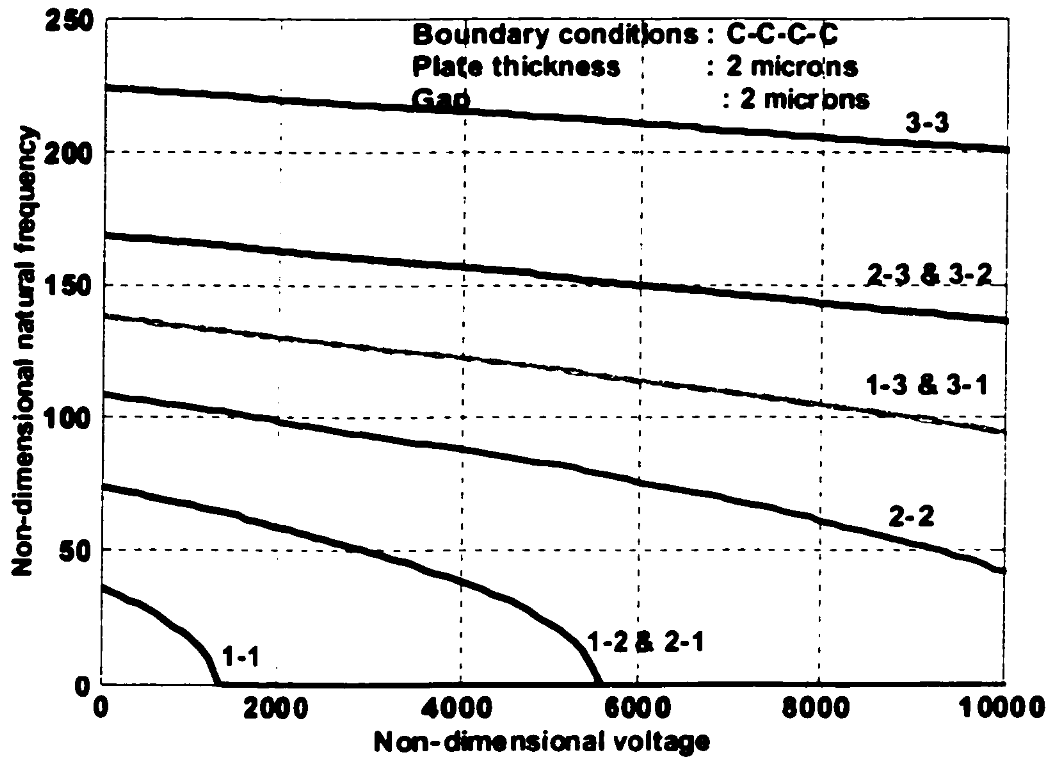

Fig. 4.9 Natural frequency versus voltage for various modes of vibration for a C-C-C-C plate

Figs. 4.10, 4.11 and 4.12 show results of non-dimensional frequency variation with the side ratio for applied voltages of 70, 80 and 90 volts, respectively for a C-C-C-C plate. As mentioned earlier, the side ratio a/b used in these computations are based on a fixed value of the width, b equal to 300 μm. Specifically for the thickness and gap dimensions constrained by the MUMPs process, there is an onset of instability in the fundamental mode of vibration at a side ratio a/b in excess of 3.0, for an application of 80 volts. In this range the system becomes unstable as a result of the voltage pull-in effect or stiction; a sticking together of the parallel plates. This occurs due to the fact that the elastic restoring force of the plate given by Eq. 3.39 is not able to overcome the negative forces of attraction induced by the electrostatic forces and the Casimir effect as considered here. These field forces are stated in Eqs. 3.40 and 3.41 respectively. For the given plate dimensions, the result is a cessation of vibration. With an application of 90 volts for example, to the microplate, we see that stiction would occur at a *pull-in side ratio*, the side ratio at which stiction occurs, of 1.65 for this square C-C-C-C microplate (Fig. 4.11). Conversely, all values of side ratio less than 1.65 with an application of 90 volts would not result in the stiction phenomenon occurring due to electrostatic or Casimir effects. Fig. 4.13 shows the variation of the fundamental non-dimensional natural frequency, γ with the non-dimensional voltage, β for a C-C-C-C microplate at various side ratios. It can be clearly be seen that as the side ratio increases, β increases up to a certain limit constrained by the *pull-in side ratio*. From Eq. 3.78d, the square of the voltage is inversely proportional to the fourth power of the side dimension, a. As the side dimensions of the microplate tend to that for a beam there is a tendency for stiction to occur. It can therefore be concluded that the side ratio is an important criterion to

consider in the design of capacitive MEMS in order to avoid the undesirable occurrence of stiction due to these field effects.

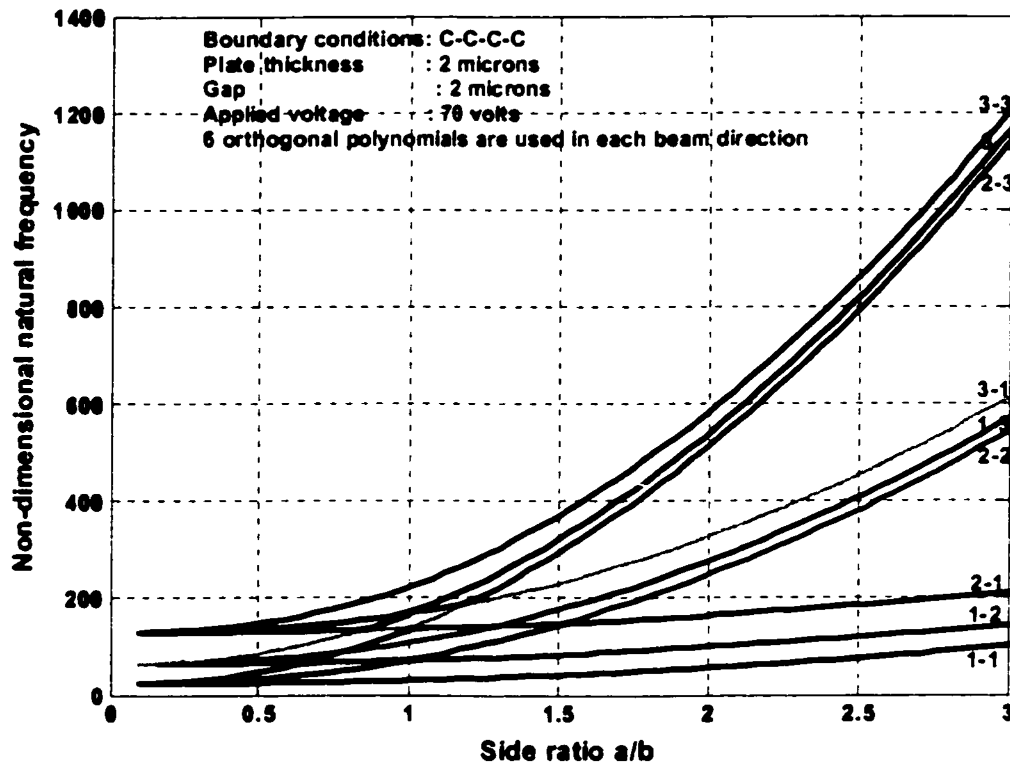

Fig. 4.10 **Natural frequency showing regions of instability for an applied voltage of 70 volts**

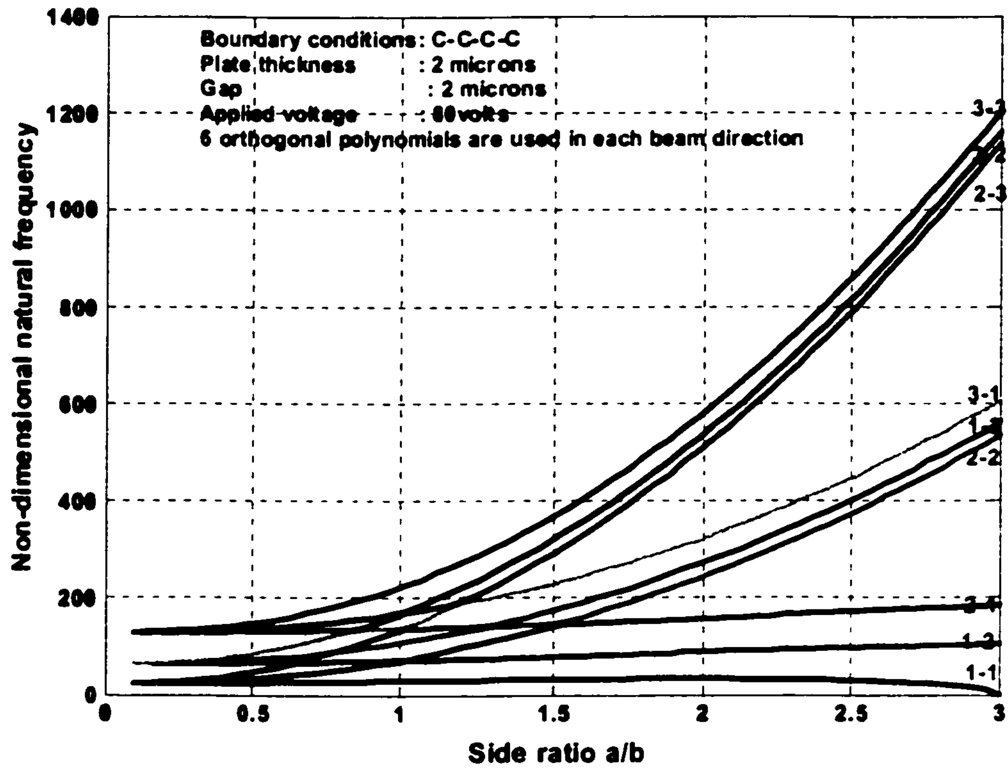

Fig. 4.11 Natural frequency showing instability for an applied voltage of 80 volts

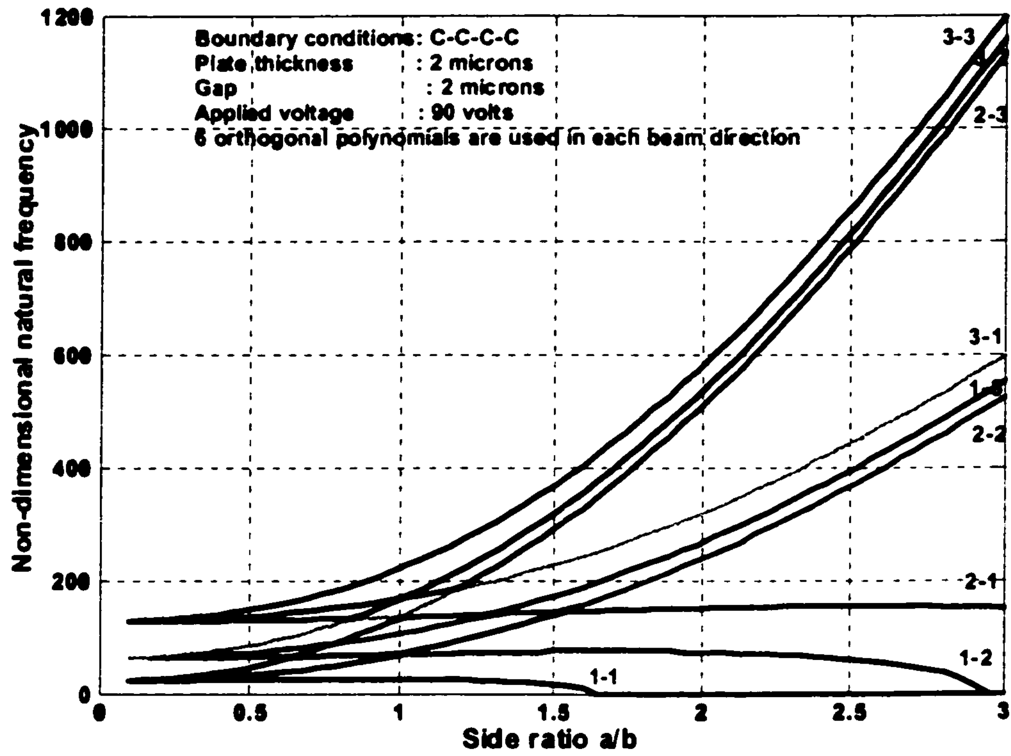

Fig. 4.12 **Natural frequency showing instability for an applied voltage of 90 volts**

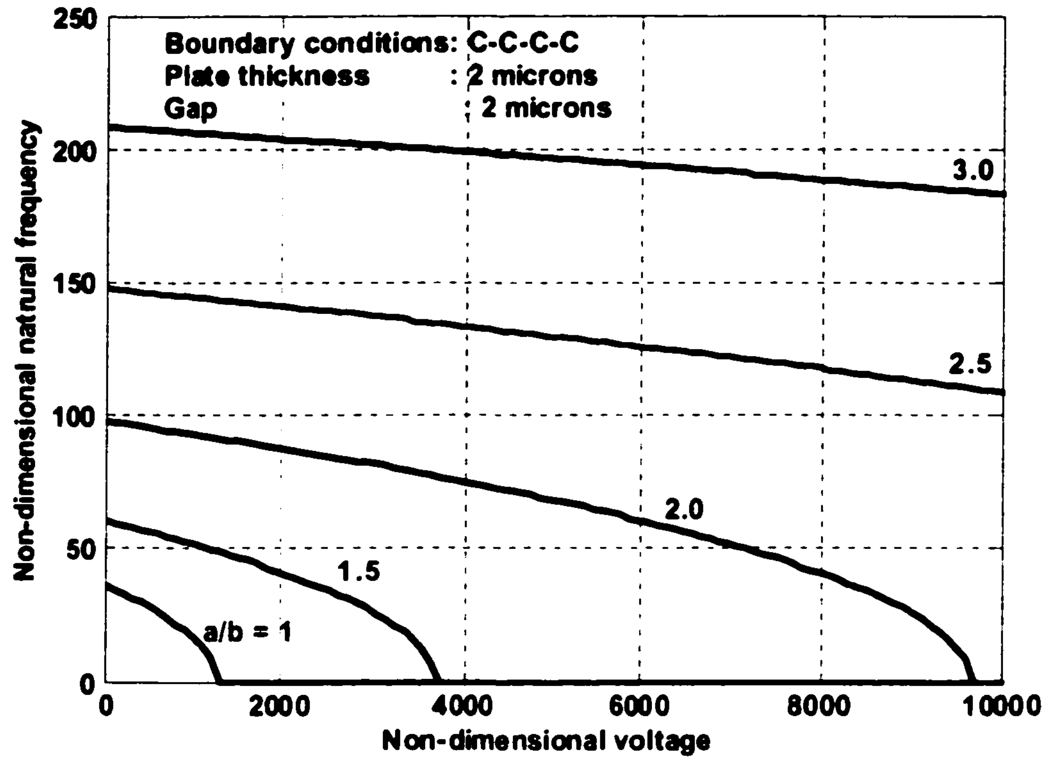

Fig. 4.13 **Natural frequency versus voltage for various side ratios on a C-C-C-C plate**

As mentioned earlier, it may be desirable in the design of capacitive MEMS components to have boundary conditions other than C-C-C-C and geometries not limited to square structures. The results for the influence of voltage on the plate natural frequencies are shown in non-dimensional form for the first 9 modes of vibration. Further results give illustrate the influence the side ratio has on the non-dimensional natural frequency at a given non-dimensional voltage. These results are presented for various boundary conditions represented by C-F-C-C, C-F-C-F, C-C-F-F, and F-F-F-C (cantilever) and are shown in Figs 4.14, 4.15, 4.16, and 4.17 respectively.

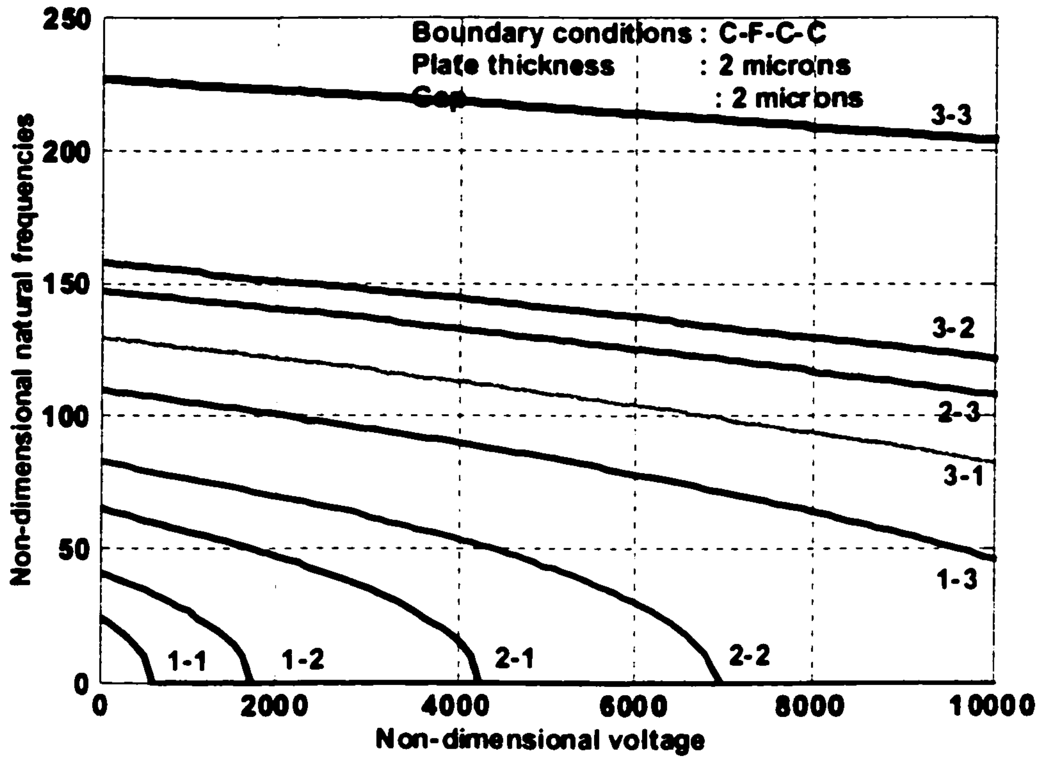

Fig. 4.14a Natural frequency versus voltage for various modes of vibration for a C-F-C-C microplate

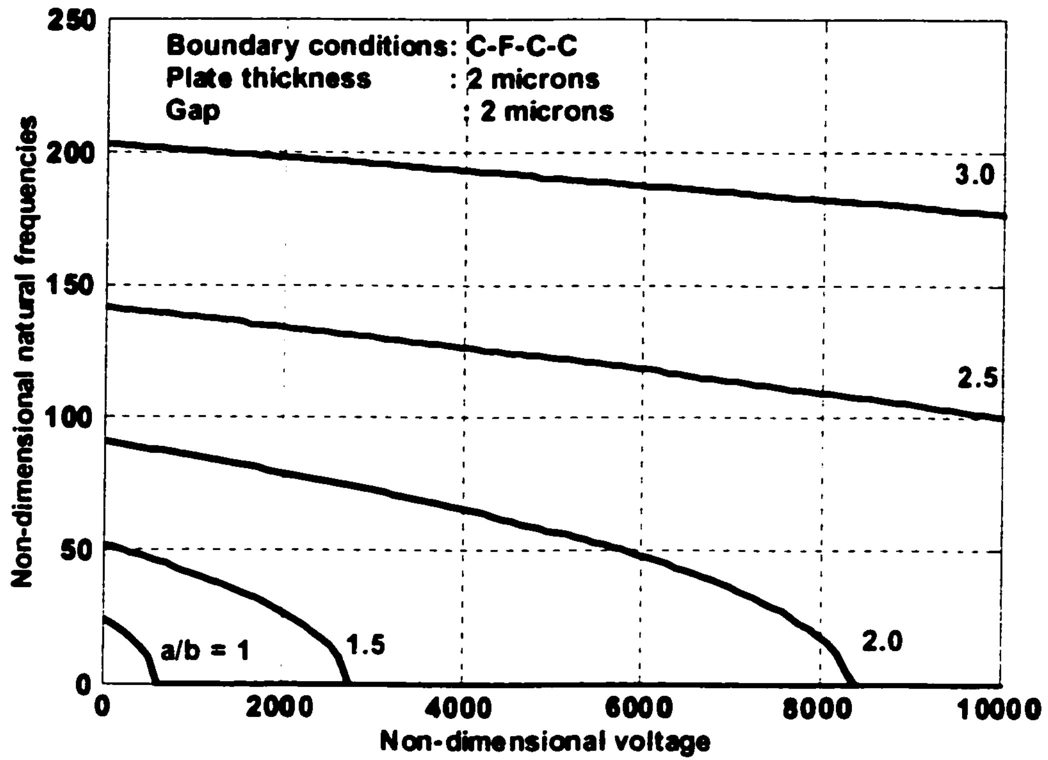

Fig. 4.14b Natural frequency versus voltage for various side ratios on a C-F-C-C microplate

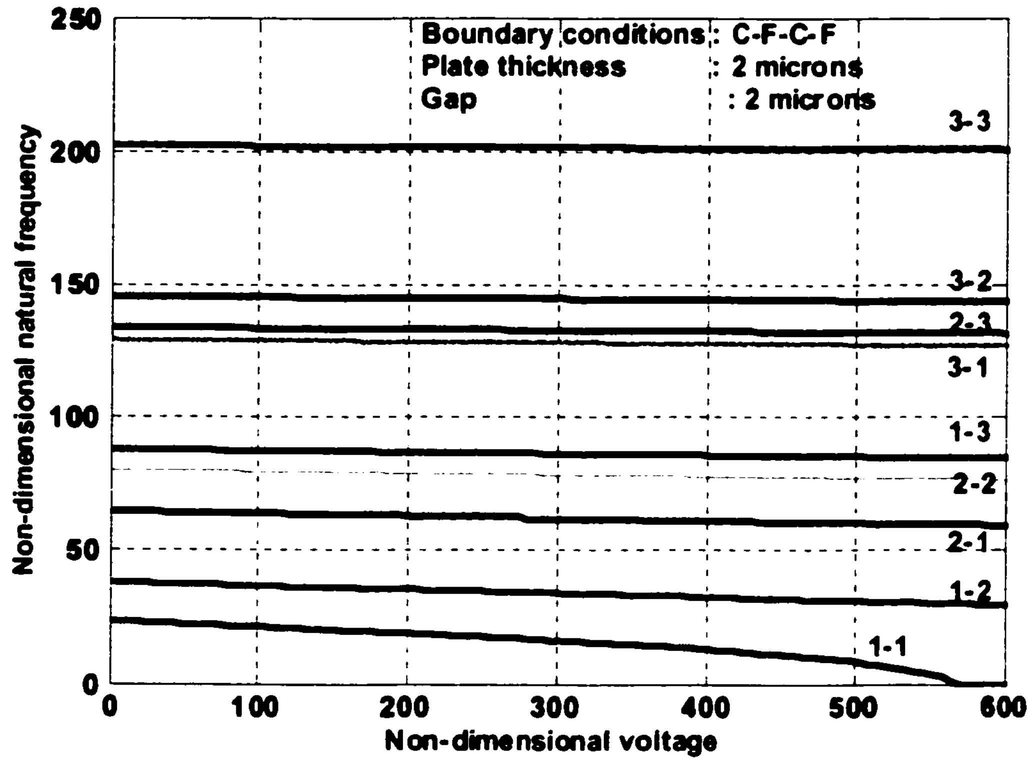

Fig. 4.15a Natural frequency versus voltage for various modes of vibration for a C-F-C-F microplate

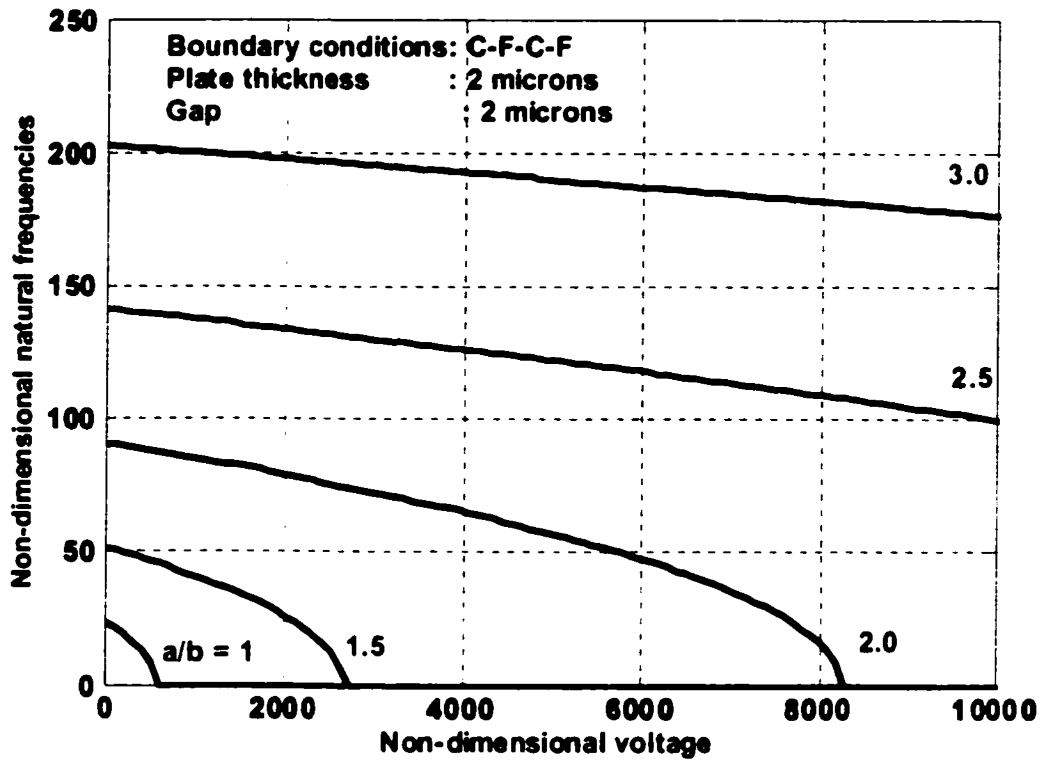

Fig. 4.15b Natural frequency versus voltage for various side ratios on a C-F-C-F microplate

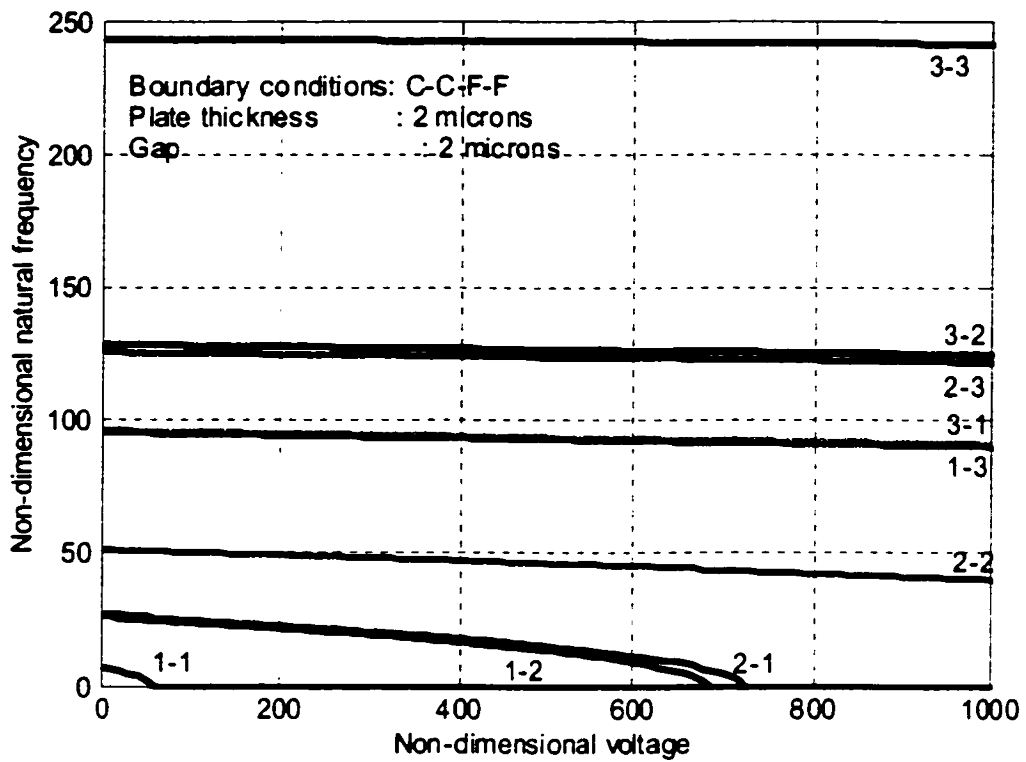

Fig. 4.16a Natural frequency versus voltage for various modes of vibration for a C-C-F-F plate

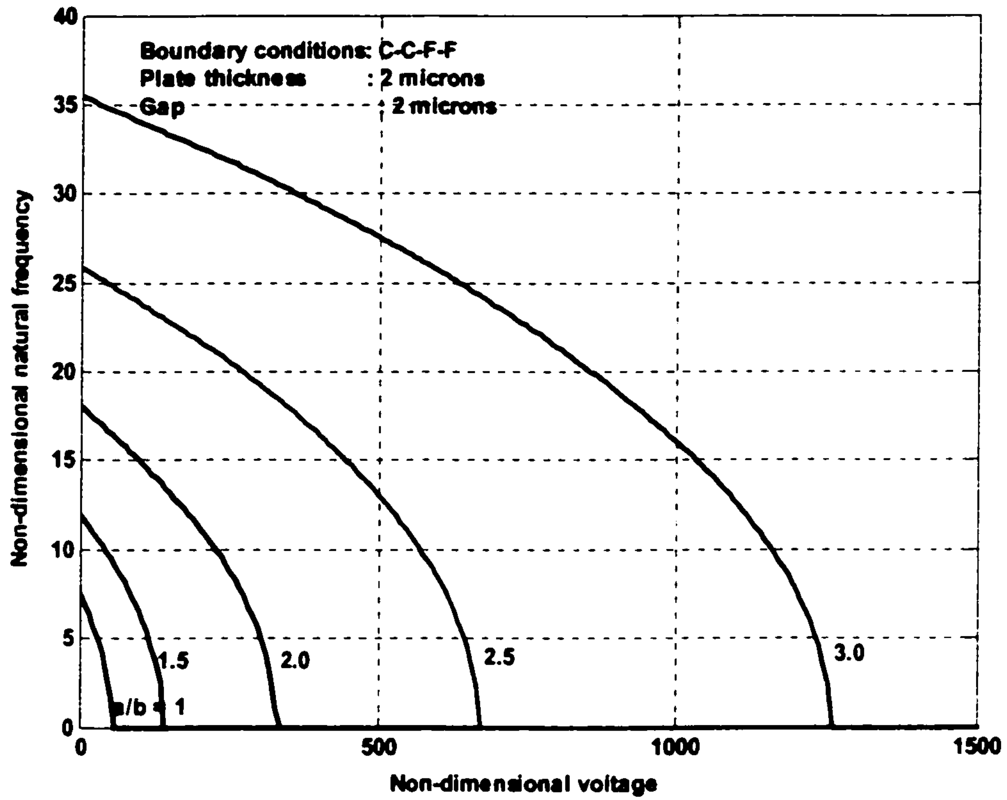

Fig. 4.16b Natural frequency versus voltage for various side ratios on a C-C-F-F plate

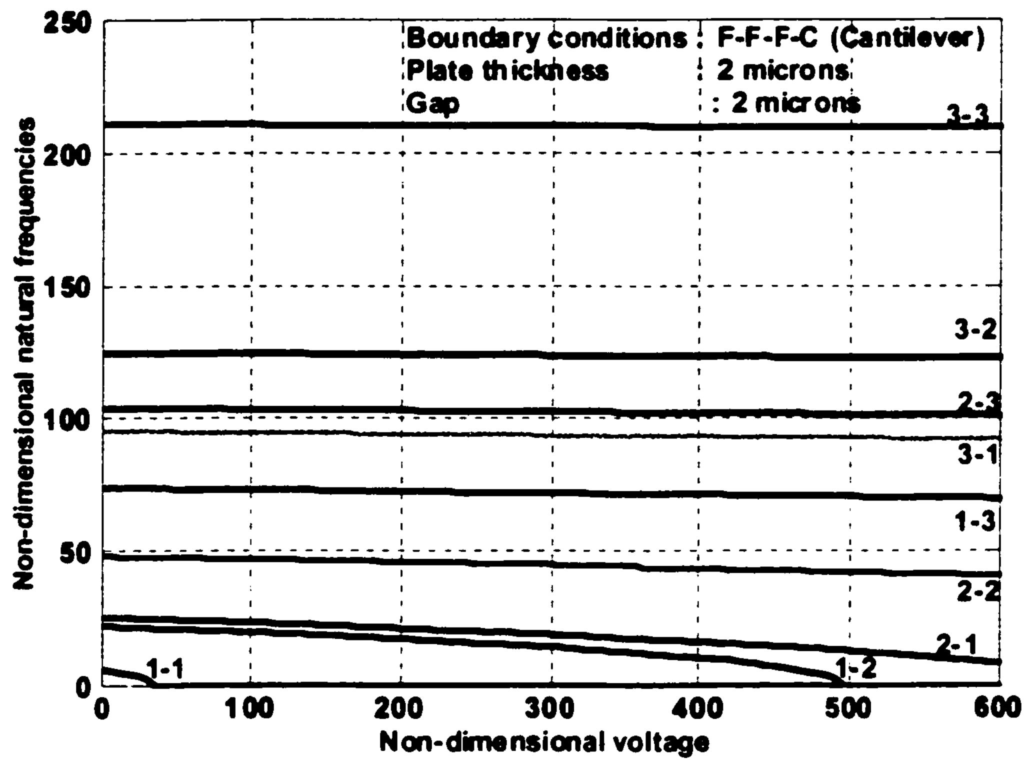

Fig. 4.17a Natural frequency versus voltage for various modes of vibration for a F-F-F-C microplate

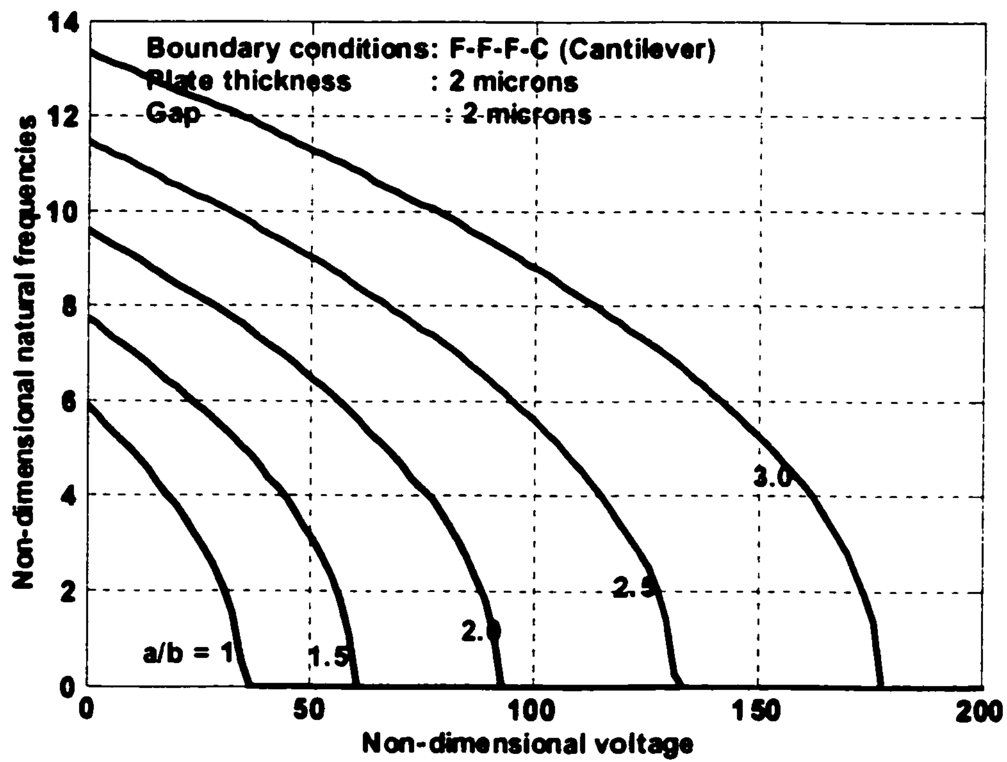

Fig. 4.17b Natural frequency versus voltage for various side ratios on a F-F-F-C microplate

From the foregoing results, it is seen that for a given side dimension, the C-C-C-C microplate has the greatest elastic restoring force capable of withstanding the field forces that induce stiction. Conversely, the cantilever plate of the same dimensions has the least. This is evident from a comparison of Figs 4.13 and 4.17b. Take for example a microplate with a side ratio of 1.5. The plate dimensions are 450 μm x 300 μm. The C-C-C-C plate will become unstable at a non-dimensional voltage of 3737.37 whereas the cantilever plate becomes unstable at 60.60. From Eq. 3.78d the maximum voltage that can be applied to the C-C-C-C microplate is 96.68 volts. The corresponding value for the cantilever plate at this side ratio is 11.93 volts, which is only about 12 % of that for the C-C-C-C plate. This may be advantageous or not, depending on the objective of the design. Similar computations may be made for other combinations of side ratio and boundary conditions that commonly occur in the design process of capacitive MEMS. As another example, consider the C-C-C-C plate at a side ratio of 1 (a square plate) and a side ratio of 2.0. From Fig. 4.13 the non-dimensional *pull-in* voltages are given as 1313.13 and 9696.96. The voltages are calculated from Eq. 3.78d as 124.98 volts and 84.88 volts respectively, showing a decrease in *pull-in* voltage as the side ratio is increased. Similarly, at side ratios of 1.0 and 2.0 for the cantilever plate, the non-dimensional *pull-in* voltages are given from Figs. 4.17b as 36.36 and 92.92, and the *pull-in* voltages are 20.79 volts and 8.31 volts respectively.

The design implications are very instructive. In the usual trade-offs inherent in the design process, engineers and scientists would do well to dimension their capacitive MEMS devices in a way that will avoid impairment of its function through stiction

effects resulting from a side ratio that causes instability for a given set of geometric boundary conditions.

The foregoing analysis and results indicate that in the design of capacitive microelectromechanical systems, engineers and scientists should consider not only the applied voltage and gap for determining the pull-in voltage and pull-in displacement as obtained by Nemirovsky and Bochobza-Degani (2001) and Rajalingham and Bhat (1998). Consideration should also be given to the *pull-in side ratio* as determined here for a given gap and voltage. The nature of the boundary conditions also has a significant influence on the pull-in parameters and must be taken into account. A microplate clamped on all four sides, C-C-C-C has a much higher pull-in voltage for a given set of dimensions than a cantilever microplate. Similarly, a C-C-C-C microplate will tolerate higher side ratios for a given voltage prior to the onset of instability for a given geometric configuration on the boundaries of the device.

Consequently the variation of plate side dimensions necessitated by device function has to be limited by the prospect of instability resulting from the proportions of the side dimensions and the nature of its boundary conditions. These results can be exploited in the MEMS design process to achieve specific desired functions, sensitivity and operational performance of a given device in a reduced design cycle time.

CHAPTER 5

CONCLUSIONS AND RECOMMENDATIONS FOR FURTHER WORK

5.1 CONCLUSIONS

The response of a capacitive microelectromechanical system (MEMS) subject to field effects arising from electrostatic and Casimir forces has been studied from the point of view of curve veering. The influence of the applied voltage and side ratio on the natural frequencies of the plate having various boundary conditions has also been investigated.

The system was modeled as a pair of parallel conductive plates designed in the Multi-User MEMS Processes (MUMPs) technology. The plate considered is a typical structural element of a capacitive MEMS device that finds application in sensors, actuators and switches. A mathematical model describing the complete effect of these forces on a pair of parallel conductive plates was developed resulting in a mixed domain type model. The response of the system from the point of view of curve veering was subsequently obtained from a solution of the resulting governing non-linear equations using a suitable approximate technique, the Rayleigh-Ritz method. The analysis is carried out using boundary characteristic orthogonal polynomials in the Rayleigh-Ritz method to obtain the natural frequencies for a given set of system parameters. The natural frequencies of a microplate subjected to the field effects considered in this thesis were obtained and the curve veering behavior for this system was examined. The effect of various boundary

conditions of the microplate on curve veering was considered. The non-dimensional natural frequencies are plotted against the side ratio.

Results are obtained using 6 orthogonal polynomials as shape functions in the Rayleigh-Ritz method of analysis. A parametric study of the influence of various parameters on the behavior of the system was presented. Consideration is given to such relations as the influence of the gap between plates, voltage, plate side dimensions, as well as type of boundary conditions and the contributing effect of the electrostatic and Casimir forces on the natural frequency of vibration of the micro plate.

From the results presented, the following conclusions have been reached:

- The plate is unstable at certain voltage and plate parameter combinations

- At a given voltage for which the plate is stable, the curve veering phenomenon occurs at several locations of side ratio between Φ_{ij} and Φ_{ji} modes of vibration. For plates that are geometrically symmetric and have symmetric boundary conditions about a diagonal axis (having a positive slope), curve veering occurs for all the Φ_{ij} and Φ_{ji} modes at a side ratio of 1.0. This is the case for the microplate clamped on all 4 sides (C-C-C-C) and that clamped on two adjacent sides and free on the other 2 (C-C-F-F), which have veering between the 1-2/2-1, 1-3/3-1 and 2-3/3-2 modes, respectively. Those with asymmetrical boundary conditions about a diagonal axis (having a positive slope) do not have curve veering occurring at a side ratio of 1, but at other locations along in the side ratio domain. This is applicable to the plates clamped on 3

sides and free on 1 (C-F-C-C), clamped on 2 opposite sides and free on the other 2 (C-F-C-F), and a cantilever plate, respectively.

- Results obtained from standard tools using approximate method of analysis should be used with understanding and caution in frequency response problems as the phenomenon of curve veering may give misleading results at certain parametric values.

- The natural frequencies are reduced with an increase in electrostatic force. The plate becomes unstable at certain parametric combinations.

- The Casimir effect causes a reduction in the natural frequencies. A sufficiently high voltage will cause instability in the plates resulting in stiction. The effect of the Casimir force accounts for about 10 % of the reduction in the natural frequency for C-C-C-C parallel microplates reduced in gap from 1 μm to 0.1 μm. Similar reductions are noted for microplates with other boundary conditions, actually resulting in stiction for cantilever microplate having the dimensions used in this research. Plates designed and fabricated in the MUMPs technology are not affected by Casimir force due to the fact that its influence is insignificant at a gap of 2 μm, which the technology requires.

- The increase in voltage causes a corresponding non-linear decrease in the natural frequency ultimately resulting in stiction. This decrease is also dependent on the side ratio and the nature of the geometric boundary conditions. It is found that as the side ratio is increased, the natural frequencies are reduced. The boundary conditions determine the elastic restoring force that prevent stiction and is highest with the C-C-C-C plate decreasing in magnitude in the following order: C-F-C-C, C-F-C-F, C-C-F-F, and F-F-F-C, the cantilever microplate.

5.2 RECOMMENDATIONS FOR FURTHER WORK

The field of microelectromechanical systems (MEMS) has expanded considerably over the last decade and is expected to be of major industrial significance in the years to come. The discovery of novel materials, processes, and phenomena at the micro and nano scale and the development of new experimental and theoretical techniques for investigations provide fresh opportunities for scientific and technological developments in microelectromechanical systems (MEMS). There is an increasing need for a multidisciplinary and system-oriented approach for the development of MEMS devices that function reliably. This can be achieved through concerted research work in this multidisciplinary area.

The development, performance and reliability of capacitive MEMS would benefit from increased research activity in the following areas:

- Improved accuracy by considering higher order approximations to the potential terms for electrostatic and Casimir energies in the Rayleigh-Ritz method

- Inclusion of the fringing effects and surface charge layer in the problem formulation.

- The mechanical properties of micro and sub-micron structural elements differ from that predicted by continuum mechanics as reported by Miller and Shenoy (2000) and Namazu et al (2000). Similar thought should be extended to considerations of the applicable field forces in generating mathematical models for analysis.

- Efficient numerical schemes such as a hybrid FEM/BEM model for analysis could be used to investigate the curve veering behavior and study the influence of parametric variations on the microplate.

- Experimental validation of results taking into account the Casimir effect

•

REFERENCES

1. Aluru, N.R., "A particle method for analysis of microelectromechanical switches," *DSC-Vol. 66, Microelectromechanical Systems (MEMS)*, pp. 531-536, ASME, 1998.
2. Ambjorn, J. and S. Wolfram, "Properties of the vacuum, 1. Mechanical and Thermodynamic," *Annals of Physics*, Vol. 147, pp. 1-32, 1983.
3. Arnold, W., Hunklinger, S. and K. Dransfeld, "Influence of optical absorption on the Van der Waals interaction between solids," *Physical Review B*, Vol. 19, No. 12, 1979.
4. Bao, M.-H., *Micro Mechanical Transducers: Pressure Sensors, Accelerometers and Gyroscopes in Handbook of Sensors and Actuators*, Vol. 8, Elsevier, New York, 2000.
5. Bhat, R. B., "Curve veering: Inherent behavior of some vibrating systems," *Shock and Vibration*, Vol. 7, pp. 1-9 SAV 112, 2000.
6. Bhat, R. B., "Natural frequencies of rectangular plates using characteristic orthogonal polynomials in Rayleigh-Ritz method," *Journal of Sound and Vibration*, Vol. 102, No. 4, pp. 493-499, 1985.
7. Bhat, R. B. and I. Stiharu, "Disordered dynamic systems resulting from approximate modeling and analysis," *Proceedings the ASME Congress and Exposition, November 5-10, 2000, Orlando, Florida*, 2000.
8. Bingqian, L., Changchun, Z. and L. Junhua, "Electrostatic force influenced by space charge in submicrometer or nanometer silicon microstructures," *Journal of Micromechatronics and Microengineering*, Vol. 9, pp. 319-323, 1999.

9. Bordag, M., Klimchitskaya, G. L. and V. M. Mostepanenko, "The Casimir force between plates with small deviations from plane parallel geometry," *International Journal of Modern Physics A*, Vol. 10, No. 18, pp. 2661-2681, 1995.

10. Bordag, M., Mohideen, U. and V. M. Mostepanenko, "New developments in the Casimir Effect," *Physics Reports*, Vol. 353, Nos 1-3, pp. 1-205, 2001.

11. Burden, R. L. and J. D. Faires, *Numerical Analysis*, 5th ed., PWS-Kent Pub. Co., Boston, 1993.

12. Casimir, H. B.G. and D. Polder, "The influence of retardation on the London-van der Waals forces," *Physical Reviews*, Vol. 73, pp. 360-372, 1948.

13. Chakraverty, S., Bhat, R.B. and I. Stiharu, "Dynamic Stability of Micro Diaphrams Under the Action of Non – Linear Electrostatic Forces," *Current Advances in Mechanical Design and Production*, 7th Cairo University International MDP Conference, Cairo, Feb. 15-17, 2000, pp. 69-76.

14. Chan E.K., Garikipati, K. and R.W. Dutton, "Characterization of contact electromechanics through capacitance-voltage measurements and simulations," *IEEE Journal of Microelectromechanical Systems*, Vol. 8, No. 2, pp. 208-217, June, 1999.

15. Chan, H. B., Aksyuk, V. A., Kleiman, R. N., Bishop, D. J. and F. Capasso, "Non-linear micromechanical Casimir oscillator," *Physical Review Letters*, Vol. 87, No. 21, 211801-1-211801-4, 2001.

16. Chen, P. and J. H. Ginsberg, "On the relationship between veering of eigenvalue loci and parameter sensitivity of eigenfunctions," *Journal of Vibration and Acoustics*, Vol. 114, pp. 141-148, 1992.

17. Claassen, R. W. and C. J. Thorne, "Vibrations of a rectangular cantilever plate," *Journal of Aerospace Science*, Vol. 29, pp. 1300-1305, 1962.

18. Cronos Integrated Systems, *MUMPs Design Handbook*, JDS Uniphase, Research Triangle Park, North Carolina, 2001.

19. Dagani, O., Socher, E., Lipson, A. Leitner, T., Setter, D. J., Kaldor, S. and Y. Nemirovsky, "Pull-in study of electrostatic torsion microactuator," *Journal of Microelectromechanical Systems*, Vol. 7, No. 4, pp. 373-379, 1998.

20. DeRaad, L. L. and K. A. Milton, "Casimir self-stress on a perfectly conducting cylindrical shell," *Annals of Physics*, Vol. 136, pp. 229-242, 1981.

21. Dickson, S. M. and E. K. H. Li, "On the use of simply supported plate functions in Rayleigh-Ritz method applied to the flexural vibration of rectangular plates," *Journal of Sound and Vibration*, Vol. 80, pp. 292-297, 1982.

22. Ehrfeld, W., Bley, P. Gotz, F. and P. Hagemann, "Fabrication of microstructures using the LIGA process," *IEEE Micro Robots and Teleoperators Workshop (Hyannis, Massachusetts)*, p. 11, IEEE, New York, 1987.

23. Ehrfeld, W., Glashauser, W., Munchmeyer, D. and W. Schelb, "Mask making for synchrotron radiation lithography," *Microelectronic Engineering*, Vol. 5, pp. 463-470, 1986.

24. Ehrfeld, W., Gotz, F., Munchmeyer, D. and W. Schelb, "LIGA process: sensor construction techniques via X-ray lithography," *IEEE Solid State Sensors and Actuators Workshop*, pp. 1-4, IEEE, New York, 1988.

25. Feynman, R., "There's plenty of room at the bottom," *Miniaturization*, edited by H. D. Gilbert, Reinhold, New York, 1961.

26. Fujita, H. and A. Omodaka, "Electrostatic actuators for micromechatronics," *IEEE Micro Robotics and Temperature Workshop (Hyannis, Massachusetts)*, p. 14, IEEE, New York, 1987.

27. Fuller,.S.B., Wilhelm, E. J. and J. M. Jacobson, "Ink-jet printed nanoparticle microelectromechanical systems," *Journal of Microelectromechanical Systems*, Vol. 11, No. 1, pp. 54-60, 2002.

28. Gabriel, K., Jarvis, J. and W. Trimmer (ed.), "Small machines, large opportunities: a report on the emerging field of microdynamics," *The NSF Workshop on Microelectromechanical Systems Research*, 1988.

29. Gianchandani, Y. B. and K. Najafi, "A bulk silicon dissolved wafer process for microelectromechanical devices," *Journal of Microelectromechanical Systems*, Vol. 1, No. 2, pp. 77-85, 1992.

30. Guckel, H., Christenson, T. R., Strobis, K. J. and T. S. Jung, "A first functional current exited planer rotational magnetic microactuator," *IEEE Microelectromechanical Systems (Fort Lauderdale, Florida)*, pp. 7-11, IEEE, New York, 1993.

31. Guckel, H., Strobis, K. J., Christenson, T. R. and J. Klein, "Fabrication of assembled micromechanical components via deep x-ray lithography," *IEEE Microelectromechanical Systems (Nara, Japan)*, pp. 74-79, IEEE, New York, 1991.

32. Harris, B. W., Chen, F. and U. Mohideen, "Precision measurement of the Casimir force using gold surfaces," *Physical Reviews A*, No. 62, p. 052109-052113, 2000.

33. Heuberger, A., "X-ray lithography," *Microelectronic Engineering*, Vol. 5, pp. 2-38, 1986.

34. Heuberger, A., and H. Betz, "X-ray lithography with synchrotron radiation," *Solid-state devices*, (ed. A. Goetzberger and M. Zerbst), Verlag Chemie, Weinheim, 1983.

35. Hung, E.S., and S.D. Senturia, "Generating efficient models for microelectromechanical systems from a few finite element simulation runs," *IEEE Journal of Microelectromechanical Systems*, Vol. 8, No. 3, pp. 230-289, September, 1999.

36. Itzykson, C. and J.-B. Zuber, *Quantum Field Theory*, McGraw-Hill, New York, 1980.

37. Jebens, R., Trimmer, W. and J. Walker, "Microactuators for aligning optical fibers," *Sensors and Actuators*, Vol. 20, pp. 65-73, 1989.

38. Kovacs, G. T. A., *Micromachined Transducers Sourcebook*, McGraw-Hill, New York, 1998.

39. Kuttler, J. B. and V.G. Sigillito, "On curve veering," *Journal of Sound and Vibration*, Vol. 75, No. 4, pp. 585-588, 1981.

40. Lamoreaux, S. K., "Demonstration of the Casimir effect in the 0.6 μm to 6.0 μm range," *Physical Reviews Letters*, Vol. 78, pp. 5-8, 1997.

41. Legtenberg, R., Eldens J. and Elwenspoek, M., "Stiction of surface micromachined structures after rinsing and drying: Model and investigation of adhesion mechanism," *Proceedings of Transducer 93*, 1993, pp. 198-201

42. Legtenberg, R., Gilbert, J. and S.D. Senturia, "Electrostatic curved electrode actuators," *IEEE Journal of Microelectromechanical Systems*, Vol. 6, No. 3, pp. 257-265, September, 1997.

43. Leissa, A. W., "On a curve veering aberration," *Journal of Applied Mathematics and Physics (ZAMP)*, Vol. 25, pp. 99-110, 1974.

44. Leissa, A. W., "On vibration of rectangular plates," *Journal of Sound and Vibration*, 1975.

45. Leissa, A. W., "The free vibration of rectangular plates," *Journal of Sound and Vibration*, Vol. 31, No. 3, pp. 257-293, 1973.

46. Li, X.-Z., Cheng, H.-B., Li, J.-M., X.-H. Zhai, "Attractive or repulsive nature of the Casimir force for rectangular cavity," *Physical Reviews D* , No. 56, pp. 2155-2162, 1997.

47. Linder, S., Baltes, H., Gnaedinger, F. and E. Doering, "Photolithography in anisotropically etched grooves," *Proceedings of the Ninth IEEE Workshop on Micro Electro Mechanical Systems, San Diego, California*, February 11-15, 1996, p.38.

48. Lukosz, W. "Electromagnetic zero-point energy and radiation pressure for a rectangular cavity," *Physica*, Vol. 56, pp. 109-120, 1971.

49. Macklay, G. J., " Analysis of zero-point electromagnetic energy and Casimir forces in conducting rectangular cavities," *Physical Reviews A*, No. 61, pp. 052110-052117, 2000.

50. Macklay, G. J., "Unusual properties of conductive rectangular cavities in the zero point electromagnetic field: Resolving Forward's Casimir energy extraction cycle paradox," *Proceedings of STAIF-99 (Space Technology and Applications International Forum), Albuquerque, New Mexico*, January, 1999.

51. Madou, M. J., *Fundamentals of Microfabrication*, CRC Press, Boca Raton, Florida, 1997.

52. Mamaev, S. G. and N. N. Trunov, "Dependence of the vacuum expectation values of the energy-momentum tensor on the geometry and topology of the manifold," *Theoretical and Mathematical Physics (USA)*, Vol. 38, No. 2, pp. 228-234, 1979.

53. Mastrangelo, C.H. and C. H. Hsu, "Mechanical stability and adhesion of microstructures under capillary forces - Part I: Basic theory," *Journal of Microelectromechanical Systems*, Vol. 2, No.1, pp. 33-43, 1993.

54. Mastrangelo, C.H. and C.H Hsu, "Mechanical stability and adhesion of microstructures under capillary forces - Part II: Experiments," *Journal of Microelectromechanical systems*, Vol. 2, No.1, pp. 44-55, 1993.

55. Masuzawa, T. "Micromachining by machine tools," *Micro Mechanical Systems: Principles and Technology*, edited by T. Fukuda and W. Menz, New York, NY: Elsevier, 1998 pp 63-82.

56. Menz, W., Bacher, W., Harmening, M. and A. Michel, "The LIGA technique: a novel concept for microstructures and the combination with silicon technologies by injection molding," *IEEE Microelectromechanical Systems (Nara, Japan)*, pp. 69-73, IEEE, New York, 1991.

57. Miller, R. E. and V. B. Shenoy, "Size-dependent elastic properties of nanosized structural elements," *Nanotechnology*, Vol. 11, pp. 139-147, 2000.

58. Milonni, P. W., *The Quantum Vacuum: An Introduction to Quantum Electrodynamics*, Academic Press, San Diego, California, 1994.

59. Milton, K. A. and Y. J. Ng, "Observability of the bulk Casimir effect: Can the dynamical Casimir effect be relevant to sonoluminescence?" *Physical Reviews E*, No. 57, pp. 5504-5510, 1998.

60. Mohideen, U. and A. Roy, "Precision measurement of the Casimir force from 0.1 to 0.9 micron," *Physical Review Letters*, Vol. 81, pp. 4549-4552, 1998

61. Morse, P.M., *Vibrations and Sound*, New York, NY: McGraw Hill, 1948.

62. Mostepanenko, V. M. and N. N. Trunov, *The Casimir Effect and its Applications*, Clarendon Press, Oxford, 1997.

63. Muthukumaran, P. Stiharu, I. and Bhat, R.B., "Gas Phase Xenon Difluoride Etching of Microsystems Fabricated through Mitel 1.5 mm CMOS Process," *Canadian Journal of Electrical and Computer Engineering*, Vol. 25, No. 1, pp. 35-41, 2000.

64. Namazu, T., Isono, Y. and T. Tanaka, "Evaluation of size effect on mechanical properties of single crystal silicon by nanoscale bending test using AFM," *Journal of Microelectromechanical Systems*, Vol. 9, No. 4, pp. 450-459, 2000.

65. Nemirovsky, Y. and O. Bochobza-Degani, "A methodology and model for the pull-in parameters of electrostatic actuators," *Journal of Microelectromechanical Systems*, Vol. 10, No. 4, pp. 601-615, 2001.

66. Packirisamy, M., Stiharu, I. and Bhat, R.B., "Vibration of micromachined condenser microphone plate diaphragms in electrostatic fields," *CANCAM 97, 16th Canadian Congress of Applied Mechanics, Quebec, Canada*, June 1-6, 1997, pp. 87-88.

67. Perkins, N. C. and C. D. Mote, "Comments on curve veering in eigenvalue problems," *Journal of Sound and Vibration*, Vol. 106, No. 3, pp. 451-463, 1986.

68. Puers, R. and D. Lapadatu, "Electrostatic forces and their effect on capacitive mechanical sensors," *Sensors and Actuators*, Vol. 56, No. 3, pp. 203-210, 1996.

69. Rajalingham, C. and R. B. Bhat, "Influence of an electric field on diaphragm stability and vibration in a condenser microphone," *Journal of Sound and Vibration*, Vol. 211, No. 5, pp. 819-827, 1998.

70. Rajalingham, C. and R.B. Bhat, "Influence of an electric field on diaphragm stability and vibration in a condenser microphone," *Journal of Sound and Vibration*, Vol. 211, No. 5, pp. 819-827, 1998.

71. Reed, M.L. and G.K. Fedder, "Photolithographic Microfabrication," *Micro Mechanical Systems: Principles and Technology in Handbook of Sensors and Actuators*, Vol. 6, edited by T. Fukuda and W. Menz, Elsevier, New York, NY, 1998, pp. 13-61.

72. Roy, A. and U. Mohideen, "Demonstration of the non-trivial boundary dependence of the Casimir force," *Physical Reviews Letters*, Vol. 82, p. 4380-4380, 1999

73. Runyan W. R. and K. E. Bean, *Semiconductor Integrated Circuit Process Technology*, Addison-Wesley, Reading, Massachusetts, 1994.

74. Saif, M. T. A., Alaca, B. E. and H. Sehitoglu, "Analytical modeling of electrostatic membrane actuator for micro pumps," *IEEE Journal of Microelectromechanical Systems*, Vol. 8, No. 3, pp. 335-345, 1999.

75. Saumaun, Wise, K. D. and J. B. Angell, "An IC piezoresistive pressure sensor for biomedical instrumentation," *IEEE Transactions on Biomedical Engineeing*, Vol. BME-20, pp. 101-109, 1973.

76. Schajer, G. S., "The vibration of a rotating circular string subject to a fixed elastic restraint," *Journal of Sound and Vibration*, Vol. 92, No. 1, pp. 11-19, 1984.

77. Serry, M. Walliser, D. and G. J. Macklay, "The Anharmonic Casimir Oscillator (ACO) -- The Casimir Effect in a Model Microelectromechanical System," *IEEE Journal of Microelectromechanical Systems*, Vol. 4, No. 4, pp. 193-205, 1995.

78. Serry, M. Walliser, D. and G. J. Macklay, "The role of the Casimir effect in the static deflection and stiction of membrane strips in microelectromechanical systems (MEMS)," *Journal of Applied Physics*, Vol. 84, No. 5, pp. 2501-2506, 1998.

79. Sparnaay, M. J., "The historical background of the Casimir effect," *Physics in the Making*, edited by A. Sarlemijn and M. J. Sparnaay, Elsevier, Amsterdam, 1989.

80. Stiharu, I., and R. B. Bhat, " Vibration of microplates in electrostatic fields using Rayleigh-Ritz method," *Proceedings of the 15th International Modal Analysis Conference, Society of Experimental Mechanics, Orlando, Florida*, 1997, p.765.

81. Stiharu, I., Rakheja, S. and L. Wang, "Humidity microsensor in CMOS Mitel15 technology," *Proceedings of the IEEE, Canadian Conf. on Electrical and Computer Engineering, Edmonton, Alberta*, May 9-12, 1999, pp. 1652-1657.

82. Sze, S. M. (ed.), *Semiconductor Sensors*, Wiley, New York, 1994.

83. Tsai, J., *Further Investigations on Curve Veering Phenomenon*, Ph.D. Thesis, The Ohio State University, 1993.

84. Tufte, O. N., Chapman, P W. and D. Long, "Silicon diffused-element piezoresistive diaphragms," *Journal of Applied Physics*, Vol.33, pp. 3322-3327, 1962.

85. Warburton, G. B., "The vibration of rectangular plates," *Proceedings of the Institute of Mechanical Engineers*, Series A, Vol. 168, pp. 371-384, 1954.

86. Weaver, W. Jr., Timoshenko, S. P. and D. H. Young, *Vibration Problems in Engineering*, 5th ed., Wiley, New York, 1990.

87. Wen, Ko, H., Hynecek, J. and S. F. Boettcher, "Development of a miniature pressure transducer for biomedical applications," *IEEE Transactions on Electron Devices*, Vol. ED-26, pp. 1896-1905, 1979.

88. Ye, W., and S. Mukherjee, "Design and fabrication of an electrostatic variable gap comb drive in microelectromechanical systems," *DSC-Vol. 66, Microelectromechanical Systems (MEMS)*, pp. 537-544, ASME, 1998.

89. Ziebart, V., Paul, O. and H. Baltes, "Strongly buckled square micromachined membranes," *Journal of Microelectromechanical Systems*, Vol. 8, No. 4, pp. 423-432, 1999.

APPENDICES

A. FABRICATION

As previously mentioned certain design processes and technologies have dominated others. Fabrication of MEMS may be carried out in three main ways:

- Photolithographic fabrication
- Fabrication using LIGA technology
- Micromachining by machine tools

A1. PHOTOLITHOGRAPHIC FABRICATION

Photolithographic fabrication on a planar substrate accounts for the overwhelming majority of commercially available MEMS devices and is the most developed of all microsystems technologies. It capitalizes heavily on existing integrated circuit (IC) technology, resulting in designs of microdevices that are capable of integrating mixed domain transducers with electronic circuitry on a single chip. Hence engineers and scientists have been able to produce functional microdevices that incorporate combinations of mechanical, thermal, magnetic, electrostatic, piezoelectric and other domain elements with the associated electronics. This is achieved at relatively low unit costs only when associated with very high volumes of production.

The fabrication processes in lithographic pattern transfer is well documented in the literature and include texts by Sze (1994), Madou (1997) and Kovacs (1998). In this

section of the thesis, an overview of some of the fundamental unit processes used in fabrication is presented.

Various combinations of these unit processes using photolithographic technology result in different integrated processes for the fabrication of MEMS devices. These include the common processes associated with fabrication on planar substrates described in later sections but are briefly stated here (Reed and Fedder, 1998).

- **Bulk micromachining** in which part of the silicon substrate is etched to produce mechanical elements such as pressure or acceleration transducers illustrated in Fig. 2.1. This fabrication technique accounts for the production of the majority of commercially available transducers currently marketed.

- **Surface micromachining** utilizes alternating patterned layers of silicon dioxide and polysilicon to create transducers on the surface of the silicon chip. The silicon dioxide is treated as a sacrificial layer and is etched to *release* the mechanical device from the substrate in a post processing operation without attacking the structural polysilicon layer as illustrated in Fig. 2.2. Surface micromachined devices are more conveniently amenable to integration with electronic circuitry on the same chip. An example is the ADXL 150 and ADXL 250 accelerometers currently manufactured and marketed by Analog Devices.

- **Dissolved wafer process** uses techniques similar to surface fabrication but is capable of producing arbitrarily shaped elements with no constraints on spacing between

elements (Gianchandani and Najafi, 1992). The material used is a single-crystal heavily boron doped silicon bonded to a glass substrate. After the unit processes for fabrication are carried out, the structure is released by dissolving the wafer in an appropriate solution, which etches the bulk silicon wafer without attacking the heavily boron-doped silicon regions and other desired features. After this process, boron-doped freestanding microstructures are left on the surface of the glass wafer. This process is capable of yielding microstructures of up to 35 μm in thickness (Reed and Fedder, 1998).

- **Standard CMOS process**

Thin film processes are used in the fabrication of devices to generate relatively thin layers on the planar substrate. These layers may be grown or deposited. Grown layers are those in which the silicon film originates from within the wafer bulk, while deposited films originate from outside the wafer. The ensuing properties of the interface between a grown film and the substrate differ greatly from that for a deposited film and the corresponding substrate. Grown oxide films for instance exhibit a much lower density of electronic defects, which adversely affect device performance.

As mentioned earlier, a combination of the fundamental unit processes result in a development of integrated processes that are customized to fabricate micro devices. The more common thin film processes, which will be described, include thermal oxidation, chemical vapor deposition (CVD), evaporation, and sputtering. A description of the photolithographic process and etching methods will then follow.

A1.1 Thermal Oxidation

In the thermal oxidation process, a film of silicon dioxide is grown on the surface of the wafer by the oxidation of silicon with water or dry oxygen in a furnace at temperatures of about 900°C to 1000°C (Kovacs, 1998). Oxidation proceeds more rapidly with water than with dry oxygen and is preferred for films greater than about 0.2 μm whereas the latter produces better interfaces and slightly denser films, which are more appropriate for hard masking.

A typical furnace used for thermal oxidation is shown in Fig. A1.1. It comprises of resistively heated, hot wall, open quartz tubes. Wafers are stacked in a slotted quartz wafer boat that takes about thirty wafers per batch. Hydrogen and oxygen are supplied through conduits into the furnace while a separate conduit is provided for discharging the nitrogen gases produced (Reed and Fedder, 1998).

The process is controlled by the reaction of the oxide at the interface rather than the flow rate of the oxidants into the furnace. The water used in the oxidation process may be obtained either by the reaction of hydrogen and oxygen or by routing oxygen through a container of liquid water. However, it is imperative to carefully determine the flow to avoid explosions caused by the hydrogen.

At the beginning of the oxidation process, the reaction rate is limited by the availability of surface reaction sites. The Deal-Grove model (Runyan and Bean 1990) is used to determine the time required to grow a certain thickness of silicon dioxide and is given as

$$t = \frac{x}{B/A} \tag{A1.1}$$

where t is the oxidation time, x is the oxide thickness and B/A is a linear rate constant expressed in terms of the used units.

Further oxidation of the silicon results in the initial silicon dioxide layer forming a barrier to incoming oxidants, necessitating diffusion through the oxide layer to continue the oxidation process. This proceeds as the oxidants interact with the silicon atoms at the silicon/ silicon dioxide interface where they are available. In this region the time required for oxidation is given by (Reed and Fedder, 1998)

$$t = \frac{x^2}{B} \tag{A1.2}$$

where B is the parabolic rate constant. The total time is a combination of the linear and non-linear region simply given from Eqs. 2.1 and 2.2 as

$$t = \frac{x}{B/A} + \frac{x^2}{B} \tag{A1.3}$$

Uniform and consistent oxidation thickness is replicated by a precise control of the temperature in the oxidation process since the linear and parabolic rate constants are thermally dependent.

An advantage of the thermal oxidation process is that it inherently results in an interface that is completely free of impurities as it is formed inside a crystalline silicon lattice. This enables the interface with a p-n junction to have controlled, reproducible electronic properties compared with junctions formed at the intersection of an unoxidized surface.

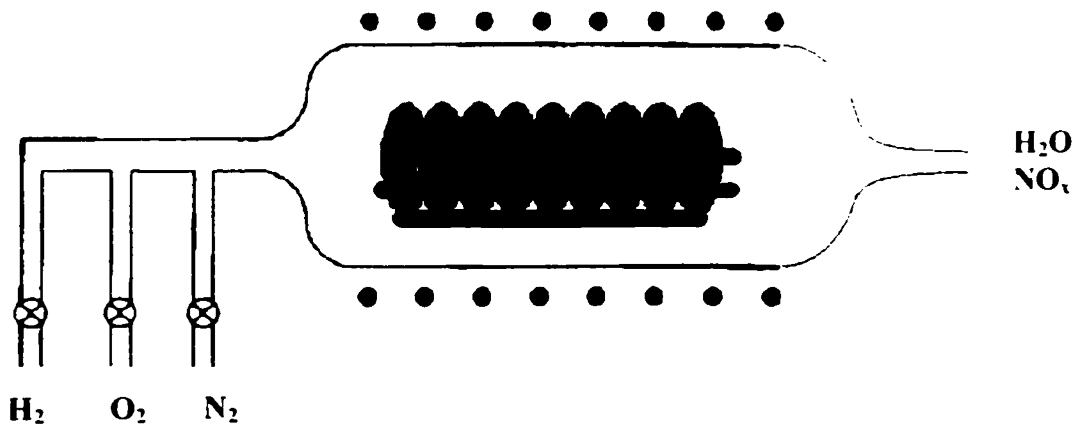

Fig A1.1 **Arrangement of a thermal oxidation system**

A1.2 Chemical Vapor Deposition (CVD)

Chemical Vapor Deposition (CVD) is used for the deposition of thin films such as polysilicon layers as well as silicon dioxide, silicon nitride, and certain metal layers in the fabrication of MEMS. The components of the film are transported as gases through reactants. These gases react on the surface of the wafer to achieve the desired film. Situations in which the reaction takes place in the gas stream usually results in the formation of particles on the wafer rather than a smooth film and is referred to as *gas-phase nucleation.*

There are two primary methods for Chemical Vapor Deposition namely Low Pressure Chemical Vapor Deposition (LPCVD) and Plasma-Enhanced Chemical Vapor Deposition (PECVD). In LPCVD the equipment used is an oxidation chamber similar to that used for thermal oxidation, in which the tube is sealed and evacuated as shown in Fig. A1.2a. Unlike the thermal oxidation process where precise thermal control is necessary and precision mass flow control is not, the converse is required in CVD. In this process the rate at which the deposition process proceeds is dependent on transport of the reactants, and hence it is absolutely necessary to precisely control the mass flow of reactants into the furnace. On the other hand precise temperature control is not required but tight ranges are recommended.

LPCVD is carried out at low pressures that typically range from 0.15 to 2 torr and relatively low temperatures of about 400°C to 700°C. This method is commonly used to deposit polysilicon layers by the pyrolytic decomposition of silane into silicon and

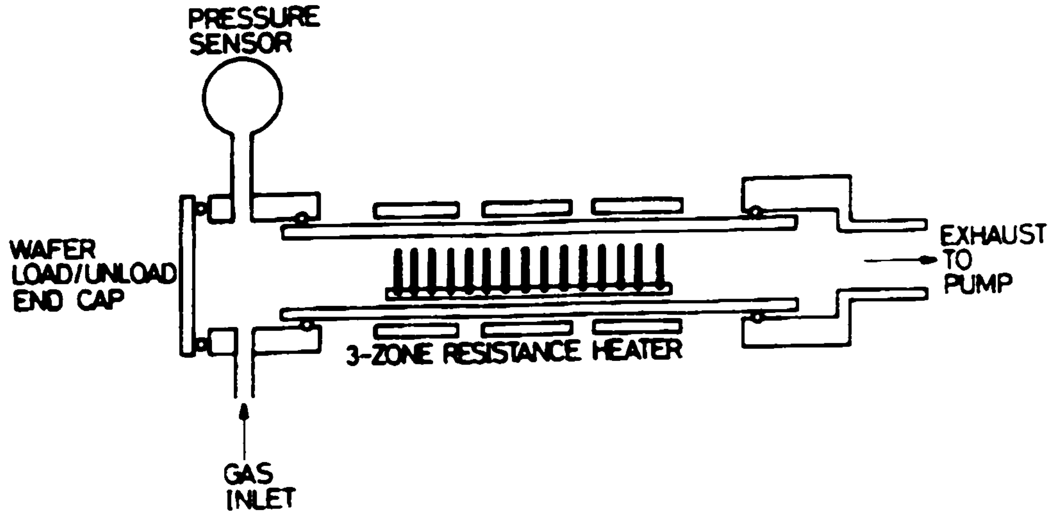

Fig. A1.2a Low pressure chemical vapor deposition (LPCVD)

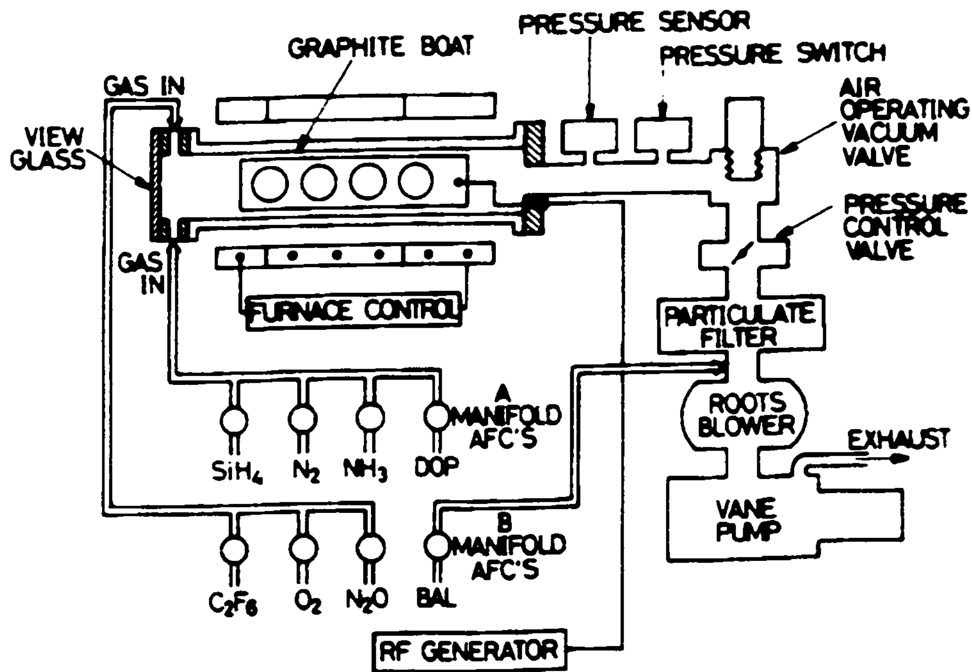

Fig. A1.2b Plasma enhanced chemical vapor deposition (PECVD)

Fig. A1.2 Chemical vapor deposition (Sze, 1994)

hydrogen. LPCVD is also used to deposit silicon dioxide films by the reaction of silicon and oxygen gas. The deposition of silicon nitride films is carried out using LPCVD by the reaction of silicon and ammonia gas at higher temperature ranges of between 800°C to 900°C introducing residual stresses in the film which are controlled by varying the amount of the respective reactants.

PECVD technology is driven by the collision of energetic electrons in a glow discharge rather than by thermal energy. In this method an rf generator is used to set up the plasma. PECVD usually takes place at very low ambient temperatures. Though the process can proceed at room temperature, the substrate is usually heated to about 300°C to improve adhesion. The system is first evacuated and a gas containing the atomic components of the film is delivered to the chamber at a pressure of a few mT. The plasma is then ignited creating many ionized species, some being deposited on the substrate forming a solid film. This process is commonly used to deposit silicon nitride layers in MEMS technology. Generally PECVD results in films that have growth rates of the order of microns per minute. Another advantage of PECVD is the higher etch rates achievable compared with films deposited by other means (Reed and Fedder, 1998). Furthermore, deposition proceeds at a lower temperature than for LPCVD. However, due to the directionality of the plasma, PECVD generally result in non-conformal film deposition. The quality of PECVD films is usually lower than that obtained using LPCVD and is less uniform.

A1.3 Evaporation

Evaporation is a physical deposition process that takes place in a chamber depicted in Fig. A1.3. In this process, the material to be deposited is placed on a crucible that is heated using such as electron beam laser or a high current until vaporization takes place in a very low-pressure chamber (as low as 10^{-7} torr). Other methods for heating include the use of thermal evaporators and flash evaporators. E-beam systems are preferred due to the high deposition rates achievable and purity of thin films deposited. The vapor then condenses on the planar substrates arranged near the top of the chamber. The deposition of elemental metals is most often carried out using this technique. However, other materials including ceramics could be deposited through this method.

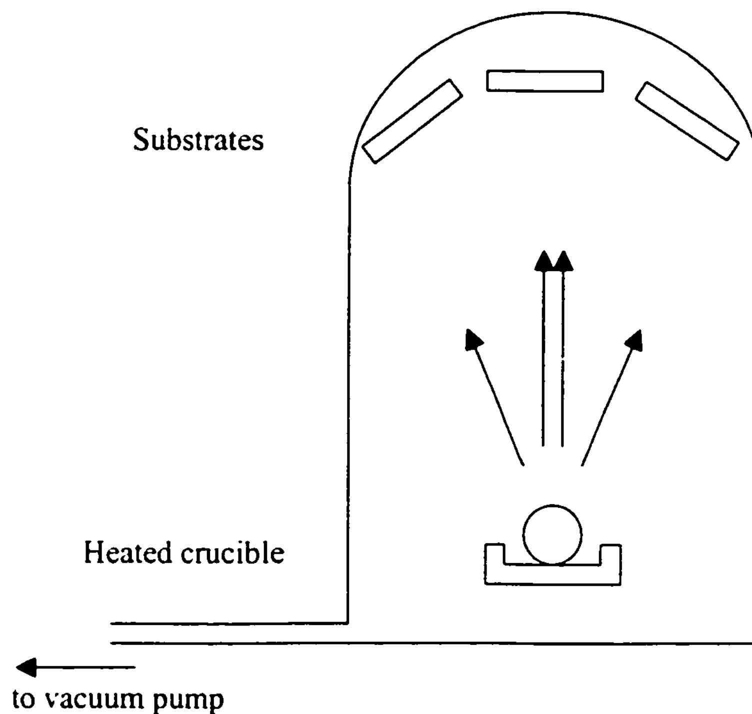

Fig. A1.3 Evaporation system

A1.4 Sputtering

Sputtering is a process in which electron impact ionization of a neutral gas, such as argon, creates energetic ions in glow discharge plasma. The ions are attracted to an electrically biased target containing the source material causing a displacement of atoms of the element, which are then deposited on the substrate as illustrated in Fig. A1.4.

In situations where reactive gases are preferred to strike plasma, chemical reactions result, which are exploited for deposition and is known as *reactive sputtering*. Oxygen sputtered on a zinc target would result in the deposition of zinc oxide while nitrogen on a silicon target would result in the deposition of a thin film of silicon nitride.

Sputtering is generally preferred to evaporation for the following reasons:

- It results in more convenient deposition of compound films
- The vacuum chamber is more compact resulting in less pump-down time leading to higher throughput for the system
- Conformal deposition is achieved in a less expensive and efficient manner than evaporation
- The substrate remains cooler for comparative deposition rates

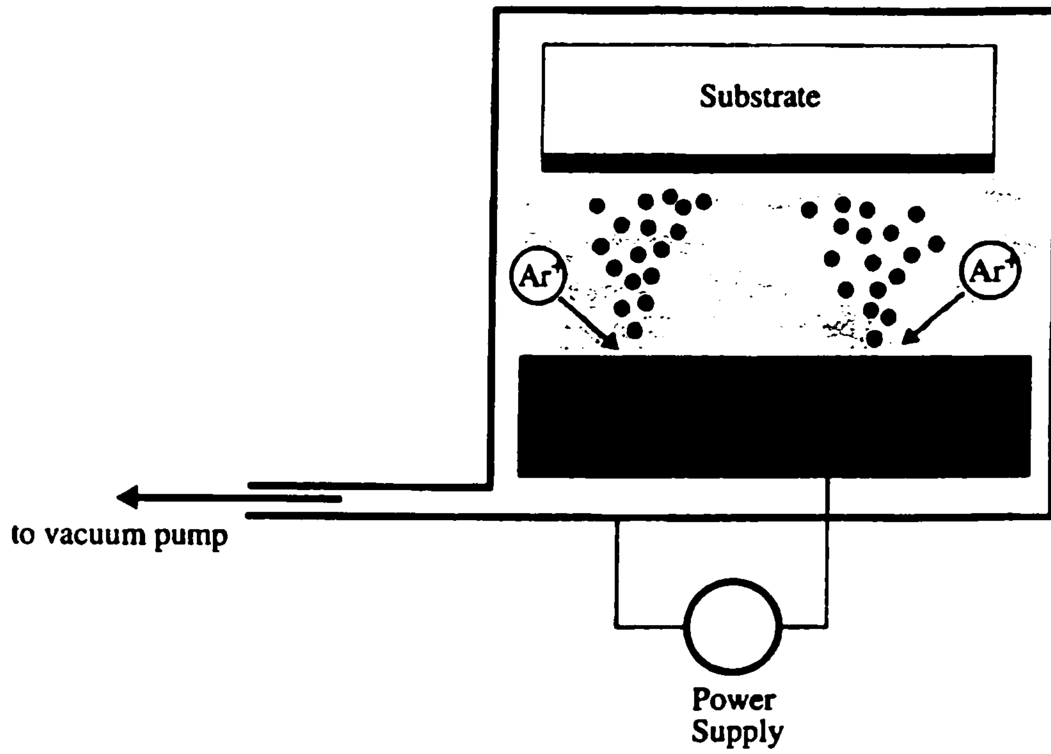

Fig. A1.4 Sputtering system

A1.5 Photolithography

In the fabrication of MEMS commencing with planar substrates, photolithography is a ubiquitous and indispensable step in the fabrication process. Comprising a few basic steps that are carried out repetitively, various patterns are produced and transferred to the substrates resulting in the design and production of a wide variety of MEMS devices.

The main steps used in photolithography of planar substrates are enunciated in the following (Madou, 1997, Kovacs, 1998, Reed and Fedder, 1998):

1. Prebake

The wafer is heated for a few minutes at temperatures in excess of 200°C to vaporize any remnants of water molecules on the wafer surface and improve the adhesion of photoresist.

2. Surface treatment for adhesion

This is carried out to ensure a better surface for adhesion bonding of the photoresist by the treatment of the wafer with an adhesion promoter such as hexamethyldisilizane (HMDS). The wafer is placed on a vacuum chuck and the HMDS is applied on it by spin coating.

3. Application of photoresist

The photoresist is applied to the surface of the wafer by spin coating. Specifically the wafer is placed on a vacuum chuck, which is rotated initially at a slow speed, gradually

increasing to several thousand revolutions per minute. As the rotation commences, resist is applied through a nozzle onto the wafer. The rotary motion causes all but a thin uniform layer of resist to remain on the substrate. The thickness of this layer is controlled by the speed of rotation and viscosity of the resist.

Application of resist over steps of more than about 0.5 μm result in a non-uniform thickness and subsequent unwanted variations in device dimensions. In order to overcome this, Linder et al (1996) proposed a method in which an electroplated resist is used to provide a conformal deposit of resist over large step sizes as high as 600 μm and mostly used in LIGA technology.

4. Softbake

This step enhances the adhesion of the photoresist to the substrate and removes any remnants of the solvent from the wafer surface and is carried out by baking in a convection oven at about 90°C for 30 minutes, or in an infrared oven for about 4 minutes or in a microwave oven for a few seconds.

5. Alignment

The wafers are aligned to the wafer flat in the equipment to be used for exposure in order to accurately transfer the projected patterns onto the wafer, corresponding with previously defined patterns. Anisotropic etching of the substrate creates alignment marks. This is more accurate since alignment is precisely done with respect to the crystal lattice. The method is useful in bulk micromachining.

6. **Exposure**

Exposure of the resist to an intense source of light is then carried out to create light and dark patterns on the mask. This exposure to light increases the solubility of the resist by a factor of about 1000 in a developer when a positive resist is used. Exposure may be by the whole-wafer method in which the entire wafer is exposed to UV light in one pass, or by the step-and-repeat system in which a smaller area (usually one die) is exposed in a single pass. The latter method yields a better precision for volume fabrication at the cost of an accurate system for movement control. This precision position control is achieved using *laser interferometry*.

7. **Development**

In this step spraying or dipping the wafer in suitable developing solvents such as sodium hydroxide or potassium hydroxide solutions in a controlled manner preserves the required dimensional integrity as the wafer is developed.

8. **Develop inspect**

After rinsing and drying, the wafers are inspected to ensure that the patterns were correctly transferred and dimensional integrity maintained. Fig. A1.5 illustrates examples of correctly exposed, over exposed and underexposed patterns as they relate to the critical dimensions of a tuning fork.

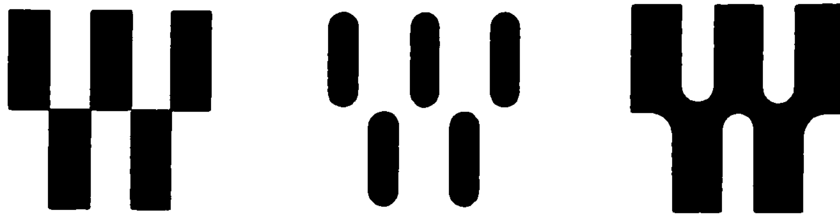

Fig. A1.5 Examples of correctly exposed, overexposed and underexposed lithographic patterns (Reed and Fedder, 1998)

9. Hardbake

This is carried out in a convection oven at about 150°C to 180°C for one hour to remove any traces of the solvent or water from the photoresist. It also improves the adhesion of the photoresist to the substrate.

10. Etching

The photoresist acts as an impervious layer to the etchant and permits etching of the thin film of material only in areas where the photoresist has been removed from the wafer.

11. Etch inspect

At this stage the wafer is inspected to verify that the etch step has progressed to achieve the desired result. If more etching is required, this is carefully done to ensure that the design dimensions are correctly obtained without over-etching.

12. Stripping

After etching, the photoresist is stripped by dissolving in suitable solvents such as trichloroethane, acetone or alcohol. Very hard resists are usually stripped using oxygen plasma. Any residues are removed with a mixture of sulfuric acid and hydrogen peroxide.

13. Final inspect

This final inspection is to verify dimensional integrity and to ensure that no photoresist remains on the wafer, as it may be inimical to subsequent fabrication processes.

A1.6 Etching

Etching in photolithographic fabrication is the removal of unwanted material with specified dimensions from a planar substrate. The substances and processes used in etching are classified broadly into isotropic and anisotropic etches and whether it is a wet or dry process. Isotropic etches remove material in a non-directional manner, without regard to the crystallographic plane directions in the structure of the silicon material. On the other hand anisotropic etches remove material along crystallographic directions for which a particular etchant is selective and is used to form through holes, pits and grooves. Selectivity of an etchant is described as the ratios of etch rates for the undesired material to that which is left respectively.

Isotropic Etching

Isotropic wet etching of silicon and polysilicon thin films can be carried out using a mixture of hydrofluoric and nitric acids. Alternatively a mixture of hydrofluoric acid, nitric acid ($HF:HNO_3:H_2O$) and acetic acid ($CH_3COOH:H_2O$) called HNA is preferably used at times. The acetic acid in the mixture ensures that etch surfaces are smoother. In this etching process the silicon is converted to an oxide by the nitric acid and then hydrofluoric acid attacks the oxide. Evidently this etchant is not selective against silicon dioxide films and must not be used where the process requires that silicon dioxide should remain after etching. Isotropic etching of silicon is usually carried out at room temperature.

Silicon dioxide is effectively etched with hydrofluoric acid ($HF:H_2O$) buffered with ammonium fluoride (NH_3F) which greatly increases its selectivity against photoresist and silicon. An unbuffered HF solution will attack the resist. This etching process may be carried out at room temperature. The etch rate is dependent on the dopant concentration and the density of the oxide layer. Phosphosilicate glass (PSG) and borosilicate glass (BSG) will etch more rapidly than thermally grown oxides, which are the slowest. Annealing at high temperatures densifies the PSG and BSG reduces the etch rate of both materials but results in a more uniform and reproducible rate.

Silicon nitride may be etched with phosphoric acid (H_3PO_4: H_2O) at 170 – 180°C that is capable of etching at a reasonably fast rate. However nitride is more commonly etched using plasma processes.

Anisotropic Etching

Suitable anisotropic etchants show a strong selectivity to various crystallographic planes in the silicon substrate and are widely used in bulk micromachining processes. The etchant exploits a difference in the etch rate of various planes with the {111} planes having the slowest rates. This process is used to create v-grooves, through holes and diaphragms as shown in Fig. A1.6.

Common anisotropic etchants include:

- Potassium hydroxide (KOH) aqueous solution, which in an aqueous form shows a selectivity of 200:1 for the {100} to {111}, planes respectively. This selectivity may be enhanced by the addition of isopropyl alcohol but it reduces the etch rate. Other alkali hydroxide solutions that may be used are NaOH, CsOH and tetramethyl ammonium hydroxide (TMAH).

- A mixture of ethylenediamine ($NH_2(CH_2)_2NH_2$), pyrocatechol ($C_6H_4(OH)_2$), in water is called EDP. Though it is not as selective as KOH, it offers greater flexibility. However handling should be with care as it is extremely toxic.

- Hydrazine, N_2H_4 is useful in processing with large etch rates. However this is at the expense of selectivity, which is relatively low being about 10:1 for {100} to {111} planes, respectively. This is an extremely hazardous material and must be handled with care.

The release of microstructures through the etching process may be unsuccessful due to *stiction*; the undesirable adhesion of the microstructure to the substrate. This occurs as a result of the surface tension forces generated, which could be as high as 70 kPa for a 2μm beam-substrate gap with a water droplet in between. Stiction is also caused by other forces such as electrostatic, van der Waals bonding, or the Casimir effect.

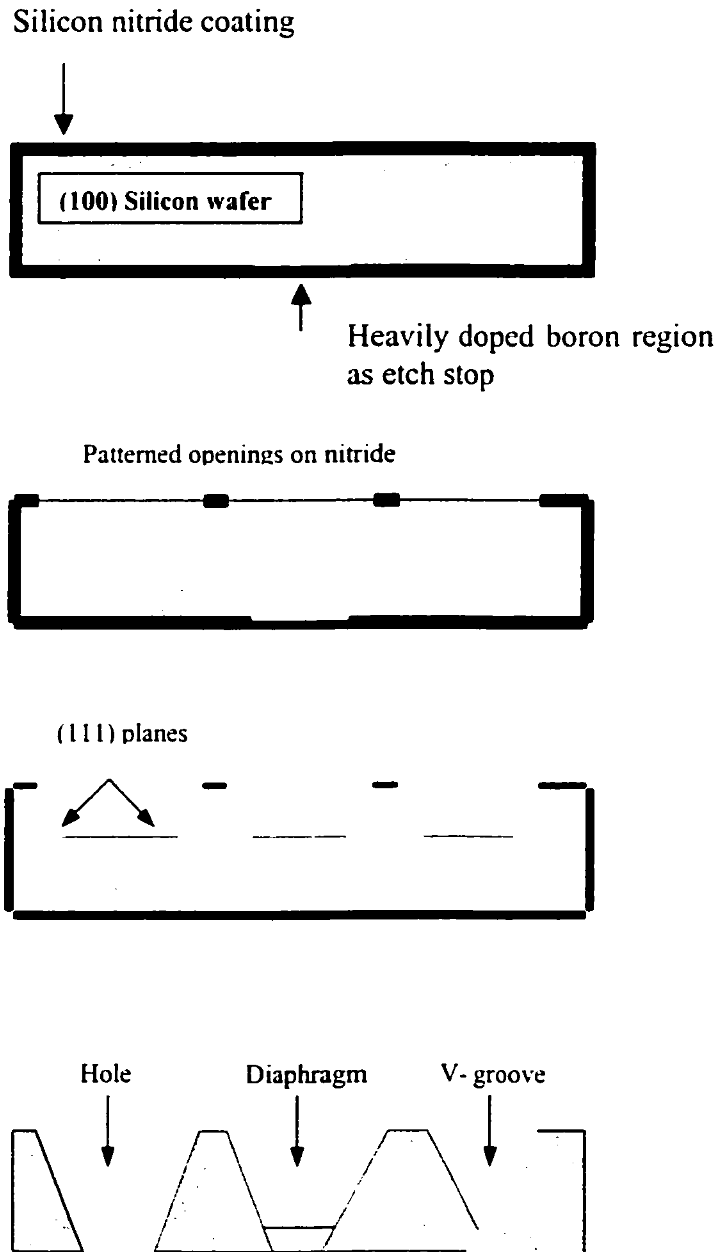

Fig. A1.6 V-groove etching

Dry Etching

This is an etching process in which gaseous plasmas are used to remove the unwanted material in a particular fabrication step. Problems associated with stiction that results from the wet etching release of a microstructure from the substrate are largely overcome by the use of dry etching techniques. Dry etching processes have the added advantage of cleanliness and compatibility with many materials. A major drawback is the complicated equipment and considerable process development required to achieve comparable results with wet etch processes. Various methods exist for dry etching which include:

- *Plasma etching*, an isotropic process in which the substrate remains unbiased.
- *Reactive Ion Etching(RIE)* where physical bombardment of the substrate by reactive ions provides a degree of anisotropy using chlorine based gases.
- *Ion milling* which is a physical process that removes material by the use of an intense low-energy beam of ions from a suitable gas such as oxygen or argon.
- *Gaseous phase etching* is a physical process in which a gas is used at a specific low pressure to remove the material to be etched. A suitable gas for this process is xenon difluoride (Muthukumaran, et al, 1999).

The common processes associated with photolithographic fabrication of MEMS devices on a planar substrate have been described. The basis of the analytical work carried out in this thesis is a capacitive type MEMS designed and fabricated in the Multi-User MEMS Processes (MUMPs) technology. The integrated process is surface micromachining, which incorporates all the basic processes described in the foregoing. The design and post processing of the proposed structure for our analysis will be given shortly in subsequent sections. Though photolithographic is the preferred method of fabrication for

the vast majority of current applications, other methods offer advantages which are appealing depending on the design objectives and function. Such a technology that offers great prospects is the LIGA technology.

A2. LIGA TECHNOLOGY

Photolithographic silicon processes of fabrication are limited to planar structures that have a maximum depth of about 10 µm and are two dimensional micromechanical devices. The LIGA technology process, which uses X-ray lithography, has overcome this limitation, extending batch fabrication of microstructures to three-dimensional devices. LIGA (an acronym from the German words, *Lithography, Galvanoformung, Abformung,* which stand for lithography, electroplating, and molding) is a micromachining technology that originated in the early 1980's at the Karlsruhe Nuclear Research Center.

As originally implemented, highly parallel X-rays of wavelength 0.2 to 2 nanometer from a synchrotron orbital radiation (SOR) acting as the etchant, are incident on a mask patterned with high Z-absorbers (Heuberger and Betz, 1983, Heuberger, 1986). The absorbers on the mask are thick enough to prevent the penetration of the X-rays. In the open areas of the mask, the radiation passes through and exposes PMMA (polymethyl-methacrylate) resist (Ehrfeld et al 1986, 1987). The resist is then developed and the resulting PMMA mold is used to produce a metal part by electroplating in the developed regions. The electroplating is either the final step in the process or the electroplated part is used as a mold for replication from another material such as plastic or ceramic.

By using the penetrating power of X-rays from a synchrotron, LIGA allows the fabrication of structures that have vertical dimensions from hundreds of microns to millimeters and horizontal dimensions that can be as small as microns. The 3-D microstructure defined by 2-D lithographic patterns is the key feature in this technology.

The height-to-width ratio capability is relevant to the manufacturing of miniature components that can withstand high pressure and temperature, and can transfer useful forces or torques. The material flexibility also offers opportunities to fabricate miniature components using LIGA instead of precision machining approaches such as wire electrodischarge grinding (WEDG) and electrodischarge machining (EDM), which are well described by Masuzawa (1998). The feature definition, radius, and sidewall texture using LIGA are superior to current precision machining techniques.

Advances in LIGA technology have made possible its combination with conventional silicon technologies to produce micromechanical devices, bringing it closer to standard fabrication processes (Guckel et al 1991, 1993). Using injection molding, Menz et al (1991) were able to produce microturbines. Monographs by Madou (1997) provide an introduction and overview of LIGA technology processes. As pointed out, the major limitation with widespread commercial application of this technology is the relatively high cost and the technical difficulty in producing the masks used in fabrication compared with standard photolithographic processes.

It is expected that when major markets emerge for devices with stringent conditions imposed on such parameters as resolution, high aspect ratio, and parallel structural walls, sufficient motivation would be generated to make commercial and industrial commitments that will justify the competitive use of LIGA technology processes in micro devices. It is conceivable that such markets may emerge in the near future in the field of micro-optical electromechanical systems (MOEMS), the fabrication of electrostatic

actuators that have the potential to produce much larger forces with higher aspect ratios, and in fulfilling the more stringent requirements imposed on packaging of integrated circuits and other micro devices as required for military and aerospace applications.

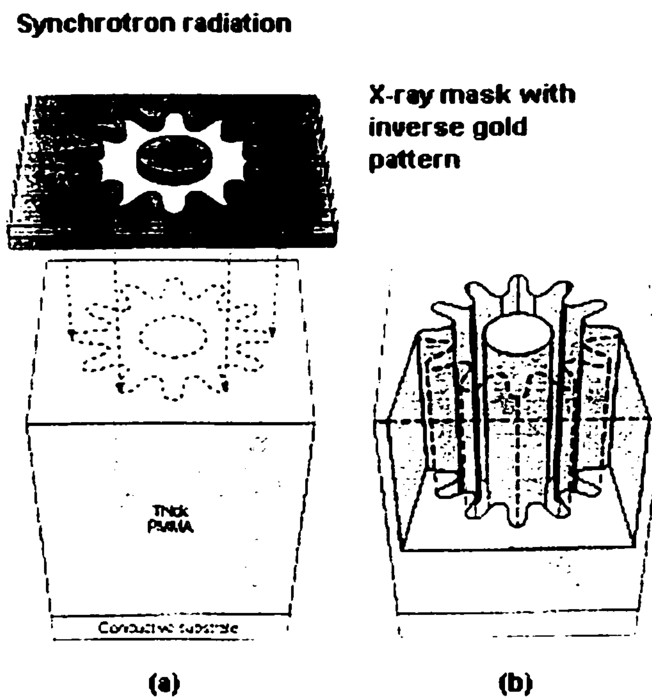

Fig. A2.1 The LIGA process (from Sze, 1994)

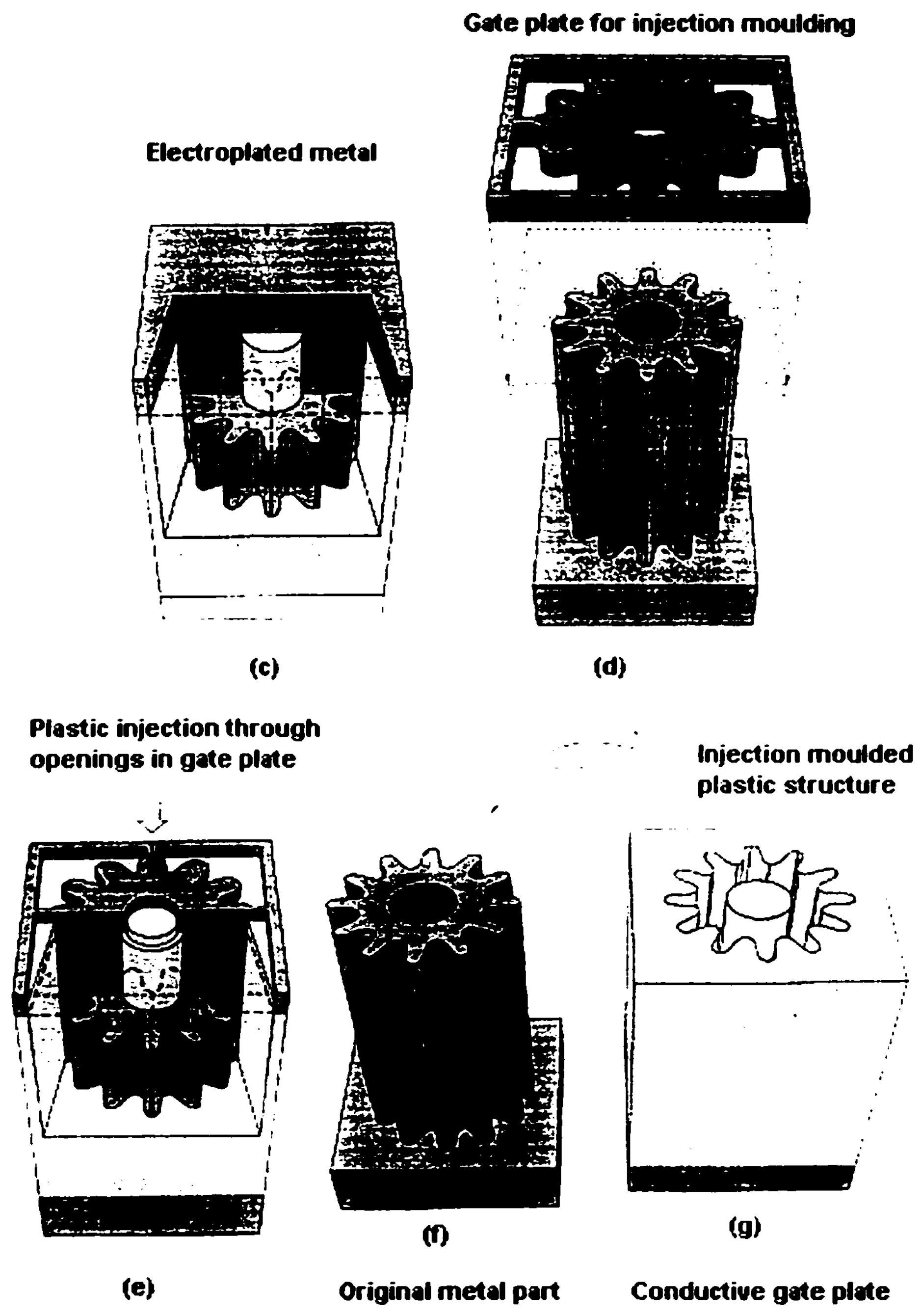

Fig. A2.1 The LIGA process (from Sze, 1994)